Electrohydrodynamics: A study of collective behavior and self-organization of an oil-in-oil emulsion

by

©Somayeh Khajehpour Tadavani

A thesis submitted to the School of Graduate Studies in partial fulfillment of the requirements for the degree of

Doctor of Philosophy

Department of Physics and Physical Oceanography
Memorial University of Newfoundland

Memorial University of Newfoundland

July 13, 2018

ST. JOHN'S NEWFOUNDLAND

Dedicated to my beloved parents

for the endless love and support

Abstract

In this thesis, I study the collective behavior and self-organization of immiscible silicone oil drops in a castor oil medium. Castor oil is a "leaky dielectric" and the silicone oil drops interact with each other due to electrohydrodynamic forces induced by an imposed electric field. The strength and the range of the hydrodynamic interactions are modulated by changing amplitude and frequency of the electric field, respectively, in a small capacitor.

The result of the electrohydrodynamic forces is to induce flows that induce drop motions, deformations and breakup. I study the effect of cell thickness, d, on the size distribution and dynamics of silicone oil drops in presence of an external DC electric field. I also investigate the effect of dimensionality by varying the cell thickness, d, and observation of drop dynamics as well as the observation of an electrohydrodynamically driven convective instability. For the first time, to our knowledge, two-roll structures, with a lateral size that is half the cell thickness, are observed experimentally. Further, this instability is also seen in castor oil medium, in the absence of any liquid-liquid and solid-liquid interfaces, indicating the importance of electrokinetic effects.

Next, I constrain the motion of silicone oil drops in 2D, using dielectrophoretic traps, in order to create a 2D droplet crystal. By driving this crystal with frequency-tunable electrohydrodynamic forces, I construct a amplitude-frequency phase diagram for the non-equilibrium order to disorder phase transition of silicone oil drops in

castor oil medium. The pure order-to-disorder behaviour is observed for a amplitude-frequency regime where no breakup events occur but the hydrodynamic flows are strong enough to deform and partially unpin the droplets from their trap potential.

Finally, an examination of the underlying flows using tracer particles reveals anomalous superdiffusive motion with power law scaling of $t^{3/2}$. The underlying probability distribution for these anomalous motions is non-Gaussian and has the form $\exp\left(-\left(\frac{x^2}{4K_\gamma t^{3/2}}\right)^{\delta/2}\right)$. At short times, it is a simple exponential decay (*i.e.* $\delta = 1$), while at longer times the distribution is consistent with $\delta = 1.4$.

This system exhibits non-equilibrium self-organization that is frequency- and amplitude-tunable, that will not only allow more detailed comparisons with detailed theory and simulation in the future. Moreover, it has been demonstrated as a model system for studying self-organization with tunable hydrodynamic interactions.

Acknowledgements

I would like first to express my sincere gratitude to my supervisor Dr. Anand Yethiraj for his continuous support, patience, and immense knowledge. Conducting a professional research and thinking strategically were two assets that I learned from him and I could not wish any better mentor for my Ph.D. He also thought me valuable life lessons that I would carry with me throughout the rest of my life.

I would like to thank Dr. Saika-Voivod for his insightful discussions in our group meeting sessions. My thanks also goes to Dr. Poduska, Dr. Morrow, and specially Dr. Merschrod who gave me access to their laboratory and research facilities.

I am also grateful to my lab mates, Edward Hayden, Payam Bagheri, Tatsuo Izawa, and Swomitra Palit for their useful comments, relevant discussions, and lots of fun we had together in the lab and off-campus.

I would like to thank my dear friends and second parents Mr. and Ms. Hicks for their love, kindness, and being there for me whenever I needed.

Last but not the least, I would like to express my appreciation to my parents, Shahnaz and Amir. Those who have been the reason of my life and without their endless support I have not been able to carry on.

Table of Contents

List of Tables

List of Figures

List of Abbreviations and Symbols

EHD	Electrohydrodynamic
PDM	Pure dielectric model
LDM	Leaky dielectric model
EKM	Electrokinetic model
F_{DEP}	Dielectrophoretic force
Re	Reynolds number
Ca	Capillary number
Ra	Rayleigh number
Re_E	Electric Reynolds number
Ca_E	Electric capillary number
Ra_E	Electric Rayleigh number
MSD	Mean square displacement
PDF	Probability distribution function
$CTRW$	Continuous time random walk
FBM	Fractional Brownian motion
RVF	Random velocity field
L_{eff}	Effective Lindemann parameter
BFM	Bright field microscopy
PIV	Particle image velocimetery
$sCMOS$	Scientific complementary metal oxide semiconductor

Chapter 1

Introduction

1.1 Non-equilibrium systems

An equilibrium state, thermal, mechanical, and/or chemical, is a condition in which no net heat, energy, and mass is transferred between the systems [1]. Although equilibrium is a favorable state in science, it is an idealization. Most systems in Nature are not in equilibrium and they exchange heat, energy or mass with their surroundings or they undergo chemical reactions [2]. Systems far from equilibrium remain poorly understood. One difficulty arises from the absence of established theoretical frameworks [3, 4]. On the other hand, unlike near equilibrium systems, far from equilibrium systems are typically nonlinear. This means that their response to a disturbance is not proportional to the magnitude of the disturbance. Moreover, far from equilibrium systems are often disordered which means they do not have a crystalline structure. Finally, such systems do not often explore all states available, a property known as non-ergodicity [4].

A system that is out of equilibrium can be designed by employing a deterministic time-dependent external force or torque. Typical examples include mechanical forces,

and forces due to applied electric or magnetic fields. One example of a far-from-equilibrium systems is the electrohydrodynamic instability, discussed in more detail in this thesis.

1.2 An overview

Bird flocks and cell colonies stretch our understanding of collective dynamics and self-organization. A common feature between them is the presence of a non-equilibrium driving force. Tunable hydrodynamic interactions, such as electrohydrodynamic interactions, play an important role in self-assemblies and collective behaviors in many far from equilibrium systems. Electrohydrodynamics (EHD) deals with fluid motion induced by electric fields [5], and it involves many problems from cloud formation [6] to crystallization [7]. Liquid drops exposed to an external electric field and surrounded by another liquid respond in a variety of ways. They can deform, rotate, coalesce, or break up [8]. The fundamental theoretical description of immiscible drop behavior in a second liquid and in an electric field is usually explained by the "leaky dielectric model" (LDM) [9]. The theory is related to accumulation of free charges at the liquid-liquid interface, which adds a tangential component to the electric stress. The tangential stress competes with the normal stress at the interface. Depending on the angular variation of stresses, or the strength of the applied electric field, the drop gives rise to shape deformation, or breakup, respectively [10].

1.3 A guide for the reader

In this thesis we use a system composed of two immiscible oils, with an externally imposed, AC or DC, electric field to study far-from-equilibrium dynamics.

In chapter 2, I first present models that describe the effect of an external electric

field on dielectric drops suspended in a leaky dielectric liquid medium. Then, I outline the relevant forces and corresponding dimensionless numbers, and the fundamentals of convection in fluids, in the presence and in the absence of an external electric field. I then introduce some useful quantities to study dynamics and structure of colloidal suspension and oil-in-oil emulsions.

In chapter 3, I first explain the experimental methods that I used to prepare my samples. Then, I give a brief description of microscopy and image processing techniques used in this work.

Chapter 4 discusses the effect of confinement on the size, breakup, and dynamics of droplets in the presence of an external DC electric field. It also presents the effect of confinement on electrokinetically driven flows in the microfluidics geometry.

The results of this thesis are presented in chapters 4 to 6. The unifying feature of these results is that they all study the collective behavior of many droplets in a driven, far from equilibrium system. While chapter 4 studies the effect of confinement, chapter 5 studies the rich dynamical structures that are obtained as a function of the driving field. While chapters 4 and 5 probe droplet shapes and motions, in chapter 6, we examine fluid flows on much shorter lengthscales and timescales.

In chapter 5, I study a non-equilibrium order-to-disorder phase transition in a microfluidic oil-in-oil emulsion, in which tunable electrohydrodynamic interactions are driven by two control parameters: frequency and amplitude of an external AC electric field. The final result is a non-equilibrium analog of a phase diagram.

A deeper understanding what is near and what is far from equilibrium requires a study of underlying fluid flows. In chapter 6, a system of oil drops, the inner fluid, is constrained on a periodic lattice and the motion of tracer particles in the outer fluid is tracked. Independent of position, frequency, and amplitude at which the experiments were carried out, superdiffusive behavior are observed. I also look for a

model system to describe the dynamics and the associated probability distributions. These distributions are non-Gaussian and the degree of non-Gaussianity gives one a measure of how far the system is from equilibrium.

Chapter 7 provides a summary of results and possibilities for future work.

Bibliography

[1] M. W. Zemansky. *Heat and thermodynamics: an intermediate textbook*. McGraw-Hill, New York, 6th edition, 1981.

[2] S. Kinoshita. *Pattern Formations and Oscillatory Phenomena*. Elsevier, Amesterdam, 1st edition, 2013.

[3] J. F. Rupprecht and J. Prost. Physical Biology. A fresh eye on nonequilibrium systems. *Science*, 352(6285):514–515, 2016.

[4] H. M. Jaeger and A. J. Liu. Far-from-equilibrium physics: An overview. *arXiv:1009.4874*, 2010.

[5] D. A. Saville. Electrohydrodynamics: The Taylor-Melcher leaky dielectric model. *Annual Review of Fluid Mechanics*, 29(1):27–64, 1997.

[6] Z. Warhaft. Laboratory studies of droplets in turbulence: towards understanding the formation of clouds. *Fluid Dynamics Research*, 41(1):20, 2009.

[7] H. Löwen. The marriage of electrostatics and hydrodynamics: simulating the dynamics of charged colloids. *Journal of Physics: Condensed Matter*, 16(10):V7–V9, 2004.

[8] P. F. Salipante and P. M. Vlahovska. Electrohydrodynamics of drops in strong uniform dc electric fields. *Physics of Fluids*, 22(11), 2010.

[9] J. R. Melcher and G. I. Taylor. Electrohydrodynamics: A review of the role of interfacial shear stresses. *Annual Review of Fluid Mechanics*, 1(1):111–146, 1969.

[10] A. Varshney, S. Ghosh, S. Bhattacharya, and A. Yethiraj. Self organization of exotic oil-in-oil phases driven by tunable electrohydrodynamics. *Scientific Reports*, 2:738, 2012.

Chapter 2

General theory and background

2.1 Electrostatics and electrohydrodynamics for a droplet in a liquid medium

2.1.1 Historical background

The first record of an electrohydrodynamic experiment is in the seventeenth century, by William Gilbert, when he observed a sessile drop of water deformed upon bringing a charged rod above it [1]. The analytic model, predicting the prolate deformation in an electric field, *i.e.*, an ellipsoid with its major axis in the direction of the electric field shown in FIG. 2.1, was derived by O'Konski and Thacher in 1953 and also Allan and Mason in 1962 for perfect dielectric drops in a perfectly insulated media [2, 3]. This model is called the "pure dielectric model" (PDM). However, some experimental observations by Allan and Mason [3] showed that some drops remain either spherical or even deform into oblate spheroids, *i.e.*, an ellipsoid with its major axis normal to the direction of the electric field shown in FIG. 2.1. Electrostatic models, which dealt with perfect dielectrics, were unable to explain the oblate deformations. As a

result, a more comprehensive model was required. The new model was built based on poorly conducting drops and media by Taylor in 1966 and a precise version of that was published by Melcher and Taylor in 1969. This model, generally referred to as the "leaky dielectric model" (LDM), has become the foundation theory of drop deformation in an external electric field [4]. The LDM is an approximation that replaces an explicit treatment of the ions with the effective boundary conditions. While, it works remarkably well on a qualitative level, there are quantitative discrepancies. A comprehensive review of the theoretical developments was given by Saville [5] and Zholkovskij *et al.* [6], providing a solution for the electrokinetic problems that were ignored in both previous models.

In the next sub-sections a brief explanation of the PDM and LDM is provided. Following that, the main differences between the LDM and the electrokinetic model are discussed. While these sections represent important theoretical background, it should be noted that only Equation (2.10) is actually used in the subsequent Results chapters.

2.1.2 The pure dielectric model (PDM)

2.1.2.1 Maxwell stress tensor components

According to the pure dielectric model (PDM) both the internal and external liquids are perfect insulators and contain no free charge carriers, therefore having zero electric conductivity [6]. An external time-varying electric field forms bound polarized electric charges at the interface of two media having different dielectric permittivities. The governing equations for electrostatics simplify to the Laplace equation (Equation (A.2) in appendix A.1.1). The boundary conditions specify continuity of the tangential component of the electric field across the drop interface (Equation (A.3) in

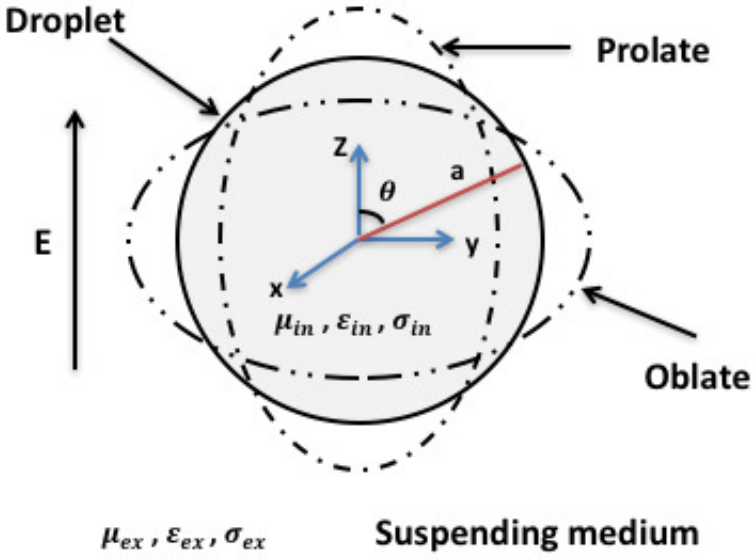

Figure 2.1: Schematic representation of the deformation of a droplet with radius a suspended in a second fluid in the presence of an electric field, E. The shaded circle represents the spherical non-deformed droplet before applying the field. The possible steady-state deformed shapes, prolate and oblate spheroids, are also depicted. The relevant properties of the droplet and suspending medium are the viscosity, μ , dielectric permittivity, ε, and conductivity, σ. The subscripts in and ex are used to represent the droplet and the suspending fluid, respectively (adapted from [7]).

appendix A.1.2), and of the normal component of the electric field (Equation (A.4) in appendix A.1.2). Also, the electric field is finite at the origin, at the center of the drop, and far from the drop, it is equal to the externally applied electric field intensity. Using these electrostatic equations leads to the electric potential and consequently the electric field both inside and outside of the drop [3]. The radial and tangential components of the electric stress, known as Maxwell stress which is the force per unit area acting on the interface, are defined by equations (A.9) and (A.10) in appendix A.1.3, respectively. By substituting the electric field components, the radial and tangential components of the non-dimensional electric stress at the interface of the drop with

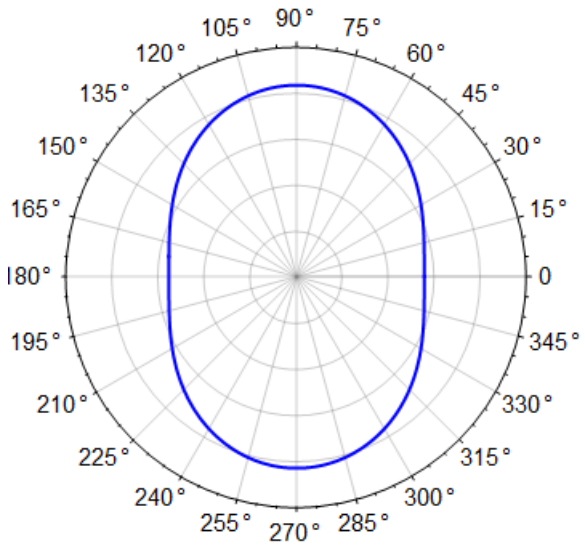

Figure 2.2: Electric stress in the pure dielectric model: The radial plot of the magnitude of the normal electric stress for $f = 0$, denoted by the blue line. A greater distance from the center indicates a larger magnitude. The electric field is along the line from 0° to 180°. The maximum of the inward force is exerted on the poles of the drop, and this gives rise to the prolate deformation.

radius a is

$$T_r \equiv \frac{T_{rr}}{\varepsilon_{ex} E^2} = \frac{9}{4} \frac{(S-1)^2}{(S+2)^2} \left(\cos^2\theta + \frac{1}{S-1} \right) (1 + \cos 2\omega t), \tag{2.1}$$

$$T_\theta = \frac{T_{r\theta}}{\varepsilon_{ex} E^2} = 0, \tag{2.2}$$

where $S = \dfrac{\varepsilon_{in}}{\varepsilon_{ex}}$, ε_{in} and ε_{ex} are the dielectric permittivities of droplet and suspending medium, respectively, E is the peak value of the alternating electric field, θ is the polar angle with respect to applied field direction, $\omega = 2\pi f$, where f is the frequency of the applied electric field, and t is the time [8]. T_r is like a dimensionless stress (or pressure), while T_θ is a dimensionless shear stress. With reference to Equation (2.1), it is noteworthy to mention that when $T_r < 0$, the radial stress is inward to the drop (like pressure, except that it is angle dependent), and in the case when $T_r > 0$ the

stress is pointed outward from the drop. The tangential component of the electric stress, Equation (2.2), is zero due to the absence of the free charges at the interface, so only the radial component gives rise to the drop deformation. In the steady state, one can assume that $f = 0$, and plot the radial component of the electric stress for a system composed of a silicone oil drop surrounded by castor oil. The radial component of the electric stress at the interface, $r = a$, is shown by a radial plot in FIG. 2.2. For dielectric constants that are relevant for a silicone oil drop, $\varepsilon_{in}/\varepsilon_0 = 2.4$, and castor oil $\varepsilon_{ex}/\varepsilon_0 = 3.6$, as the surrounding medium, $S \simeq 0.66$. Thus, $T_r = -0.07$ at the equator, *i.e.*, at $\theta = 0$, while at the poles, *i.e.*, at $\theta = \pi/2$, $T_r = -0.1$. Since negative values indicate inward stress, the resulting shape is prolate. Even when the inner and outer fluids are reversed, the positive outward force at the pole exceeds that at the equator and the deformation is still prolate. The PDM prediction, therefore, is that the deformation is always prolate, no matter which fluid is the inner or the outer.

2.1.2.2 Drop deformation function

The next step is to calculate the primary measured quantity, *i.e.* the drop deformation function, $D = \dfrac{d_\parallel - d_\perp}{d_\parallel + d_\perp}$, where $d_\parallel$ and $d_\perp$ are the axes of the ellipsoidal droplet parallel and perpendicular to the applied electric field, respectively. For a non-deformed drop with radius a, $D = 0$. For a prolate shape, $D > 0$, and for an oblate one, $D < 0$ [7].

The deformation of the drop in the electric field is characterized by a balance of interfacial tension, hydrostatic pressure, and electric stress at the drop interface. The electric stress causes the interface to distort, while interfacial tension tends to restore the original shape. Viscous stress and fluid pressure gradients due to the flow fields can also alter the deformation. In steady state, the electric stress can not create liquid flows, and the stationary deformation of the drop is due to a balance of the normal electric stress and interfacial tension forces. The drop deformation obtained

by O'konski *et al.* [2], Allan *et al.* [3], Torza *et al.* [8], and Zholkovskij *et al.* [6] is

$$D = \Phi \frac{\varepsilon_{ex} a E^2}{\gamma}, \tag{2.3}$$

where $\Phi = \frac{9}{16}\frac{(S-1)^2}{(S+2)^2}$, and is related to the Clausius-Mossotti factor. The PDM result always yields a prolate drop shape, which means that D is always positive, and the deformation is due to the polarization forces since free charge is absent and the electric stress is normal to the interface. In the static drop deformation, all fluid properties like velocity and viscosity disappear. The steady state deformation of a drop is thus observed only at low electric fields. However, when the field increases beyond a certain value, drop break up occurs [9, 10].

2.1.3 The leaky dielectric model (LDM)

2.1.3.1 Maxwell stress tensor components

The leaky dielectric model (LDM) differs from the PDM through the assumption of uniform non-zero conductivities of each liquid. Low-conductivity liquids, such as hydrocarbons, do not self-ionize. The charge carriers, which are ions, result from the spontaneous dissociation of tiny amounts of ionizable substances present in the liquids [11]. In LDM, the conductivities are small enough that they only modify the fluid-fluid interface. The LDM presumes the existence of free charge carriers in both liquids [4, 6, 8, 12]. Upon applying the electric field, there is now the possibility for free charge carriers at the interface. Thus, the drop deformation comes from three contributions. The first part, similar to PDM, is the electric force due to the bound polarization charge perpendicular to the interface by reason of the difference in dielectric permittivities of the liquids. The second part consists of normal and tangential electric forces due to the field-induced free charges at the interface, which

cause fluid motion. Once there is fluid motion, and given the very low Reynolds number, these additional forces are balanced at all times by the viscous force, acting normal and transverse to the interface [6].

The electrostatic equations are summarized by the Laplace equation (Equation (A.2) in appendix A.1.1) for droplet and suspending medium. The boundary condition is once again specified first by continuity of the tangential electric stress at the drop interface (Equation (A.3) in appendix A.1.2). Under a static field, the LDM uses the continuity of current at the interface as the second boundary condition,

$$\mathbf{J_{1n}} = \mathbf{J_{2n}}, \tag{2.4}$$

where $\mathbf{J_{1n}} = \sigma_1 \mathbf{E_{1n}}$ and $\mathbf{J_{2n}} = \sigma_2 \mathbf{E_{2n}}$ are the normal components of the current density at the interface. In the case of a non-steady state, Equation (2.4) is written as

$$\mathbf{n} \cdot (\sigma_{in} \mathbf{E}_{in} - \sigma_{ex} \mathbf{E}_{ex}) = \frac{-\partial \sigma_f}{\partial t} \tag{2.5}$$

where σ_f is the total free surface charge density.

Solving the electrostatic equations gives rise to the electric potential and electric field inside and outside of the drop from which one can calculate the radial and tangential components of the electric stress (using Equations (A.9) and (A.10) in appendix A.1.3). In the presence of an oscillatory electric field with a constant field amplitude, E, the electric stress is a function of the frequency, f, and the angle between the radial vector of the drop and the field direction, θ. The total stress is a sum of normal and transverse stresses which include both dipolar and hydrodynamic contributions. Each contribution has time independent and time dependent parts. As with the discussion with the PDM, the steady drop deformation arises from the time independent part, while the time dependent part gives rise to shape oscillations [13].

At steady state, the dimensionless radial component of the electric stress is given as

$$T_r \equiv \frac{T_{rr}}{\varepsilon_{ex}E^2} = \frac{9}{4}\frac{\left[\left(H^{-2}-2SH^{-2}+1\right)+\tau^2\omega^2\left(S-1\right)^2\right]\cos^2\theta+\left(S-1\right)\left(H^{-2}+\tau^2\omega^2\right)}{\left(2H^{-1}+1\right)^2+\tau^2\omega^2\left(S+2\right)^2}. \tag{2.6}$$

The dimensionless tangential component is given by

$$T_\theta \equiv \frac{T_{r\theta}}{\varepsilon_{ex}E^2} = \frac{9}{2}\,\frac{H^{-1}\left(H^{-1}S-1\right)}{\left(2H^{-1}+1\right)^2+\tau^2\omega^2\left(S+2\right)^2}\,\cos\theta\,\sin\theta. \tag{2.7}$$

In the above, $H = \dfrac{\sigma_{in}}{\sigma_{ex}}$ and $\tau = \dfrac{\varepsilon_{ex}}{\sigma_{in}}$ [8]. Consider the case where σ_{in} is small and $\sigma_{ex} \to 0$, as a result $H^{-1} \to 0$, but also $\tau \to \infty$. The steady component of Equation (2.6), $T_{r,\omega\to 0}$, becomes

$$T_r \equiv \frac{T_{rr}}{\varepsilon_{ex}\overline{E}^2} = \frac{9}{2}\,\frac{(S-1)^2}{(S+2)^2}\left(\cos^2\theta+\frac{1}{S-1}\right), \tag{2.8}$$

where $\overline{E} = \dfrac{E}{\sqrt{2}}$. Equation (2.8) in this limit reduces to Equation (2.1) for small ω. Similarity, Equation (2.7) also reduces to Equation (2.2) at long times (large τ) .

The angular variation of the radial and tangential stresses on the drop and the variation of the total stress versus applied frequency are plotted in FIG. 2.3. FIG. 2.3(a) shows the radial component of the electric stress for dielectric constants and conductivities that are relevant for a silicone oil drop ($\varepsilon_{in}/\varepsilon_0 = 2.4$ and $\sigma_{in} = 3.95\times10^{-11}$ S/m), with castor oil ($\varepsilon_{ex}/\varepsilon_0 = 3.6$ and $\sigma_{ex} = 4.0\times10^{-10}$ S/m), as the surrounding medium: this results in the parameters $S \simeq 0.67$ and $H \simeq 0.1$. Three frequencies are stated as examples in the following.

At $f = 2$ Hz, $T_r \simeq -0.17$ at the equator and -0.13 at the poles which means the inward force is bigger at the equator and the resulting drop shape is oblate. At $f = 10$ Hz, $T_r \simeq -0.08$ at the equator and -0.11 at the poles which means the inward

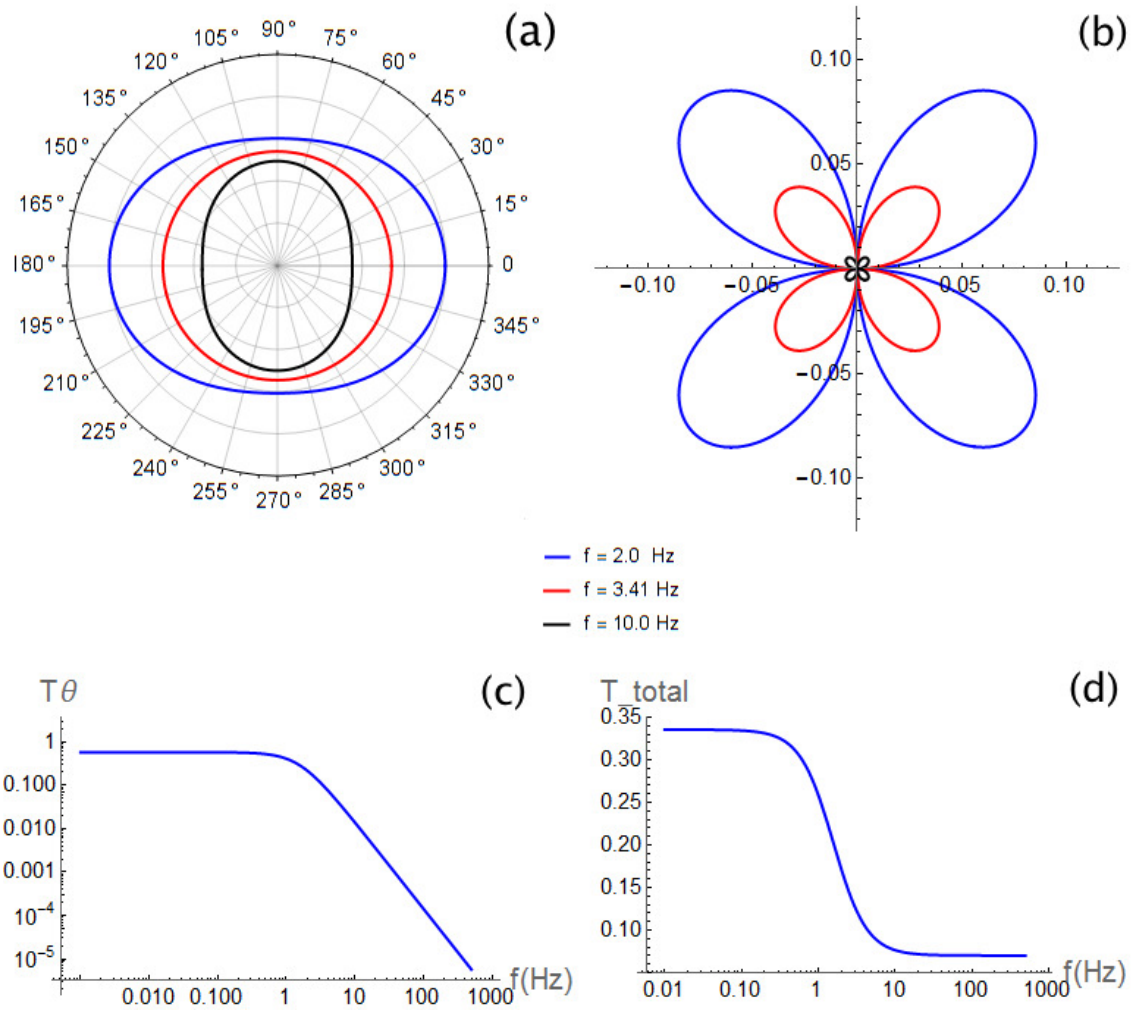

Figure 2.3: Electric stress in the leaky dielectric model. (a): The radial plot of the normal component of the electric stress at the interface. The electric field is along the line from 0° to 180°. (b): The radial plot of the tangential component of the electric stress at the interface. (c): The amplitude of the tangential component of the electric stress versus frequency. (d): The variation of total stress on the drop with the applied frequency.

force is bigger at poles and resulting drop is a prolate spheroid. At $f = 3.41$ Hz, $T_r \simeq -0.12$ at both the poles and the equator and the drop remains spherical.

Fig. 2.3(b) shows the polar plot of the tangential component of the stress which is maximum at $\frac{\pi}{4}$, $\frac{3\pi}{4}$, $\frac{-3\pi}{4}$, and $\frac{-\pi}{4}$. The tangential component of the electric stress causes circulation patterns inside and outside the drop. The direction of the tangential electric stress at the interface determines the direction of the flow inside and outside the drop. The magnitude of the tangential stress decreases with increasing frequency, FIG. 2.3(c). The sharp decrease for frequencies $f > \frac{1}{2\pi\tau}$ comes from the $\tau^2\omega^2$ dependence, in the denominator of Equation (2.7). This sharp decrease is the cause of a frequency-dependent transition from pure dipolar behavior at high frequencies to increasingly strong electrohydrodynamic behavior as frequency is lowered. With increasing frequency, the magnitude of the total stress, FIG. 2.3(d), decreases too [8, 13].

2.1.3.2 Drop deformation function

The drop deformation function in LDM, can be obtained from a similar procedure as in the PDM, and the only difference is that the hydrodynamic equations contain an additional tangential stress which arises from interface charges (Equation (B.5) from appendix B.1 is replaced by Equation (B.7) from appendix B.2). The drop deformation function is given by

$$D = \Phi \frac{\varepsilon_{ex} a E^2}{\gamma}, \tag{2.9}$$

where [8]

$$\Phi = \frac{9}{16}\left(1 - \frac{H^{-1}(11M+14) + H^{-2}(15(M+1) + S(19M+16)) + 15\tau^2\omega^2(1+M)(1+2S)}{5(1+M)\left((2H^{-1}+1)^2 + \tau^2\omega^2(S+2)^2\right)}\right), \tag{2.10}$$

where $S = \frac{\varepsilon_{in}}{\varepsilon_{ex}}$, $H = \frac{\sigma_{in}}{\sigma_{ex}}$, and $M = \frac{\mu_{in}}{\mu_{ex}}$. The prolate and oblate deformations are indicated where $\Phi > 0$ and $\Phi < 0$, respectively.

In the LDM, when the droplet approaches a steady state under the influence of the external electric field, the four steady circulations along the interface would be generated inside the droplet due to the shear stress at the interface generated by accumulated charge which in turn is produced by applying the electric field. According to the LDM, the maximum value of the tangential velocity is obtained at the droplet interface at the angle of $\frac{\pi}{4}$, $\frac{3\pi}{4}$, $\frac{-3\pi}{4}$, and $\frac{-\pi}{4}$, *i.e.* $45°, 135°, 225°$, and $315°$ correspond to maxima of the tangential component of the electric stress, FIG. 2.3(b).

Consider a simplified cartoon of a drop in an electric field, shown in FIG. 2.4. Upon applying the field, a charge distribution is created inside and outside of the droplet, at the interface, depending on the polarity of the nearest electrode. When $SH^{-1} < 1$ the charge relaxation time of the drop, $\tau_{in} = \frac{\varepsilon_{in}}{\sigma_{in}}$, is smaller than the charge relaxation time of suspending medium, $\tau_{ex} = \frac{\varepsilon_{ex}}{\sigma_{ex}}$ *i.e.*; $\sigma_{in} > \sigma_{ex} \Rightarrow \tau_{in} < \tau_{ex}$, and therefore the conduction in the drop is faster than the suspending liquid. As a result, the interface charge distribution is dominated by the charge separating inside the drop, and the drop dipole moment is aligned with the electric field. In this case, charges at the poles are attracted toward the electrodes, resulting in a prolate shape. This is depicted in FIG. 2.4(a). In the opposite case, $SH^{-1} > 1$, *i.e.*, $\sigma_{in} < \sigma_{ex} \Rightarrow \tau_{in} > \tau_{ex}$, and the charge response of the suspending fluid is faster than the drop. Hence, the charge of the interface is dominated by the charge separation in suspending fluid and the drop dipole is inverted, as shown in FIG. 2.4(b) [7, 14]. The flows provide stresses, in order to balance the action of tangential components of the field acting on charges at the interface [5]. While the above cartoon is constructed with time-independent field in mind the results hold for time-dependent (dc) fields as well; because the more conductive medium dominates in terms of ion concentrations.

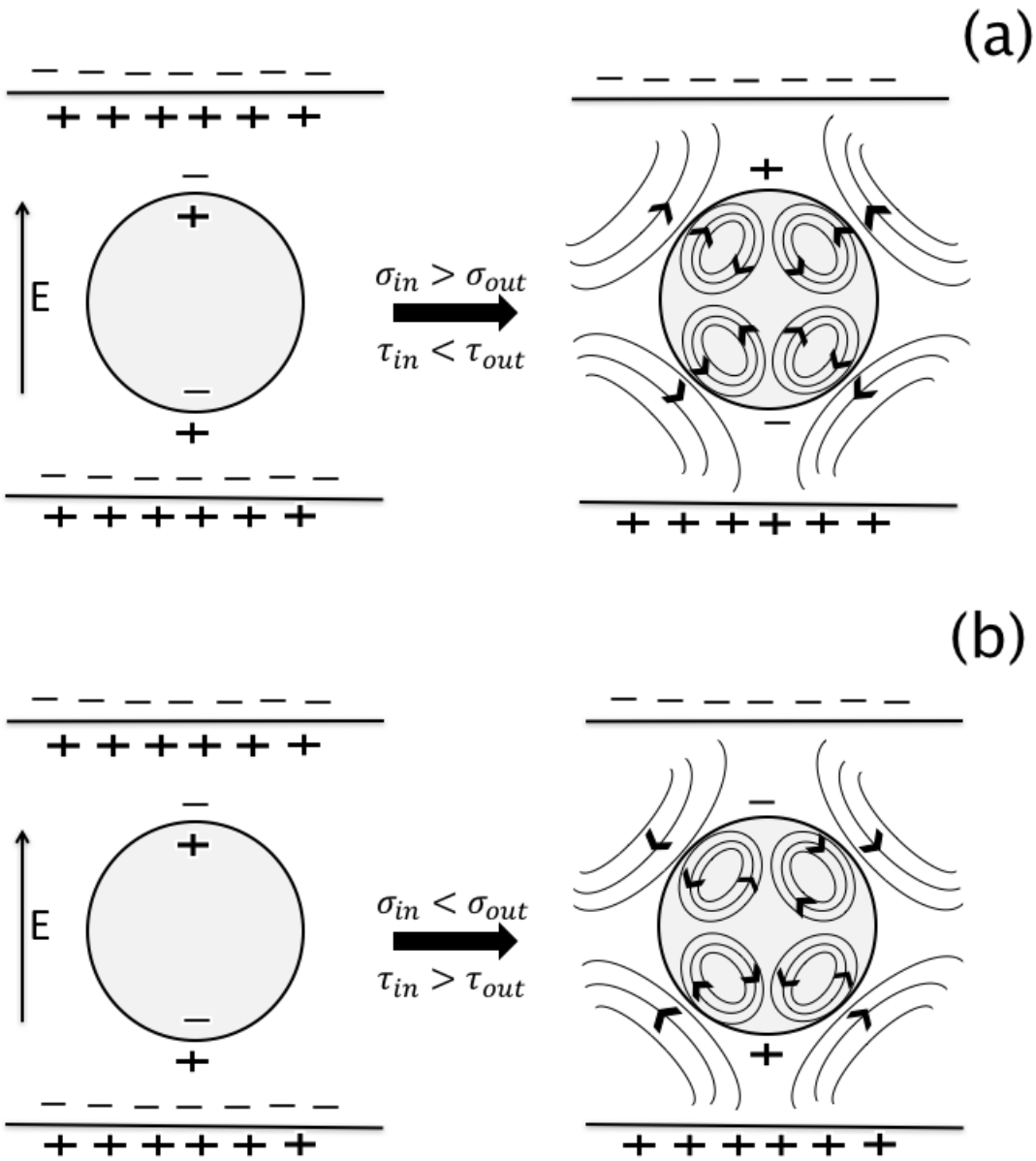

Figure 2.4: A schematic design of charge distribution at the interface, inside and outside of the droplet: (a): Prolate deformation. (b): Oblate deformation. Left and right figures show the initial and final charge distributions, respectively. The final charge distribution is defined by the competition between charge relaxation times of inner and outer fluids. The faster conduction is dominant and defines the final charge distribution sign. The direction of the flow is such that try to push the charges at the interface to the electrodes with opposite signs. The corresponding direction of the tangential electric stress is denoted by arrows.

It should be noted that the LDM does not provide a complete description of the problem, and works when the conductivity is small enough such that one can focus exclusively on the interface.

2.1.4 Experimental discrepancies

In the Taylor regime of weak fields, fields that are not strong enough to break up, move, or rotate droplets, the qualitative aspects of the LDM are satisfactory and one is able to predict correctly the oblate and prolate deformations. There nevertheless exist quantitative discrepancies in this regime. In most of the experiments, the deformation of the drop, for both oblate and prolate deformations, was larger than the theoretical values by a factor of 2 [5, 15]. The electrokinetic models, EKM, were invoked in order to address the quantitative inconsistencies in weak fields and it is discussed in the next section.

At higher electric fields, a new dynamical regime has been uncovered in experiments: a drop tilts and then shows Quincke electro-rotation upon increasing the field amplitude [16, 17], and in some cases gives rise to droplet breakup [18]. Drop electro-rotation is well known since the work of Quincke [19] on rigid particles in strong electric field. For a solid particle, in a viscous fluid and in a presence of a uniform electric field, the symmetry is broken by a small rotation of the particle and asymmetrical distribution of charge, resulting in a net torque on the solid particle. Quincke rotation for liquid drops has not yet been fully understood. Recently, a numerical simulation was carried out by Das *et al.* [20] to address electro-rotation and breakup of a viscous drop. In contrast with the Taylor description, which considers a balance between charge relaxation and charge convection by the interfacial fluid flow, the interfacial nonlinear charge convection is taken into account. In moderate electric fields, this simulation study predicts Quincke rotation of droplets, but not for

very strong electric fields and low-viscosity drops. With increasing field amplitude, a transition to electro-rotation, after strong deformation in the Taylor regime, leads the drop towards a more spherical shape. Decrease in D with the onset of Quincke rotation changes the nature of flow around the droplet. Under Quincke rotation the flow becomes rotational [18, 20], and consequently it changes the charge distribution and results in a reduction in the effective dipole moment and the magnitude of the electric stress.

At very strong electric fields, a chaotic breakup of droplets was also observed and reported by Varshney *et al.* [21, 22] and Khajehpour Tadavani *et al.* [23]; the latter is part of this thesis, Chapter 4. This regime is poorly understood and to our knowledge, it has not yet been studied theoretically.

2.1.5 The electrokinetic model (EKM)

The LDM is a "lumped-parameter" model. The LDM replaces the role of ions in the diffuse double layer, and the existence of any bulk charge carriers, with a tangential electric field boundary condition. It is remarkable that it works so well qualitatively. The charged interface attracts counter-ions in the bulk of fluid and repels co-ions over a lengthscale comparable to the Debye length. Thus, one can apply the electrokinetic effect, *i.e.* the presence of a diffuse layer of charge carriers in both liquids, as a correction to the LDM [5, 12].

The need to develop an electrokinetic model, the EKM, for the drop deformation was noted by Torza *et al.* in 1971. In general, in EKM, the electric field distribution was described by the Poisson equation (Equation (A.1) in appendix A.1.1). The current density includes the contribution of the convection of the charge carriers, the

diffusion, and the electromigration into ionic transfer as

$$\mathbf{J} = \rho_f \mathbf{V} - D\nabla\rho_f - \sigma\nabla\psi, \tag{2.11}$$

where ρ_f, V, D, σ, and ψ are volume charge, velocity, diffusion coefficient, conductivity, and electric potential, respectively. For simplicity, all charge carriers in each liquid have equal diffusion coefficients, and the thickness of the diffuse charge layer is evaluated using the Debye length. Moreover, EKM uses the generalized statement of the continuity of current in each liquid as

$$\nabla \cdot \left[\frac{\partial (\varepsilon \mathbf{E})}{\partial t} + \mathbf{J} \right] = 0 \tag{2.12}$$

In the steady state, the displacement current vanishes from Equation (2.12), yielding $\nabla \cdot \mathbf{J} = 0$. The hydrodynamic governing equations, modified by including the electrical body forces or $\rho\mathbf{E}$, for each liquid are given in Equation (B.3) in appendix B. Also, all LDM's hydrodynamic boundary conditions are valid in EKM [5–7, 24].

Zholkovskij *et al.* [6] obtained an analytical expression for a small drop deformation in a "weak" external electric field. In their work, the diffuse layer is electrically neutral; and any ionic transfer by convection is ignored. The expression derived represents the drop deformation as a function of the parameters employed in previous theories, S, H, and M, as well as two additional parameters. The additional parameters are the ratios of the drop radius to the Debye lengths of the drop and outer liquid, respectively. The expression obtained for the drop deformation is valid for arbitrary values of all parameters. This solution is also able to predict the behavior of the leaky dielectric drop in a pure dielectric medium and a pure dielectric drop in a leaky dielectric medium; none of these cases have ever been studied theoretically before. The drop deformation functions predicted by this theory are in good agreement with the

LDM and PDM for liquids with high and low conductivity, respectively. The surprise is that the theory is in quantitative agreement with LDM, including its discrepancies with respect to experiment, such as theoretical deformation being smaller than deformation observed in experiments. This theory is not applicable for high strengths of the electric field or also for large drop deformation. Thus, there is room for quantitative studies, with careful quantitative experiments to enable detailed comparisons with future simulations, in this field.

Schnitzer *et al.* [25] have proposed a new EKM approach, motivated by the work of Baygents *et al.* [24], for drop deformation and electrophoretic drop motion, for strong amplitude of the electric field. Unlike the EKM of Zholkovskij *et al.* [6] and the LDM of Melcher *et al.* [4], both of which assume zero net charge on the interface, total charge held by interface in the absence of the external field, Schnitzer *et al.* argued that the screened net charge is not zero. The action of the external field on a slightly perturbed equilibrium net charge distribution, at the interface, results in slow electro-osmotic flow profiles. These flows, however, are smaller than those corresponding to the LDM circulations. The net charge at the interface, however, is surrounded by two narrow space charge layers, and the electro-neutral bulk domains. These neutral domains are homogenized by strong ionic advection. Following the work of Baygents *et al.*, Schnitzer *et al.* use two quantities $\beta = \dfrac{E_\infty a}{k_B T/e}$ and $\delta = \dfrac{\kappa^{-1}}{a}$. β is ratio of drop voltage to the thermal voltage, $k_B T/e \approx 26$ mV at room temperature, and δ is the ratio of Debye thickness of the outer fluid to the drop size, respectively. The focus of interest was the limit of $1 \ll \beta \ll \delta^{-1}$. This indicates that the inner and outer fluids have thin diffuse-charge layers in a presence of a strong electric field. In the Baygents *et al.* approach, the inner and outer regions can not be matched to provide the flow field directly, calculated by LDM, and an intermediate region with thickness of β^{-1} is required [26]. Schnitzer *et al.* followed the Baygents *et al.* approach and succeeded

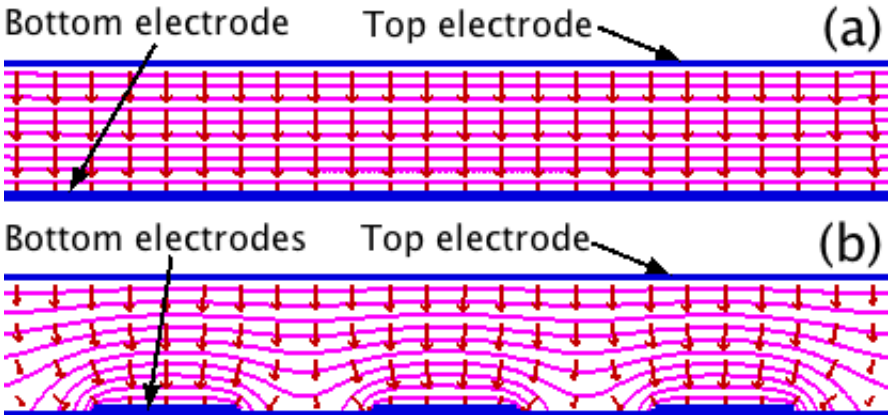

Figure 2.5: (a)-(b): Simulations of electric fields and equipotential lines, simulated by Poisson Superfish in a cell with a simple, (a), and patterned, (b), bottom conducting electrodes. The top plates in both (a) and (b) are simple electrodes. (a): Equipotential lines are parallel and electric field vectors, denoted by arrows, are perpendicular to them. The electric field vectors are uniformly spaced and are equally dense everywhere. (b): Due to the non-uniformity of the bottom electrode, the low electric field, non-electrode regions, have less dense equipotential lines and smaller electric fields vectors.

to match the inner and outer regions, without any intermediate region, and to reduce their EKM to LDM. In doing so, they noticed that the ionic diffusivity ratios are not independent parameters and are all proportional to the ratio of viscosities.

2.2 Dielectrophoresis

The dielectrophoretic force, F_{DEP}, is a force which is exerted on a dielectric liquid, surrounded by another dielectric medium, in the presence of a non-uniform electric field. Both immiscible dielectric liquids experience a gradient of the electric field due to the non-uniformity induced by a patterned electrode. FIG. 2.5 shows simulations of equipotential and electric field lines simulated in the software Poisson Superfish [27]. The gradient of electric field results in a movement of the interface due to induced

polarization in the dielectric fluids. F_{DEP} can be expressed as

$$F_{DEP} = \frac{1}{2}\left(\varepsilon_1 - \varepsilon_2\right) \nabla\left(\mathbf{E}\cdot\mathbf{E}\right) - \frac{1}{2}\mathbf{E}\cdot\mathbf{E}\nabla\left(\varepsilon_1 - \varepsilon_2\right), \tag{2.13}$$

where ε_1 and ε_2 are the permittivities of liquid 1 and 2, respectively, and $\mathbf{E}$ is the electric field across two electrodes. The second term is usually either negligible or zero. The electric field gradient and the difference between the dielectric constants play key roles to F_{DEP}. Generally, F_{DEP} changes sign depending on whether $\varepsilon_1 > \varepsilon_2$ or $\varepsilon_1 < \varepsilon_2$. When F_{DEP} is strong enough, it forces the liquid with smaller dielectric constant to redistribute into low electric field regions, non-electrode regions, and the liquid with higher dielectric constant to squeeze into higher field regions. The redistribution of two liquids is often used in optical imaging and in the microlens industry [28].

2.3 Forces and dimensionless numbers

2.3.1 Forces

Forces in an incompressible flowing fluid include inertial force, viscous force, pressure force, gravity force, surface tension force, and electric force. These forces per unit

volume, υ, or force densities, can be written as follows

$$\text{inertial forces} \qquad \rho\frac{dV}{dt} \propto \frac{\rho V^2}{L}, \tag{2.14a}$$

$$\text{viscous forces} \qquad \frac{\mu}{y}\frac{du}{dy} \propto \frac{\mu V}{L^2}, \tag{2.14b}$$

$$\text{pressure forces} \qquad \frac{\Delta p}{y} \propto \frac{\Delta p}{L}, \tag{2.14c}$$

$$\text{gravity forces} \qquad \frac{mg}{\upsilon} \propto g\rho, \tag{2.14d}$$

$$\text{surface or interfacial tension forces} \qquad \frac{\gamma}{L^2}, \tag{2.14e}$$

$$\text{electric force} \qquad \frac{\varepsilon E^2}{L}, \tag{2.14f}$$

where ρ, V, L, μ, Δp, g, γ, ε, and E are density of liquid, characteristic velocity of an object relative to the fluid, characteristic length, viscosity, pressure difference, gravitational acceleration, surface or interfacial tension, dielectric permittivity, and electric field respectively. The ratio of any two forces will be a dimensionless number. In the following, the most relevant numbers to the current work will be introduced.

2.3.2 Reynolds number: (Re)

The Reynolds number, Re, is a criterion that measures whether fluid flow is absolutely steady (laminar), or turbulent. The Reynolds number is defined as the ratio of inertial forces, the nonlinear term on the left hand side of Equation (A.19), to viscous forces, the third term on the right hand side of the same equation, so

$$Re \equiv \frac{\text{inertial forces}}{\text{viscous forces}} = \frac{\rho V^2/L}{\mu V/L^2} = \frac{L^2/\nu}{L/V} = \frac{\text{viscous time scale}}{\text{convective time scale}}. \tag{2.15}$$

In the above $\nu = \dfrac{\mu}{\rho}$ is the kinematic viscosity. At high Reynolds numbers, e.g $R_e > 2000$ for pipe flows [29], flows tend to be turbulent. Also, Reynolds number can

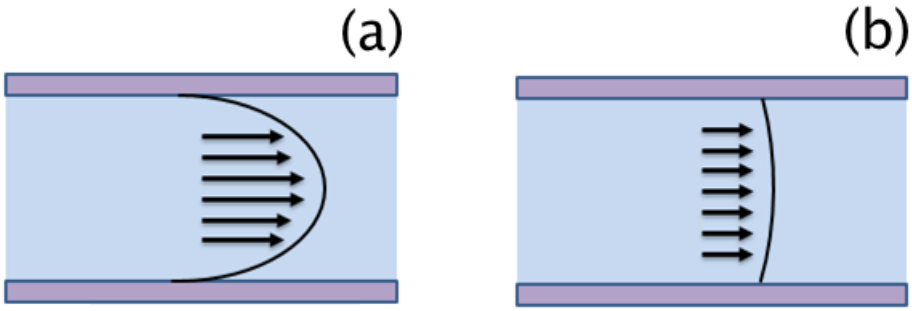

Figure 2.6: Mean velocity profiles for laminar, (a), and turbulent, (b), pipe flow. (a): The velocity profile across the diameter of the pipe for laminar flow conditions shows a gradual velocity gradient. (b): Very steep gradients near the walls resulting from turbulent flow conditions. Those steep gradients are proportional to the flow resistance in the pipe. Thus, turbulence results in significantly less flow for a given applied pressure.

be a measure of the viscous and convective time scales. A large Reynolds number means that viscous effects propagate slowly into the fluid. This is the reason why boundary layers are thin in high Reynolds number flows, because the fluid is being convected along the flow direction at a much faster rate than the spreading of the boundary layer, which is normal to the flow direction FIG. 2.6. In the microfluidic systems considered in this thesis, $Re = 10^{-7} - 10^{-5}$.

2.3.3 Capillary number: (Ca)

The capillary number, Ca, represents the relative effect of viscous forces related to surface or interfacial tension acting across an interface. It is written as

$$Ca \equiv \frac{\text{viscous forces}}{\text{surface tension force}} = \frac{\mu V/L^2}{\gamma/L^2} = \frac{\mu V}{\gamma}. \tag{2.16}$$

If $Ca \gg 1$ the viscous forces dominate over surface or interfacial tension forces. However, if $Ca \ll 1$, then viscous forces are negligible compared to the surface or interfacial forces [30]. The capillary number can be varied by changing the flow rate,

the interfacial tension, and viscosity of the fluids.

2.3.4 Rayleigh number: (Ra)

Heat convection is generated by buoyant forces. A thermal gradient between the interface and the bulk of the fluid creates density differences within the fluid. Natural heat convection does not depend on the fluid velocity and but rather depends on fluid properties including density, ρ, viscosity, μ, thermal diffusivity, α, characteristic length, L, and buoyant force per unit volume, $\rho g \beta \Delta T$, where ρ, g, β, and ΔT are density, acceleration of the gravity, fluid's coefficient of thermal expansion with unit of 1/K, and the characteristic temperature difference of the flow, respectively [31].

The Rayleigh number, Ra, is associated with the heat transfer within the fluid and it represents the ratio of the destabilizing effect of buoyancy to the stabilizing effect of viscosity acting on the fluid and it is shown by

$$Ra \equiv \frac{\text{buoyant forces}}{\text{viscous forces}} = \frac{\rho g \beta \Delta T}{\mu \alpha / L^3}. \tag{2.17}$$

When the Rayleigh number is below a critical value, the heat transfer is in the form of conduction and when it exceeds the critical value, it is in the form of convection [30]. In the simplest case, when the fluid is in between two free boundaries, a problem that was solved by Lord Rayleigh in 1916, the critical value of Rayleigh number is $Ra \simeq \frac{27\pi^4}{4}$ [32].

2.3.5 Electric Reynolds number: (Re_E)

Based on LDM, there is no real perfect dielectric so the charge conduction process cannot be completely ignored. In low inertia systems dominated by viscosity or surface tension or both, the charges introduced into the dielectric liquid have sufficient time

to fully relax to a surface charge from a bulk volumetric charge. The typical time for volumetric charge to decay is called the space charge relaxation time and it is the ratio of the dielectric permittivity to the surface charge density of the medium, $\frac{\varepsilon}{\sigma}$. However, in the presence of inertia forces, the advection time scale is sometimes shorter than the space charge relaxation time scale. Then, the characteristic time for a fluid element to move a distance is set by the advection time scale [33].

The relative importance of these two time scales is shown by the electric Reynolds number, Re_E, and it is defined as the ratio of the time scale of the charge relaxation by ohmic conduction to the time scale of charge convection by the flow. This is shown by [34]

$$Re_E \equiv \frac{\text{ohmic charge relaxation time scale}}{\text{charge convection time scale}} = \frac{\varepsilon/\sigma}{L/V}. \tag{2.18}$$

2.3.6 Electric capillary number: (Ca_E)

In the presence of electrostatic forcing, one can define electric capillary number, Ca_E, as the dimensionless ratio between electric forces and the restoring interfacial tension acting on a drop [35],

$$Ca_E \equiv \frac{\text{electric forces}}{\text{interfacial tension forces}} = \frac{\varepsilon_{ex} E^2/a}{\gamma/a^2} = \frac{\varepsilon_{ex} a E^2}{\gamma}, \tag{2.19}$$

where a is the radius of the non-deformed drop. The relation between Ca_E and the droplet shape deformation, D, is shown by

$$D = \Phi \, Ca_E, \tag{2.20}$$

where Φ is the discriminating function introduced in Equation (2.9). Although, at low electric fields the relation between capillary number and the drop deformation is

provided by (2.20), this is not the case when Ca_E is above a critical value [8]. In other words, steady equilibrium deformation of a drop no longer exists if the electric field strength exceeds the critical value. Consequently, the interfacial tension is overcome by electric forces and the resulting dynamics is either a tip-streaming deformation when $\varepsilon_{in}/\varepsilon_{ex} > 1$ [9, 36–39] or a pinch-off deformation which produces a bulbous-ended deformation and breakup when $\varepsilon_{in}/\varepsilon_{ex} < 1$ [9, 36, 37, 39].

In 1998, Feng [34] represented the electric capillary number using $Ca_E = \mu_{ex}U/\gamma$, where U is the maximum velocity at the drop surface calculated from the creeping-flow solution for a spherical drop at $Re_E = 0$. Therefore, the electric capillary number is expressed by

$$Ca_E \equiv \frac{9 \mid S^{-1}H - 1 \mid M^{-1}}{10\left(H+2\right)^2\left(M^{-1}+1\right)} \frac{\varepsilon_{in} a E^2}{\gamma}. \tag{2.21}$$

In this system $S = \varepsilon_{in}/\varepsilon_{ex} = 0.67$, $H = \sigma_{in}/\sigma_{ex} = 0.10$, $M = \mu_{in}/\mu_{ex} = 0.17$, $\gamma \simeq 3{-}4$ mN/m is the interfacial tension between the oils, $\varepsilon_{in} = \varepsilon_0 k_{in} = 21.24{\times}10^{-12}$ F/m, a is radius of the drop and E is the strength of the applied electric field. The electric capillary number can be written as $Ca_E = 0.9{\times}10^{-9} a E^2$ (where a and E are expressed in mks units).

2.3.7 Electric Rayleigh number: (Ra_E)

Electrohydrodynamic instability flows are triggered by a nondimensional parameter called the electric Rayleigh number, Ra_E. These flows are due to the transport mechanism of charge distribution. Electric charges move, relative to the liquid, with a drift velocity, $V_d = \mu_d E$, where E is the electric field and μ_d is the ionic mobility [40]. The electric Rayleigh number measures the relative importance of Coulomb forces to

viscous forces and is given by

$$Ra_E \equiv \frac{\text{electric forces}}{\text{viscous forces}} = \frac{\varepsilon_{ex} E_0^2 / L}{\mu V / L^2} = \frac{\varepsilon_{ex} E_0^2 d^2}{\mu K_{eff}} \frac{\nabla \sigma}{\sigma_0}, \tag{2.22}$$

where d is the thickness, $\varepsilon_{ex} = \varepsilon k_{ex}$ is the dielectric permittivity, μ is the viscosity of the layer, E_0 is the applied field strength at the lower conductivity boundary, K_{eff} is an effective diffusivity associated with the Brownian motion of the charge-carrying solutes, and $\frac{\nabla \sigma}{\sigma_0}$ is the relative conductivity increment [41].

2.4 Convection in fluids

2.4.1 A note on convection

Convection is the macroscopic collective flow of liquid particles which can be caused by different driving forces. These driving forces are buoyancy, surface tension, bulk electric forces that arise from density gradients, thermal or concentration gradients, and the violation of electroneutrality principle, respectively. Convection of all sorts, independent of the nature of driving forces, may result in *self-organized* spatial or spatio-temporal patterns as cooperating rolls, fingerprint-like shapes or hexagonal cells [42]. Chapter 4 uncovers a particular convective instability in our system of interest.

2.4.2 Rayleigh-Bénard and Bénard-Marangoni convections

In 1900 Henri Bénard made experiments on the instability of a thin layer of fluid, less than 1 mm thick, open to air and subjected to a vertical temperature gradient. The flow is driven by differences in density due to a temperature gradient. The warmer fluid near the hot plate has a lower density than the rest of the fluid. The colder and

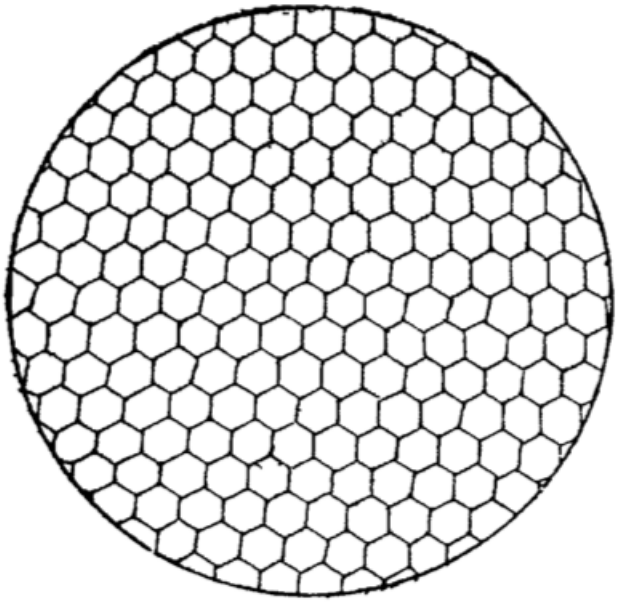

Figure 2.7: Top view of convection patterns in a thin layer of spermaceti heated from below (adapted from [43]).

heavier fluid at the top sinks due to gravity and resulting buoyant forces, while it is opposed by the viscous damping force in the fluid. The balance between these two forces determines if convection will occur and is expressed by the Rayleigh number, Equation (2.17). Bénard cells are mainly hexagonal and the pattern resembles a honeycomb. FIG. 2.7 shows a top view of convection patterns in a thin layer of spermaceti. Bénard accurately determined properties such as the spatial periodicity of the hexagonal pattern, its variation, and the profile of the interface [43]. Later, in 1916, the experiments made by Bénard inspired Lord Rayleigh to study the theoretical aspects of the convective rolls. He developed a complete linear stability analysis, for a liquid between two horizontal solid boundaries and heated from below, assuming that the vertical velocity component and the temperature disturbance vanish at the top and bottom boundaries [32]. As a result, this convective phenomenon is called the Rayleigh-Bénard instability. The discrepancies between Bénard experiments and

Rayleigh theoretical results led to a new theory based on the gradient of the surface tension, known as the Marangoni effect. In 1958, the role of the Marangoni effect was pointed out by Pearson for the case of a free liquid surface [44], where the instability mechanism arises from temperature fluctuations on the free surface, which in turn give rise to gradients in the surface tension. The surface tension gradient forces the warmer fluid to a cooler spot, which is a region with the higher surface tension, and as a result, the bulk of the layer will be deformed. The bulk flows pump the fluid up, reinforcing the initial temperature fluctuations and correspondingly, flows which are driven by the surface tension gradient develop. This convection is called Bénard-Marangoni or thermo-capillary convection.

2.4.3 Electrohydrodynamic convection

Electrohydrodynamic, EHD, systems are hydrodynamical systems exposed to an electric field. Liquids in these systems are good insulators or weak electrolytes, with conductivities less than 1 S/m; therefore even in the presence of intense electric fields their currents are weak [11]. The coupling between the electric field and ion migration can give rise to a permanent macro to micro-scale fluid instability, known as electroconvection. The electric force is described by

$$\mathbf{F}_E = q\,\mathbf{E} - \frac{1}{2}\,E^2\,\nabla\varepsilon + \frac{1}{2}\nabla\left[\rho\,\frac{d\varepsilon}{d\rho}\,E^2\right]. \tag{2.23}$$

In the Equation above, the first term is the Coulomb force: the force per unit volume exerted on a medium containing free charges, q. It is the strongest term and it is usually dominant in the presence of DC fields. The second term is called the dielectric force, and is exerted on non-homogeneous dielectric liquids. It is usually weaker than the Coulomb term and only exists in AC fields with periods much shorter than that

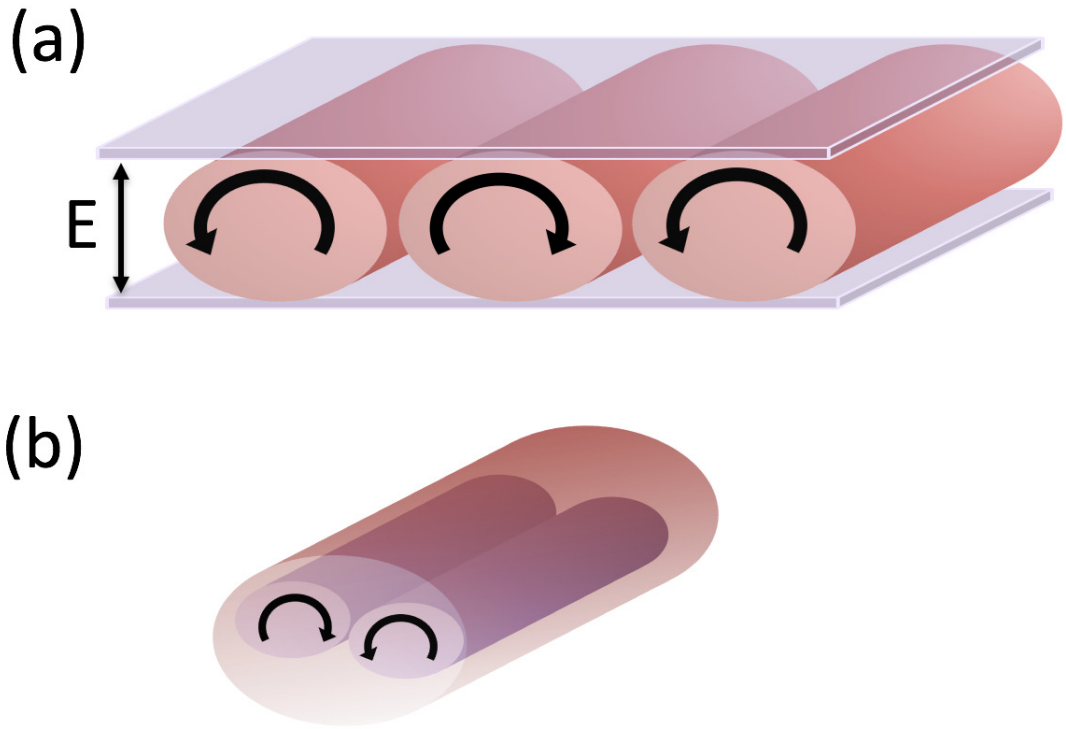

Figure 2.8: (a): Electroconvective rolls are shown by cylinders. Direction of rotation is shown by black arrows on cylinders. (b): The difference between one-roll and two-roll structures is shown by two convective rolls, as two-roll structure in purple, inside one-roll structure, in pink.

the charge relaxation time of the liquids. The third term is called the electrostrictive term and it is treated as a modification to the fluid pressure. In this term ρ is the mass density. These forces may act on bulk or at any possible interface between different liquids and lead to an instability [45, 46].

The instability produced by the electric force in the body of a liquid is described as a convective motion in the form of 3-dimensional rolls, very similar to what have been observed for traditional Rayleigh–Bénard convection, shown in FIG. 2.8(a). As opposed to thermal energy as the input in traditional Rayleigh–Bénard convection, here the electric energy is the source of convective instability and the first term in

Equation (2.23) is the primary force applied to the body of the liquid. If the conductivity of the liquid or unipolar charge injection is high enough, or the magnitude of electric force is much stronger than the magnitude of the viscous force, then one-roll structures turn into two-roll structure as shown in figure 2.8(b). Two-roll structures are reported theoretically in the work of Vázquez *et al.* [47] but to our knowledge they have not been reported experimentally.

Electrohydrodynamic instabilities have been studied in one major context: electroconvection induced by the presence of an electrical conductivity gradient explained first by Baygents *et al.* in 1998 [41] as a special case of electrohydrodynamic flows originally explained by LDM model [4, 12]. Different than the original LDM, electrohydrodynamic instability occurs due to charge separation, and molecular diffusion of conductivity, in the bulk of a single miscible fluid, not at the interface of two immiscible fluids. Electrohydrodynamic instability is due to dielectrophoretic forces that emerge from local electrical conductivity differences in the fluid, which in turn is caused by concentration gradients in the charge-carrying solutes. Baygents *et al.* explained that an electrohydrodynamic instability will be initiated if the electric Rayleigh number, Ra_E, see Equation (2.22), exceeds a threshold value of 1.4×10^4 for $\frac{\triangle\sigma}{\sigma_0} = 8$. They also explain the convective instability in terms of the relaxation time scales as follows: the instability grows with the electroviscous time scale as $\tau_{ev} \propto E_0^{-2}$, where E_0 is the applied field strength. On the other hand, molecular diffusion, with a time scale of $\tau_d = L^2/K_{eff}$, where L is length scale and K_{eff} is the effective diffusion coefficient, relaxes the conductivity gradient which is correlated with the charge accumulation and the strength of the electric body force. The electric Rayleigh number can also be defined in terms of relaxation times as $Ra_E = \tau_d/\tau_{ev}$. Therefore, the convective instability occurs only when the disturbance grows fast enough to overcome diffusive relaxation.

2.5 Order to disorder phase transitions

Phase transitions, or changes of state, are physical events that have been known for a very long time. Phase transitions depend on dimensionality, surface properties, defects, heating and cooling rates, and external fields. The first microscopic understanding of phase transitions was attempted by Johannes van der Waals in 1873. He presented a primitive theory of the gas-liquid transition which related the equation of state to a molecular model. The van der Waals picture focuses on short-ranged repulsive intermolecular forces and the longer ranged attractive forces in fluids and solids. These attractive interactions keeps the volume of the system constant while the arrangement and motions of molecules within the volume are determined by repulsive forces [48]. His approach laid down the main picture of the modern theoretical understanding of phase transitions.

The kinetics of phase transitions are difficult to study because of the combination of atomic length scales and short time scales. Hence, researchers have employed colloidal structures as a modern model system. Both colloids and atoms experience strong thermal motions and as a result they can form thermal equilibrium phases. Similar to atoms, colloidal particles have thermal energies on the order of k_BT. Like atoms, colloidal hard and soft spheres can undergo disorder to order phase transitions by varying different control parameters such as volume fraction, external electric or magnetic fields, light, physical confinements and temperature gradient. They can form gas, liquid, liquid crystal and crystal phase, and can also exhibit phase coexistence. In the ordered state, they can pack into different crystal structures, such as face-centred cubic (fcc), body-centred cubic (bcc), body-centred tetragonal (bct), body-centred orthorhombic (bco), as well as complex crystal structures. For a colloid diameter that is roughly 10^3 times bigger than atoms, the elastic moduli of resulting colloidal crystals is 10^9 times smaller than those of atomic crystals; therefore, they are also called soft

crystals. Unlike atoms, one can track easily colloidal particles [49, 50]. The kinetics of transitions have been studied experimentally by several techniques: bright field microscopy, confocal microscopy, fluorescent microscopy, static and dynamic light scattering, small angle X-ray scattering and small angle neutron scattering [51].

With colloidal systems, the kinetics of crystal nucleation from a fluid [52], crystal-crystal transition [53–55], and dynamics in glassy systems [56] have been studied. Yet, quantitative agreement between theory and experiment is lacking [51]. In addition, the kinetics of phase changes in driven systems that are very far from equilibrium have not been studied, with a few exceptions.

The concept of the phase transition has been also applied in diverse number of biological arenas: for example, cytoplasm can undergo a "gel-sol" transition [57]. Liquid-liquid demixing is also a well-known phase transition in cellular membranes. This mechanism is used to control endocytic or exocytic membrane transport which can be used either to transduce signals across the membrane or to carry out biochemical reactions [58]. Active matter systems and living cells have thus presented examples of non-equilibrium phase transitions.

Vesicles have also attracted lots of interest in their non-equilibrium shape phase transitions induced by external electric fields. A vesicle subjected to an external DC or AC electric field undergoes a dramatic shape deformation from circular to non-circular, prolate or oblate. The vesicle response to an electric field enables their use for drugs, protein, and DNA deliveries into living cells. The LDM is also employed to describe the electrohydrodynamics of membranes. While the LDM can explain steady-state deformation of vesicles, a "squaring shape" deformation remains unexplained [59]. The model system used in this thesis, a liquid-liquid emulsion with drop size of the order of micrometers, provides a means to tunably control hydrodynamic interactions and study structure and dynamics in real time.

2.6 Study of dynamics

The mobility of a particle reflects the mechanical properties of the environment. Mechanical properties of micro-scale environments can be quantified by a single particle trajectory or groups of trajectories. The relevant physical observables in which one is interested are averages. A common averaged quantity that is often calculated is the mean squared displacement, MSD. In what follows, the MSD in both simple Brownian motion and in anomalous diffusion, and their probability distribution of displacements is discussed.

2.6.1 Mean square displacement

A colloidal particle which undergoes random walk motion, for simplicity just in one dimension, can move just forward or backward. By adding together the steps, taking into account the fact that steps backwards subtract from the total, while steps forward add to the total, one is able to calculate the total distance from the starting point. Since both forward and backward steps are equally probable, the mean displacement sums up to zero. If however, instead of adding the distance of each step one adds the squares of the distances, it will always add a positive quantity to the total. In this case the sum will be some positive number, which grows larger with every step. The mean squared displacement gives a better indication of the magnitude of particles' motions. If one assumes each step happens at regular time intervals, one can easily see how the square distance grows with time. Einstein showed that it grows linearly with time [60] and in d dimension,

$$MSD = \langle (r(t) - r(0))^2 \rangle = 2dDt, \tag{2.24}$$

where D is the diffusion coefficient of colloidal particles. In normal diffusion the particle trajectories are characterized by irregular, but homogeneous independent small steps.

Normal diffusion in many natural phenomena close to equilibrium can also be understood from probability theory described by the central limit theorem. If a statistical quantity, random variable, is the sum of other statistical quantities, such as position of a random walker after large number of steps, n, and the steps are independent, and they have finite mean, M, and variance, $\sigma^2_{r_n}$, then the distribution of the random walker position, $P(r,t)$, is Gaussian. In particular, if $M = 0$ and $r_0 = 0$ and Δrs have the same variance then in d-dimensional space,

$$P(r,t) = \left(2\pi\sigma^2_{r_n}\right)^{-d/2} \exp\left(\frac{-r^2}{2\sigma^2_{r_n}}\right). \tag{2.25}$$

On the other hand, the MSD by definition is equal to the variance,

$$\left\langle \left(\Delta r\,(t)\right)^2 \right\rangle = \int (\Delta r)^2 P(r,t)\, d\Delta r = d\sigma^2_{r_n}. \tag{2.26}$$

Using Equation (2.24) one can get $\sigma^2_{r_n} = 2Dt$. So probability distribution function of the walker, PDF, 2.26, can be written in the form of [61]

$$P(r,t) = (4\pi Dt)^{-d/2} \exp\left(\frac{-r^2}{4Dt}\right). \tag{2.27}$$

2.6.2 Anomalous diffusion

Many different systems, far from equilibrium, show deviations from normal diffusion, faster or slower diffusion known as anomalous diffusion. Anomalous diffusion has been known since the work of Richardson in 1926 on fully developed turbulence,

when $MSD \propto t^3$ [62]. Anomalous diffusion can be studied in a more general scaling form of

$$MSD = 2dK_\gamma t^\gamma, \tag{2.28}$$

where d refers to the dimensionality of the system and K_γ is the generalized diffusion constant with dimension $[K_\gamma] = \mathrm{m}^2\mathrm{s}^{-\gamma}$, respectively. When $0 < \gamma < 1$, the dynamics is "sub-diffusive" and when $\gamma > 1$ the dynamics is "super-diffusive". In the case of $\gamma = 2$ the dynamics is termed as "ballistic". Brownian motion is a prototype of normal diffusion with $\gamma = 1$ [63–65].

Probability distribution of Brownian motion is usually Gaussian, there is a body of work [66] that addresses non-Gaussian Brownian, Fickian, diffusion. The probability distribution of anomalous diffusion is very likely non-Gaussian. Different anomalous diffusion phenomena have been described by different dynamical models such as continuous time random walk, CTRW [63–65], fractional Brownian motion, FBM [63–65] and motion in random velocity field, RVF [67, 68].

The continuous time random walk, CTRW, was introduced by Montroll *et al.* in 1965 [69] for the description of charge carrier motion in semiconductors. CTRW studies the motion of a particle that has to wait for a random waiting and trapping time before it makes a random jump. The length of each waiting time and jump is independent from their previous values [63–65].

FBM describes anomalous diffusion in the presence and in the absence of external forces. It was fully described by Mandelbrot *et al.* in 1968 [70]. FBM is a Gaussian self-similar process. For such processes observations that are far apart in time or in space are correlated strongly, indicating the presence of a long-range dependence. The

probability distribution of FBM in d dimension takes the form

$$P\left(r,t\right)=\left(4\pi K_{\gamma}t^{\gamma}\right)^{-d/2}\ \exp\left(\frac{-r^{2}}{4K_{\gamma}t^{\gamma}}\right), \tag{2.29}$$

where $0<\gamma\leq 2$ [63–65].

Enhanced diffusion with a $\gamma=3/2$ power law has been related to the random velocity field, RVF, model. It has been first described by Matheron *et al.* [71] in 1980 to understand water transport in microscopically heterogeneous rocks. The RVF model explains coupling between diffusion and convection by spatially random, but temporally static velocity fields, that leads to the superdiffusion. It describes a 2D stratified medium of homogeneous but distinct layers, such that transport properties vary between strata in x-direction. The fluid velocity varies from layer to layer randomly, while the pressure drops along strata. A particle diffuses in the fluid perpendicular to the direction of the flow. Redner [67, 68], Zumofen *et al.* [72], and Bouchaud *et al.* [73] obtained the probability distribution of displacements in d dimension for diffusion in random velocity fields,

$$P\left(r,t\right)=\left(At^{3/2}\right)^{-d/2}\ \exp\left(-\left(\frac{r^{2}}{4K_{\gamma}t^{3/2}}\right)^{\delta/2}\right), \tag{2.30}$$

where A is the normalization factor with dimension $[A]=m^{2}s^{-3/2}$, and K_{γ} is the generalized diffusion constant. δ is a parameter that is not fully determined within the model, but it should be $\delta\leq 1.7$, while the asymptotic behavior considering large displacements suggests $\delta\leq 4/3$ [67, 68].

2.6.3 Non-Gaussian parameter

The most important indicator of non-Gaussian behavior, or deviation of the shape of distribution function from Gaussian, is a parameter, known as Non-Gaussian parameter, α_2, and it was first introduced by Rahman [74] in 1964 as

$$\alpha_2 = \frac{\langle x^4 \rangle}{\left(1 + \frac{2}{d}\right) \langle x^2 \rangle^2} - 1, \tag{2.31}$$

where d is dimension, and $\langle x^4 \rangle$ and $\langle x^2 \rangle$ are the fourth and the second moments of probability distribution of displacements. For Brownian motion, $\alpha_2 = 0$, and it deviates from zero for non-Brownian diffusion.

2.6.4 MSD of a soft crystal

Structure and dynamics of order to disorder phase transitions can be studied in colloidal crystals in real space and real time. Detailed observation of microscopic order and dynamics can be achieved by video microscopy [75]. Interactions, dynamics, and elasticity of a charge-stabilized colloidal crystal were studied by Weiss *et al.* [76]. In this work, the microscopic interactions between pairs of colloids is related to the macroscopic parameters describing colloids' collective behavior. Each colloidal sphere diffuses in a potential of mean force created by interactions with its neighbors. In 3D, the potential, centered around each unit's equilibrium position, can be approximated by a harmonic well as

$$W(r) = \frac{1}{2} k r^2, \tag{2.32}$$

where r is the position of each sphere at time t and k is the harmonic constant. The probability density for a particle initially at location $\mathbf{r}$ to diffuse in a potential of mean force by a distance $\mathbf{\Delta r}$ is denoted by $P(\mathbf{\Delta r}, t \mid \mathbf{r})$. By getting an average over

all possible starting positions, $\mathbf{r}$, the probability for a particle to move by $\mathbf{\Delta r}$ in time t is $P(\mathbf{\Delta r}, t) = \int_{-\infty}^{\infty} P(\mathbf{\Delta r}, t \mid \mathbf{r})\, P(\mathbf{r})\, d\mathbf{r}$, where $P(\mathbf{r}) = \left(\frac{\beta k}{2\pi}\right)^{d/2} \exp\left(\frac{-\beta k r^2}{2}\right)$, d is the number of dimensions, and $\beta^{-1} = k_B T$. One can then get $P(\mathbf{\Delta} r, t)$ as

$$P(\mathbf{\Delta r}, t) = \frac{a^3}{\pi^{3/2}} \exp\left(-a^2 \mathbf{\Delta r^2}\right), \tag{2.33}$$

where $a = \dfrac{\dfrac{\beta k}{2} + \dfrac{1}{4Dt}}{\left(\beta k + \dfrac{1}{4Dt}\right)^{1/2}}$.

In one dimension, $P(\mathbf{\Delta r}, t)$ can be written in the form

$$P(\mathbf{\Delta} x, t) = \frac{a}{\pi^{1/2}} \exp\left(-a^2 \mathbf{\Delta} x^2\right). \tag{2.34}$$

The mean square displacement in one dimension is then written as

$$\langle \mathbf{\Delta} x^2 \rangle = \int_{-\infty}^{\infty} P(\mathbf{\Delta} x, t)\ \mathbf{\Delta} x^2\, d\mathbf{\Delta} x. \tag{2.35}$$

Replacing $P(\mathbf{\Delta} x, t)$ with the form in Equation (2.33), the MSD is given by

$$\langle \mathbf{\Delta} x^2 \rangle = \frac{1}{2} \frac{\beta k + \dfrac{1}{4Dt}}{\left(\dfrac{\beta k}{2} + \dfrac{1}{4Dt}\right)^2}. \tag{2.36}$$

In two dimensions, one can write the total MSD as

$$\langle \mathbf{\Delta} r^2 \rangle = \langle \mathbf{\Delta} x^2 \rangle + \langle \mathbf{\Delta} y^2 \rangle = \frac{\beta k + \dfrac{1}{4Dt}}{\left(\dfrac{\beta k}{2} + \dfrac{1}{4Dt}\right)^2}. \tag{2.37}$$

At two extreme time scales, $t \to 0$ and $t \to \infty$, the total MSD can be written in the

following forms:

$$\langle \mathbf{\Delta} r^2 \left(t \to 0\right) \rangle = 4Dt, \tag{2.38}$$

and

$$\langle \mathbf{\Delta} r^2 \left(t \to \infty\right) \rangle = \frac{4}{\beta k}. \tag{2.39}$$

At short times, the particles trapped in the mean force can diffuse with a diffusion coefficient D. At longer times, the particles are caged by nearest neighbors and MSD reaches an asymptotic value corresponding to the inverse of the harmonic constant. The plateau value of the MSD, at long times, corresponds to an effective Lindemann parameter, L_{eff}, that quantifies the distance from melting of a crystal. In the classical theory of melting, the Lindemann Parameter, L, is a unitless number; and it is related to the particles' mean square fluctuations. The asymptotic value is twice the variance of the displacement from the equilibrium position, $\langle \mathbf{\Delta} r^2 \left(t \to \infty\right) \rangle = 2 \left\langle \mathbf{\Delta r} \left(t\right) \cdot \mathbf{\Delta r} \left(t\right) \right\rangle = 2 \left(\langle \mathbf{\Delta r} \left(t\right)^2 \rangle - \langle \mathbf{\Delta r} \left(t\right) \rangle^2 \right)$ [77, 78]. L_{eff} in one dimension is defined by $L_{eff} = \frac{1}{d_{nn}} \sqrt{\frac{3}{2} \langle \mathbf{\Delta} x^2 \left(t \to \infty\right) \rangle}$, where d_{nn} is the nearest neighbor distance. In $2D$ and by using Equation (2.39) L_{eff} is given by [79]

$$L_{eff} = \frac{1}{d_{nn}} \sqrt{\frac{3}{4} \langle \mathbf{\Delta} r^2 \left(t \to \infty\right) \rangle} = \frac{1}{d_{nn}} \sqrt{\frac{3}{\beta k}}. \tag{2.40}$$

In the small systems studied, dynamical measures such as above have the advantage that they are single particle partial measures that are less sensitive to the detection of all the neighboring drops.

2.7 The study of structure

2.7.1 Bond-orientational order parameter

Halperin *et al.* in 1978 [80], described the theory of melting in two dimensions in terms of a bond orientational order parameter. They argued that as the crystal melts, defects in the crystal lattice appear. The defects stay closely associated with each other at early stages of melting. Later on, and at higher temperatures, the number of defects increases, they spread throughout the lattice, the long range orientational order disappears, and the matter becomes liquid. The local bond orientational order is given by

$$\Psi_N = \left| \frac{1}{N} \frac{\sum_{j=1}^{N} l_j e^{in\theta_j}}{\sum_{j=1}^{N} l_j} \right|, \tag{2.41}$$

where N is the number of nearest neighbors at lattice point j, l_j is the line segment that connects the neighbors $j-1$ and j, θ_j is the angle that the vector from the selected lattice point of j to the $j-1$th neighbor point of lattice makes with respect to the x axis. Ψ_N is calculated relative to either perfect 4-fold, for $n=4$, or 6-fold, for $n=6$, symmetry, which can vary between 1 and 0 where 1 indicates perfect n-fold symmetry [81, 82].

2.7.2 Pair correlation function

The radial distribution function or pair correlation function, $g(r)$, in a given system of atoms, molecules, or colloids describes how the density varies as a function of distance from a reference point. For a given image with total number of particles of N and

total area of A, $g(r)$ is defined by

$$g(r) = \frac{1}{N} \frac{\sum \frac{dn}{dA}}{\frac{N}{A}}, \tag{2.42}$$

where dn is the number of lattice points in a circle with radius r and area of dA. At very short distance, smaller than inter particle distance, $g(r)$ is equal to 0. For short distances, larger than inter particle distance, $g(r)$ is related to how the lattice points are packed together. For example, for a hard sphere system with particles with radius σ, the closest distance between two particles is 2σ. At larger distances, the probability of finding two particles with a given separation is roughly constant because the layers are more diffuse. At this limit, the density plays an important role. For instance, for systems with large density per area, it is more likely to find two particles at a given distance. $g(r)$ is normalized to density area, so at very large distance it goes to 1 as uniform probability. The radial distribution function is used to characterize the structure of the given system in terms of nearest neighbors. The first peak of $g(r)$ represents the position of the first nearest neighbors, the second peak shows the position of the second nearest neighbors and so on [83].

2.7.3 Temporal auto-correlation

A variable is "auto-correlated in time" if its value at a specific time is correlated with its values at other time. The auto-correlation, as a mathematical tool, is used for finding repeating patterns, such as the presence of a periodic signal obscured by noise. To explain the auto-correlation, one can assume that there are N observations as x_1, x_2, x_3, $\cdots$ and x_N on district time series. Therefore, one can form $(N-1)$ pairs of observations as (x_1, x_2), (x_2, x_3),$\cdots$, (x_{N-1}, x_N), while the first and the second

variables in each pair are at time t and $t+1$, respectively. The correlation between x_t and x_{t+1} for lag time $L = 1$ is given by

$$C_1 = \frac{\dfrac{\sum_{t=1}^{N-1} (x_t - \overline{x})(x_{t+1} - \overline{x})}{N-1}}{\dfrac{\sum_{t=1}^{N} (x_t - \overline{x})^2}{N}}, \tag{2.43}$$

where $\overline{x}$ is the average value of observations. For a large number of observations, $N - 1 \simeq N$, one can write

$$C_1 = \frac{\sum_{t=1}^{N-1} (x_t - \overline{x})(x_{t+1} - \overline{x})}{\sum_{t=1}^{N} (x_t - \overline{x})^2}. \tag{2.44}$$

Therefore, for L distance apart, or L lags, the auto-correlation is shown by [84]

$$C_L = \frac{\sum_{t=1}^{N-L} (x_t - \overline{x})(x_{t+L} - \overline{x})}{\sum_{t=1}^{N} (x_t - \overline{x})^2}. \tag{2.45}$$

In this thesis, in Chapter 5, the auto-correlation measurement is used to study the orientational dynamics of droplets as ellipses. The observations are $\cos(\theta - \theta_0)$, where θ and θ_0 are the angles of the fitted ellipse on the binary drop at times t and t_0, respectively.

Bibliography

[1] G. Taylor. Electrically driven jets. *Proceedings of the Royal Society of London. Series A, Mathematical and Physical Sciences*, 313(1515):453–475, 1969.

[2] C. T. O'Konski and H. C. Thacher. The distortion of aerosol droplets by an electric field. *The Journal of Physical Chemistry*, 57(9):955–958, 1953.

[3] R. S. Allan and S. G. Mason. Particle behaviour in shear and electric fields. I. deformation and burst of fluid drops. *Proceedings of the Royal Society of London. Series A, Mathematical and Physical Sciences (1934-1990)*, 267(1328):45–61, 1962.

[4] J. R. Melcher and G. I. Taylor. Electrohydrodynamics: A review of the role of interfacial shear stresses. *Annual Review of Fluid Mechanics*, 1(1):111–146, 1969.

[5] D. A. Saville. Electrohydrodynamics: The Taylor-Melcher leaky dielectric model. *Annual Review of Fluid Mechanics*, 29(1):27–64, 1997.

[6] E. Zholkovskij, J. Masliyah, and J. Czarnecki. An electrokinetic model of drop deformation in an electric field. *Journal of Fluid Mechanics*, 472:1–27, 2002.

[7] G. Supeene, C. R. Koch, and S. Bhattacharjee. Deformation of a droplet in an electric field: Nonlinear transient response in perfect and leaky dielectric media. *Journal of Colloid And Interface Science*, 318(2):463–476, 2008.

[8] S. Torza, R. G. Cox, and S. G. Mason. Electrohydrodynamic deformation and burst of liquid drops. *Philosophical Transactions of the Royal Society of London. Series A, Mathematical and Physical Sciences (1934-1990)*, 269(1198):295–319, 1971.

[9] S. D. Deshmukh and R. M. Thaokar. Deformation, breakup and motion of a perfect dielectric drop in a quadrupole electric field. *Physics of Fluids*, 24(3):032105, 2012.

[10] R. Thaokar. Dielectrophoresis and deformation of a liquid drop in a non-uniform, axisymmetric AC electric field. *The European Physical Journal E*, 35(8):1–15, 2012.

[11] T. Cameron, A. L. Yarin, and J. F. Foss, editors. *Springer handbook of experimental fluid mechanics*. Springer Berlin Heidelberg, Berlin, Heidelberg, 2007.

[12] G. I. Taylor. Studies in electrohydrodynamics. I. The circulation produced in a drop by electrical field. *Proceedings of the Royal Society of London. Series A, Mathematical and Physical Sciences (1934-1990)*, 291(1425):159–166, 1966.

[13] A. Varshney. *Structure formation and mechanical response of model amorphous systems*. PhD thesis, School of Natural Science, Tata Institute of Fundamental Research, India, 2013.

[14] Z. Wang, Q. Dong, Y. Zhang, J. Wang, and J. Wen. Numerical study on deformation and interior flow of a droplet suspended in viscous liquid under steady electric fields. *Advances in Mechanical Engineering*, 6(5):1–12, 2014.

[15] N. Bentenitis and S. Krause. Droplet deformation in dc electric fields: the extended leaky dielectric model. *Langmuir*, 21(14):6194–209, 2005.

[16] P. F. Salipante and P. M. Vlahovska. Electrohydrodynamics of drops in strong uniform dc electric fields. *Physics of Fluids*, 22(11), 2010.

[17] P. F. Salipante and P. M. Vlahovska. Electrohydrodynamic rotations of a viscous droplet. *Physical Review E*, 88(4):043003, 2013.

[18] J. Ha and S. Yang. Electrohydrodynamics and electrorotation of a drop with fluid less conductive than that of the ambient fluid. *Physics of Fluids*, 12(4):764–772, 2000.

[19] G. Quincke. Ueber rotationen im constanten electrischen Felde. *Annalen der Physik*, 295(11):417–486, 1896.

[20] D. Das and D. Saintillan. Electrohydrodynamics of viscous drops in strong electric fields: numerical simulations. *Journal of Fluid Mechanics*, 829:127–152, 2017.

[21] A. Varshney, S. Ghosh, S. Bhattacharya, and A. Yethiraj. Self organization of exotic oil-in-oil phases driven by tunable electrohydrodynamics. *Scientific Reports*, 2:738, 2012.

[22] A. Varshney, S. Gohil, M. Sathe, S. Rao RV, J. B. Joshi, S. Bhattacharya, A. Yethiraj, and S. Ghosh. Multiscale flow in an electro-hydrodynamically driven oil-in-oil emulsion. *Soft Matter*, 12(6):1759–1764, 2016.

[23] S. Khajehpour Tadavani, J. R. Munroe, and A. Yethiraj. The effect of confinement on the electrohydrodynamic behavior of droplets in a microfluidic oil-in-oil emulsion. *Soft Matter*, 12(45):9246–9255, 2016.

[24] J. C. Baygents and D. A. Saville. The circulation produced in a drop by an electric field: A high field strength electrokinetic model. *AIP Conference Proceedings*, 197(1):7–17, 1990.

[25] O. Schnitzer and E. Yariv. The Taylor–Melcher leaky dielectric model as a macroscale electrokinetic description. *Journal of Fluid Mechanics*, 773:1–33, 2015.

[26] M. Bazant. Electrokinetics meets electrohydrodynamics. *Journal of Fluid Mechanics*, 782:1–4, 2015.

[27] The Los Alamos accelerator code group - Web Services, http://laacg.lanl.gov/laacg/services/download_sf.phtml.

[28] H. P. Zappe and C Duppé, editors. *Tunable micro-optics*. Cambridge University Press, Cambridge, England, 1st edition, 2016.

[29] O. Reynolds. An experimental investigation of the circumstances which determine whether the motion of water shall be direct or sinuous, and of the law of resistance in parallel channels. *Philosophical Transactions of the Royal Society of London*, 174(0):935–982, 1883.

[30] P. K. Kundu. *Fluid mechanics*. Academic Press, Burlington, 4th edition, 2010.

[31] G. Hauke. *An Introduction to fluid mechanics and transport phenomena*. Fluid Mechanics and Its Applications. Springer Netherlands, Dordrecht, 2008.

[32] O. M. F. R. S. Lord Rayleigh. On convection currents in a horizontal layer of fluid, when the higher temperature is on the under side. *The London, Edinburgh, and Dublin Philosophical Magazine and Journal of Science*, 32(192):529–546, 1916.

[33] B. P. van Poppel, O. Desjardins, and J. W. Daily. A ghost fluid, level set methodology for simulating multiphase electrohydrodynamic flows with application to liquid fuel injection. *Journal of Computational Physics*, 229(20):7977–7996, 2010.

[34] J. Q. Feng. Electrohydrodynamic behaviour of a drop subjected to a steady uniform electric field at finite electric Reynolds number. *Proceedings of the Royal Society A: Mathematical, Physical and Engineering Sciences*, 455(1986):2245–2269, 1999.

[35] J. Q. Feng and T. C. Scott. A computational analysis of electrohydrodynamics of a leaky dielectric drop in an electric field. *Journal of Fluid Mechanics*, 311(1):289–326, 1996.

[36] J. D. Sherwood. Breakup of fluid droplets in electric and magnetic fields. *Journal of Fluid Mechanics*, 188:133–146, 1988.

[37] R. Karyappa, S. Deshmukh, and R. Thaokar. Breakup of a conducting drop in a uniform electric field. *Journal of Fluid Mechanics*, 754:550–589, 2014.

[38] R. Pillai, J. D. Berry, D. J. E. Harvie, and M. R. Davidson. Electrokinetics of isolated electrified drops. *Soft Matter*, 12(14):3310–3325, 2016.

[39] H. Nganguia, Y. Young, A. T. Layton, M. Lai, and W. Hu. Electrohydrodynamics of a viscous drop with inertia. *Physical Review E*, 93(5):053114, 2016.

[40] J. Wu, P. Traoré, P. A. Vázquez, and A. T. Pérez. Onset of convection in a finite two-dimensional container due to unipolar injection of ions. *Physical Review E*, 88(5):053018, 2013.

[41] J. C. Baygents and F. Baldessari. Electrohydrodynamic instability in a thin fluid layer with an electrical conductivity gradient. *Physics of Fluids*, 10(1):301–311, 1998.

[42] M. Orlik. *Self-Organization in electrochemical systems II spatiotemporal patterns and control of chaos*. Monographs in Electrochemistry. Springer, Berlin, Heidelberg, 2012.

[43] H. Bénard. Les tourbillons cellulaires dans une nappe liquide. - Méthodes optiques d'observation et d'enregistrement. *Journal de Physique Théorique et Appliquée*, 10(1):254–266, 1901.

[44] J. R. A. Pearson. On convection cells induced by surface tension. *Journal of Fluid Mechanics*, 4(5):489–500, 1958.

[45] A. Castellanos. Coulomb-driven convection in electrohydrodynamics. *IEEE Transactions on Electrical Insulation*, 26(6):1201–1215, 1991.

[46] P. Atten. Electrohydrodynamic instability and motion induced by injected space charge in insulating liquids. *IEEE Transactions on Dielectrics and Electrical Insulation*, 3(1):1–17, 1996.

[47] P. A. Vázquez, G. E. Georghiou, and A. Castellanos. Numerical analysis of the stability of the electrohydrodynamic (ehd) electroconvection between two plates. *Journal of Physics D: Applied Physics*, 41(17):10, 2008.

[48] D. Chandler, J. D. Weeks, and H. C. Andersen. Van der waals picture of liquids, solids, and phase transformations. *Science*, 220(4599):787–94, 1983.

[49] W. Poon. Colloids as big atoms. *Science*, 304(5672):830–831, 2004.

[50] B. Li, D. Zhou, and Y. Han. Assembly and phase transitions of colloidal crystals. *Nature Reviews Materials*, 1(2):15011, 2016.

[51] A. Yethiraj. Tunable colloids: control of colloidal phase transitions with tunable interactions. *Soft Matter*, 3(9):1099–1115, 2007.

[52] U. Gasser, E. R. Weeks, A. Schofield, P. N. Pusey, and D. A. Weitz. Real-space imaging of nucleation and growth in colloidal crystallization. *Science*, 292(5515):258–62, 2001.

[53] A. Larsen and D. Grier. Like-charge attractions in metastable colloidal crystallites. *Nature*, 385(6613):230–233, 1997.

[54] A. Yethiraj and A. Van Blaaderen. A colloidal model system with an interaction tunable from hard sphere to soft and dipolar. *Nature*, 421(6922):513–7, 2003.

[55] P. Mohanty, P. Bagheri, S. Nöjd, A. Yethiraj, and P. Schurtenberger. Multiple path-dependent routes for phase-transition kinetics in thermoresponsive and field-responsive ultrasoft colloids. *Physical Review X*, 5(1), 2015.

[56] E. R. Weeks, J. C. Crocker, A. C. Levitt, and D. A. Weitz. Three-dimensional direct imaging of structural relaxation near the colloidal glass transition. *Science*, 287(5453):627–31, 2000.

[57] G. H. Pollack. Cells, gels and the engines of life. (A new, unifying approach to cell function). *Annals of Botany*, 91(3):404–405, 2001.

[58] A. Hyman and K. Simons. Cell biology. Beyond oil and water-phase transitions in cells. *Science*, 337(6098):1047–9, 2012.

[59] A. Iglic, editor. *Advances in planar lipid bilayers and liposomes*, volume 12. Elsevier, Oxford, UK, 2010.

[60] D. F. Evans and H. Wennerström. *The colloidal domain: where physics, chemistry, biology, and technology meet*. Advances in interfacial engineering series. VCH Publishers, New York, NY, 1994.

[61] L. Vlahos, H. Isliker, Y. Kominis, and K. Hizanidis. Normal and anomalous aiffusion: A tutorial. *arXiv:0805.0419*.

[62] L. F. Richardson. Atmospheric diffusion shown on a distance-deighbour draph. *Proceedings of the Royal Society of London. Series A, Containing Papers of a Mathematical and Physical Character*, 110(756):709–737, 1926.

[63] R. Metzler and J. Klafter. The random walk's guide to anomalous diffusion: a fractional dynamics approach. *Physics Reports*, 339(1):1–77, 2000.

[64] R. Metzler and J. Klafter. The restaurant at the end of the random walk: recent developments in the description of anomalous transport by fractional dynamics. *Journal of Physics A: Mathematical and General*, 37(31):R161–R208, 2004.

[65] R. Metzler, J. H. Jeon, A. G. Cherstvy, and E. Barkai. Anomalous diffusion models and their properties: non-stationarity, non-ergodicity, and ageing at the centenary of single particle tracking. *Physical Chemistry Chemical Physics*, 16(44):24128–24164, 2014.

[66] B. Wang, J. Kuo, S. Bae, and S. Granick. When Brownian diffusion is not Gaussian. *Nature Materials*, 11(6):481–5, 2012.

[67] S. Redner. Superdiffusive transport due to random velocity field. *Physica D*, 38:287–290, 1989.

[68] S. Redner. Superdiffusion in random velocity fields. *Physica A*, 168:551–560, 1990.

[69] E. W. Montroll and G. H. Weiss. Random walks on lattices. II. *Journal of Mathematical Physics*, 6(2):167–181, 1965.

[70] B. B. Mandelbrot and J. W. Van Ness. Fractional Brownian motions, fractional noises and applications. *Society for Industrial and Applied Mathematics Review*, 10(4):422–437, 1968.

[71] G. Matheron and G. de Marsily. Is transport in porous media always diffusive? A counterexample. *Water Resources Research*, 16(5):901–917, 1980.

[72] G. Zumofen, J. Klafter, and A. Blumen. Enhanced diffusion in random velocity fields. *Physical Review A*, 42(8):4601–4608, 1990.

[73] J. P. Bouchaud, A. Georges, J. Koplik, A. Provata, and S. Redner. Superdiffusion in random velocity fields. *Physical Review Letters*, 64(21):2503–2506, 1990.

[74] A. Rahman. Correlations in the motion of atoms in liquid argon. *Physical Review*, 136(2A):A405–A411, 1964.

[75] J.C. Crocker and D. G. Grier. Methods of digital video microscopy for colloidal studies. *Journal of Colloid And Interface Science*, 179(1):298–310, 1996.

[76] J. A. Weiss, A. E. Larsen, and D. G. Grier. Interactions, dynamics, and elasticity in charge-stabilized colloidal crystals. *The Journal of Chemical Physics*, 109(19):8659–8666, 1998.

[77] J. Bongers and H. Versmold. Microscopic investigations of the single particle dynamics in colloidal crystals. *The Journal of Chemical Physics*, 104(4):1519–1523, 1996.

[78] Y. N. Ohshima and I. Nishio. Colloidal crystal: bead–spring lattice immersed in viscous media. *The Journal of Chemical Physics*, 114(19):8649–8658, 2001.

[79] A. M. Alsayed, M. F. Islam, J. Zhang, P. J. Collings, and A. G. Yodh. Premelting at defects within bulk colloidal crystals. *Science*, 309(5738):1207–10, 2005.

[80] B. I. Halperin and D. R. Nelson. Theory of two-dimensional melting. *Physical Review Letters*, 41(2):121–124, 1978.

[81] C. A. Murray. *Bond-orientational order in condensed matter systems.* Partially Ordered Systems. Springer-Verlag, New York, 1992.

[82] A. Yethiraj, A. Wouterse, B. Groh, and A. van Blaaderen. Nature of an Electric-Field-Induced Colloidal Martensitic Transition. *Physical Review Letters*, 92(5):058301, 2004.

[83] D. C. Rapaport. *The art of molecular dynamics simulation*. Cambridge University Press, Cambridge, UK, 2nd edition, 2004.

[84] P. F. Dunn. *Measurement and data analysis for engineering and science*, volume 26. CRC Press, 2nd edition, 2010.

Chapter 3

Experimental techniques

3.1 Cell preparation

3.1.1 Simple cells for uniform electric fields

FIG. 3.1 shows a photograph and a schematic of a cell with electric field perpendicular to the microscope slide and parallel to the gravity. More detailed schematic designs are shown in FIG. 4.1. An indium tin oxide (ITO) cover glass slide (SPI), which is both optically transparent and electrically conductive, is glued to a microscope slide with an ultraviolet-curing optical adhesive (Norland Optical Adhesive 61) and cured under an ultraviolet lamp (UV lamp Spectroline model $SB-100P$) for 10 min. The glass or plastic spacers with defined thicknesses are glued to the bottom plate and cured under the UV lamp to give a sample thickness d, shown in FIG. 3.1(b). A second ITO slide is glued to the spacers and cured with the same method. To prevent accumulation of charge at the edges of both ITO slides, the ITO coated regions at the edges are removed using hydrochloric acid ($36.5-38\%$). The wire connections to the top and bottom plate are made by a silver paste (Canemco Inc.). After drying the silver, the connection area is glued and cured in the same way.

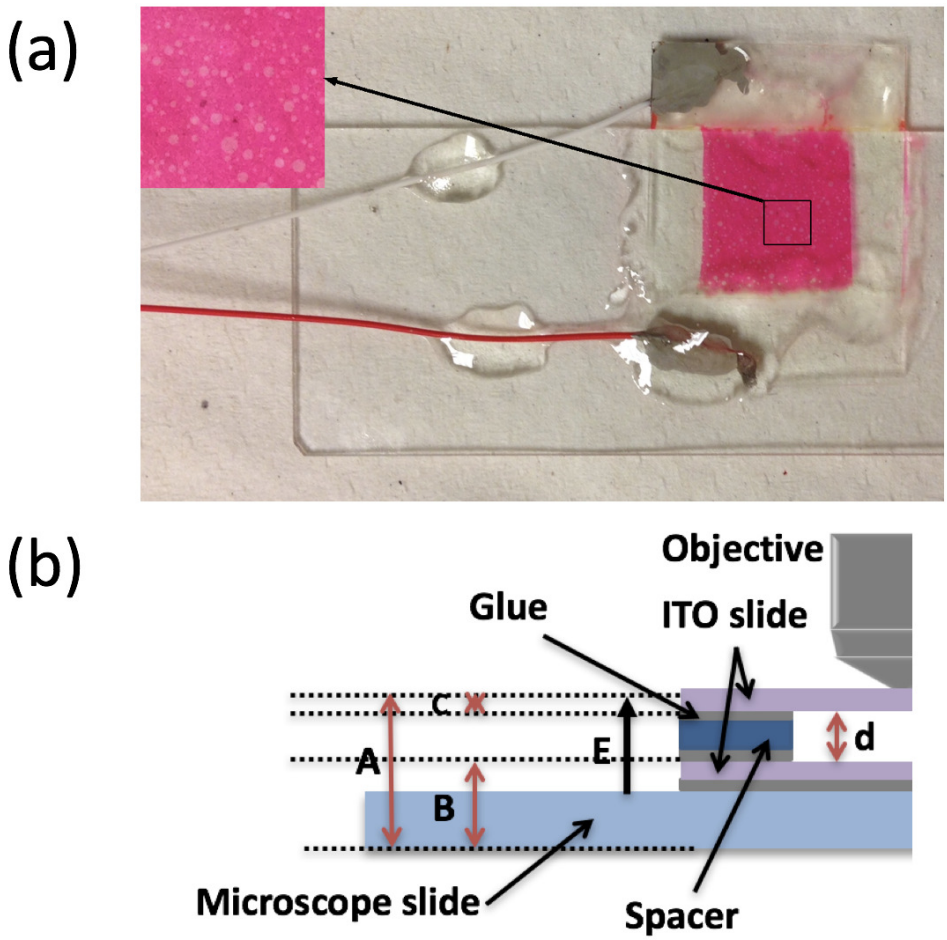

Figure 3.1: (a): A photograph of a sample cell. The inset shows castor oil, dyed in Nile Red, and silicone oil drops with pale color. (b): A side view of the cell. The cell thickness, d, is defined by $d = A - B - C$. Electric field is perpendicular to the substrate and parallel to gravity.

The thickness of the cell is $d = A - B - C$, FIG. 3.1(b), where A is the total thickness, B is the thickness of microscope slide plus the first layer of glue plus the thickness of the ITO bottom plate, and C is the thickness of the top ITO plate. A, B, and C are all measured using a micrometer.

To apply the DC electric field, Chapter 4, a DC power generator (Kepco, $0 - 1500$ V) was used and the magnitude of the applied voltage on the cell is checked by a multimeter (model 4C21, BK precision). A DC high voltage power supply (Xerox

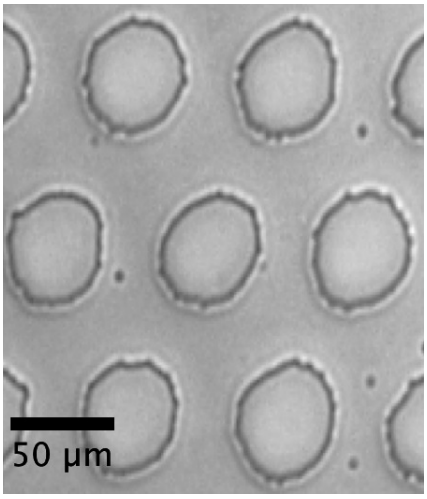

Figure 3.2: A hexagonal array of roughly circular ITO-free regions is etched by the photo-lithography technique.

model $HV - 1543$, $0 - 10000$ V) was also used in some experiments.

To apply an AC electric field, Chapters 5 and 6, a sinusoidal AC voltage (Tektronix model $AFG3022$) was applied to the cell, while the output voltage of the power generator was amplified by a high voltage amplifier (Trek model $PZD2000A$).

3.1.2 Patterned cells for non-uniform fields

In this configuration, the cell construction is unchanged, but the ITO bottom plate has been selectively etched by photo-lithography such that a hexagonal array of roughly circular ITO-free regions, diameter $\sim$ 50 μm and with nearest-neighbor center-to-center spacing $\sim$ 100 μm, is obtained. An optical micrograph of the bottom plate after etching is shown in FIG. 3.2. The steps to make the pattern are summarized below:

1. Wash ITO slide with ethanol.

2. Spin coat 555 μL of the photoresist $S1813$ (Microchem), on the ITO slide at 4000 rpm for 30 s.

3. Soft bake: place the ITO slide on the hot plate at 110 °C for 1 min.

4. Expose: expose those areas of ITO where supposed to be removed for 10 s using an $SF100$ mask-less patterning system (MPS, Intelligent Micro Patterning).

5. Develop: immediately submerse in $NaOH$ 0.5% by volume for 30 s and wash with water and repeat this process 3 times.

6. Unmount ITO: submerse the ITO slide in concentrated HCl for 30 s.

7. Wash with water and dry the ITO slide with the air gun.

The experiments using the patterned electrode were carried out in an AC electric field at different frequencies. A sinusoidal AC voltage (model AFG3022, Tektronix) is applied to the cell over the frequency range of 0.01 to 100 Hz. The output voltage of the power generator is amplified by a high voltage amplifier (model PZD2000A, Trek). The maximum achievable voltage with this set up is $0 - 1000V$, over the frequency range of $0 - 25MHz$.

3.1.3 Materials

The oils that are used within the experiment are silicone oil and castor oil. Castor oil, $C57H104O9$, is a weakly polar and colorless to very pale yellow liquid. Silicone oil, $[-Si(CH3)2O-]n$, is also a transparent oil with polarity much less than that of castor oil. In experiments with only silicone oil, castor oil is dyed with a fluorescent polar dye called "Nile Red" with the molecular formula of $C20H18N2O2$, while in most of cases the bright field microscopy is used. The Nile Red dye does not mix with silicone oil and so it is a perfect choice for the emulsion of silicone oil and castor oil. Experiments were carried out with and without the dye: no difference in experimental

	silicone oil	castor oil	PMMA
Radius $[\mu m]$			0.5
Dielectric constant $\varepsilon/\varepsilon_0$	2.4	3.6	2.6
Conductivity σ $[S/m]$	3.95×10^{-11}	4.0×10^{-10}	
Viscosity μ $[Pa.s]$	0.137	0.819	
Density ρ $[g/cm^3]$	1.047	0.960	1.26
Diffusion coefficient D $[m^2/s]$		2.02×10^{-12}	

Table 3.1: Table of materials' constants.

frequency dependences were noted. Table 3.1 is a list of materials' constants for the silicone oil, castor oil, and PMMA particles used in this thesis.

3.1.4 Cell filling

In the first sets of experiments, chapter 4, the cell is either filled by pipetting an emulsion of silicone oil (Dow Corning 550, Dow Corning Co.), and castor oil (castor oil huile de rain, NOW foods), in a volume ratio of 1 : 16, or PMMA particles and castor oil with mass ratio of 1:11000. In the experiment with Nile red and castor oil the mass ratio was 1:218 of dye to castor oil. In the second sets of experiments, chapter 5, one uses an emulsion of silicone oil and castor oil in a volume ratio of 1 : 16. In the third sets of experiments, chapter 6, the cell is filled by the same emulsion as the second cell while fluorescent PMMA particles are also added in order to track the fluid motion. To fill the cells one follows a simple procedure. The pipette is brought near one entrance to the cell. Due to the capillary action, the suspension is sucked into the cell. Any excess solution at the edge is then wiped off. The cell is sealed and glued with UV epoxy and cured for 15 min.

3.2 Optical microscopy

In the experiments carried out in this thesis, a Nikon Eclipse $80i$ upright and a Nikon Eclipse $TE2000-U$ inverted optical and confocal microscopes were used. A high speed water-cooled digital sCMOS, scientific complementary metal oxide semiconductor, camera (pco.edge 5.5) with a frame rate of 100 frames/s (fps) at full resolution of 2560×2160 pixel as a full download stream to the PC, is mounted on the microscope rear ports. The data, depending on the sample, is collected by two different microscopy techniques: bright field microscopy and fluorescence microscopy.

3.2.1 Bright field microscopy

Bright field microscopy (BFM), which yields dark objects on a bright background, is the simplest technique for optical microscopy. In BFM, carried out with an upright microscope, the light source is positioned below the sample. Light then propagates through the sample, and is observed by the objective lens and sensor, which are positioned above the sample. The simplicity of BFM is the main reason this technique is so popular in optical microscopy. The BFM has a lower contrast compared to other optical techniques like fluorescence microscopy and confocal microscopy.

The common illumination technique that is used in optical microscopy is called Kohler illumination. In Kohler illumination, there are two sets of principal conjugate focal planes that occur along the optical pathway through the microscope. One set consists of four field planes, referred to as the field or image-forming conjugate set, while the other one consists of four aperture planes, referred to as the illumination conjugate set. Each plane within a set is conjugated with the others in that set because they are simultaneously in focus and can be viewed superimposed upon one another when observing specimens through the microscope [1].

3.2.2 Fluorescence microscopy

If light is incident on a molecule, it may absorb the light and then emit light of a different color, a process known as fluorescence. After absorbing a photon of light in the ground state, the molecule can move to an excited state with higher energy. Within 10^{-8} s, the molecule dissipates some of the absorbed energy, due to the collisions with the surrounding molecules, and drops to a lower energy. Eventually, the molecule undergoes an emission and drops to its ground state and in this process it emits light with lower energy and a higher wavelength. The wavelengths of the excitation light and the color of the emission light are material dependent. In fluorescence microscopy, the entire field of view is completely illuminated and all fluorophores that are illuminated fluoresce at the same time [2]. Fluorescence microscopy uses a light source, in this case a mercury lamp, which emits light over a broad wavelength. A filter is used to allow a narrow wavelength bandwidth of light to enter the region of interest. The sample with a fluorescent dye will be excited and will emit light at a longer wavelength (lower energies than the excitation). The emitted light will pass through a dichromatic mirror that reflects light shorter than a certain wavelength but transmits light of a longer wavelength. The emission light is recorded with a monochrome camera. The intensity from the full range of emission spectrum of the fluoresce is recorded in one grey-scale image, under a range of 0 to 256 for 8-bit recording. The fluorescent objects are shown from white to grey, depending on the located plane with respect to the objective, in a black background.

The recent introduction of sCMOS cameras enables high-speed imaging at the relatively low light level of fluorescent microscopy.

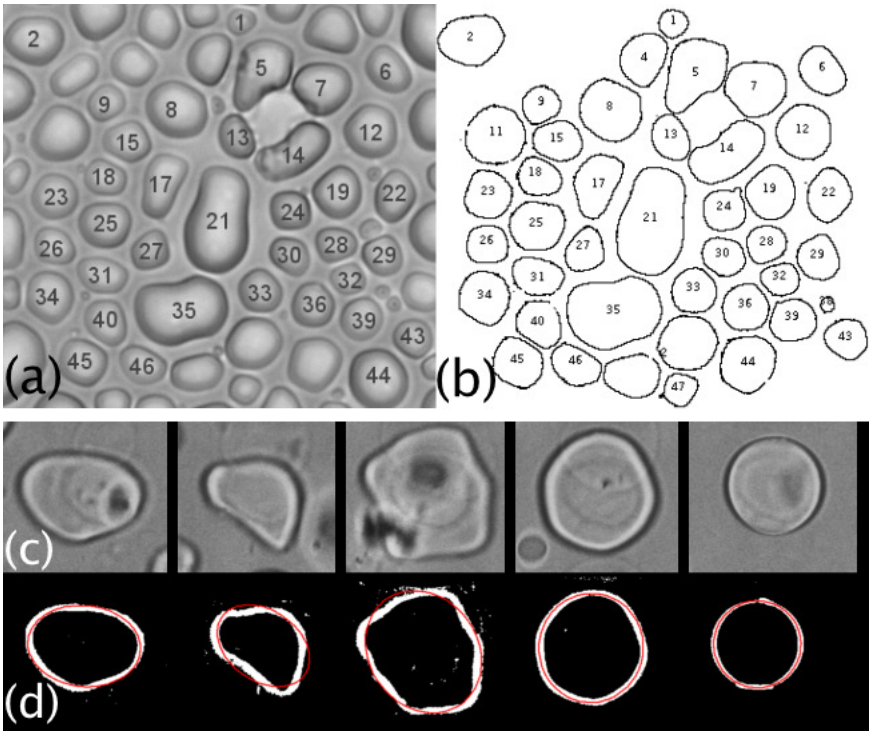

Figure 3.3: (a): For the thickness dependent experiments: An 8-bit image of droplets in a small portion of field of view. (b): The same image in grey scale while the edge of drops are found by Analyze Particle code. (c): For order to disorder transition experiments: 8-bit images of droplets located on patterned spots. (d) The same images while ellipses are fitted on the edge of drops in red.

3.3 Image processing: 2D particle tracking

Particle tracking is a technique to investigate the position of objects as a function of time. The "particle tracks" gives the coordinates of objects over a series of time steps. This enables one to understand what is happening to each object motion as a function of time.

After recording a movie, the coordinates of the objects are found by three different methods depending on whether the objects are drops or fluorescent colloidal particles like PMMA. Drops are non-spherical objects with sharp boundaries that lend themselves well to an edge finding and/or an ellipse fitting algorithm. Monodisperse,

spherical fluorescent particles typically exhibit a roughly parabolic intensity profile, whose extent is predictable (because of monodispersity). In this case, matrix convolution methods can yield particle centers to sub-pixel resolution. In the following, these methods are discussed.

3.3.1 The edge finding method

Edge detection is a very important area in the field of image processing. Edges characterize boundaries and are therefore a problem of fundamental importance in image processing. Edges in images are areas with strong intensity contrasts, a jump in intensity from one pixel to the next. Edge detecting significantly reduces the amount of data and filters out useless information, while preserving the important structural properties in an image.

A well known "Canny edge detector" created by Canny in 1988, is widely considered to be the standard edge detection algorithm in the industry. The Canny edge detector first smooths the image to eliminate noise. It then finds the image gradient to highlight regions with high spatial derivatives. The algorithm then tracks along these regions and suppresses any pixel that is not at the maximum. The gradient array is now further reduced by hysteresis. Hysteresis is used to track along the remaining pixels that have not been suppressed. Hysteresis uses two thresholds and if the magnitude is below the first threshold, it is set to zero, and made a nonedge. If the magnitude is above the high threshold, it is made an edge. If the magnitude is in between two thresholds, then it is set to zero unless there is a path from this pixel to a pixel with a gradient above the highest threshold [3].

Experiments studying the effect of confinement with a simple electrode, chapter 4, were carried out by BFM. When the data set is recorded, a computer program using the edge finding method is employed to find the edges of the drops based on the gra-

dient of image intensity, FIG. 3.3(a)-(b). FIG. 3.3(a) shows the original image, while FIG. 3.3(b) shows the results of the edge finding procedure. The drop numbers, after edge finding, have been super-imposed on the original figure in FIG. 3.3(a). This code is programmed in Fiji which is an open source Java-based image processing package developed at the National Institute of Health. The code used is called "Analyze Particles" and has two different parameters: size and circularity. The size parameter can vary between zero and infinity depending on the size of the drops, while the circularity can change between zero and one, representing the non-circular and perfect-circular drops, respectively. To ignore noise due to the low quality of images, which can cause even a small shadow in the background of the image to be recognized as a small drop, the size parameter is set between $100 - 1000$ pixel^2. The circularity varies between 0.4 and 1 due to the fact that sometimes the nearest drops are recognized as one drop with a circularity close to zero, or a drop shadow is considered as a part of the drop and makes the edge non-circular. For every single frame in a stack the center of mass, (x, y), and the area of the drops are measured and saved as a text file in the pixel scale.

3.3.2 The method to fit ellipse

For experiments studying the non-equilibrium disordering of a droplets crystal, Chapter 5, experiments were carried out on a patterned electrode and recorded by BFM. To study the orientational dynamics of droplets, an ellipse-fitting algorithm was used. In this approach, one uses the curve and surface fitting method. To the lowest order, a deformed circle can be approximated as an ellipse, FIG. 3.3 (c)-(d). The code, which is available freely [4], is programmed in IDL (Interactive Data Language by Exelis Visual Information Solutions). IDL is a commercial programming language package that is popular for data analysis of a large set of images and is often used

for astronomy and colloidal systems. First, an 8-bit grey scale image is converted to a binary image, while the edge of the drops have the highest intensity value. In order to minimize the search area, a square box of interest is created around each patterned drop. Then, by filtering out the lower values of intensity and evaluating the edge position of the patterned drop in pixel and in the box of interest, an ellipse can be fitted on the edge. To get a more precise fit for a noisier image, when patterned drops are surrounded by many tiny droplets, a clustering algorithm written in IDL is used. This algorithm filters out the high-intensity spots that are not part of patterned drops in the box of interest. The output consists of the major axis M, the minor axis m, centroid (x, y), and angle of the major axis with respect to the x-axis. The output is then saved as *gdf* files in pixel scale.

3.3.3 Fluorescent PMMA particle tracking

For fluorescent PMMA particles, the data set is recorded by fluorescence microscopy. The stack of images is then analysed using a computer program that is coded in IDL. The IDL codes used in this project are described by Crocker and Grier [5] and are available freely [6]. The code obtains the centroid of each colloidal particle and assigns an ID to every particle in every frame. To do so, at least two parameters should be well-defined: the "diameter", a value a little greater than the actual diameter of the particles but smaller than their separation, and "separation", the minimum allowed separation between the centers of particles. Through standard image convolution produces, the x and y of centroids are calculated, in pixels, and then converted to μm.

3.4 Particle image velocimetry

Particle image velocimetry, PIV, is a common technique for fluid flow measurement and provides velocity fields. In an ideal PIV measurement, the displacement of tracer particles over a small time interval extracts the local fluid velocity. The assumption is that the velocity of the tracers is the same as the flow velocity. The particles are illuminated in a plane of the flow. The light scattered by the particles is recorded as images. In PIV, one computes the cross-correlation of two images with a given "lag" in time. The displacement of the particles is given by the lag with the largest correlation. The frames are split into a large number of interrogation areas, or windows. Then the displacement vector for each window is calculated. In this project an open source PIV implementation called "Civx", programmed in Fortran, is used [7, 8]. Also, the droplets themselves are used as tracer particles to measure displacement between consecutive frames. Windows with a size of twice the drop size are used and the displacement is estimated from the movement of the droplets.

3.5 Image pre-processing

In this thesis, different methods of image processing have been employed. In chapter 4, the "Enhance Contrast", "Sharpen Image", and "Gaussian Filter" operations, from FIJI (ImageJ), were used to improve the quality of the images prior to binarizing the image. The "Analyze Particle" code was then run (in FIJI) on these binarized images. These pre-processing steps are admittedly very qualitative because the grey-scale images vary in quality from experiment to experiment. In chapter 5, images were converted to binary, using the "Invert" option in FIJI (ImageJ): this makes the edges of the drops black, and they are surrounded by a white background. Next, the movies were scaled by 1/4 in order to make the image processing faster (this practical

step is not essential). The final distances (in pixels), after processing, were multiplied by 4. In chapter 6 before analyzing the data, the brightness of all frames have been enhanced using the "Adjust Brightness and Contrast" (and the "Auto" setting within it) in FIJI (ImageJ).

Bibliography

[1] A. Kohler. New method of illumination for phomicrographical purposes. *Journal of the Royal Microscopical Society*, 14:261–261, 1984.

[2] D. Semwogerere and E. R. Weeks. Confocal microscopy. In *In Encyclopedia of Biomaterials and Biomedical Engineering, Biomaterials, Biomedical Engineering. Informa Healthcare*, pages 705–714. CRC Press, 2008.

[3] J. Canny. A Computational approach to edge detection. *IEEE Transactions on Pattern Analysis and Machine Intelligence*, PAMI-8(6):679–698, 1986.

[4] M. Wardt. IDL curve fitting and function optimization, https://www.physics.wisc.edu/~craigm/idl/fitting.html.

[5] J. C. Crocker and D. G. Grier. Methods of digital video microscopy for colloidal studies. *Journal of Colloid and Interface Science*, 179(1):298–310, April 1996.

[6] J. C. Crocker and E. R. Weeks. Particle tracking using IDL, http://www.physics.emory.edu/faculty/weeks//idl/.

[7] A. M. Fincham and G. R. Spedding. Low cost, high resolution DPIV for measurement of turbulent fluid flow. *Experiments in Fluids*, 23(6):449–462, 1997.

[8] A. Fincham and G. Delerce. Advanced optimization of correlation imaging velocimetry algorithms. *Experiments in Fluids*, 29(1):S013–S022, 2000.

Chapter 4

The effect of confinement on the electrohydrodynamic behavior of droplets in a microfluidic oil-in-oil emulsion

Synopsis: Reprinted (adapted) with permission from Soft Matter (Royal Society of Chemistry Publishing Group)12(45), pp 9246-9255, 2016. S. Khajehpour Tadavani carried out the experiments and analysis and wrote the initial draft of the manuscript and implemented subsequent revisions. J. R. Munroe provided advice with the PIV analysis and provided comments on the drafts. A. Yethiraj supervised the project, provided comments on the drafts and contributed to the final text of the manuscript.

4.1 Abstract

A two-fluid emulsion (silicone oil drops in the "leaky dielectric", castor oil) with electrohydrodynamically driven flows can serve as a model system for tunable studies of hydrodynamic interactions [1]. Flows on multiple length- and time-scales have been observed but the underlying mechanism for these chaotic, multi-scale flows is not understood. In this work, we conducted experiments varying the thickness of the test cell to examine the role of substrate interactions on size distribution, mean square displacement, and velocity of the drops as a function of the electric field strength. We find that the electric capillary number, Ca_E, at the threshold of drop breakup is of order unity for cell thicknesses of 100 μm or thicker, but much larger for thinner cells. Above this threshold, there is a clear transition to super-diffusive droplet motions. In addition, we observe that there is a convective instability prior to the onset of chaotic flows, with the lengthscale associated with the convection rolls increasing linearly with an increase in the cell thickness. The fact that the convective instability appears to occur in the leaky dielectric castor oil regardless of whether the second component is liquid drops, solid particles, or dissolved dye has implications on the underlying mechanism for the unsteady flows.

4.2 Introduction

Several experimental model systems have realized tunable near-equilibrium self-assemblies [2–4], but there are fewer good model systems for far-from-equilibrium self-assemblies [5]. Electrohydrodynamics – fluid motion induced by electric fields– [6] provides a tuning parameter to drive an otherwise dissipative, low-Reynolds number fluid out of equilibrium. Liquid drops exposed to an external electric field and surrounded by another liquid respond in a variety of ways. They can deform, rotate, coalesce, or

break up [7]. The coupling between fluid motion and the electric field is used for a wide range of applications; two examples are electrohydrodynamic pumps [8] and ink-jet printing [9].

Drop deformation has been extensively studied theoretically and experimentally during the past six decades [10–16]. The theoretical description of immiscible drop behavior in a second liquid and in an electric field typically invokes the "leaky dielectric model" [13]. The model relates the accumulation of free charges at the liquid-liquid interface to a tangential component of the electric stress (which gives rise to electrohydrodynamic forces), which in turn competes with the normal electrostatic stress (*i.e.* dipolar forces) at the interface. Depending on the angular variation of stresses, or the strength of the applied electric field, the drop gives rise to shape deformation, or breakup [13–15].

This study focuses on the collective behavior within a test cell of many silicone oil drops in a medium of castor oil, interacting via long-range electrohydrodynamic forces. The strength of the hydrodynamic interactions are modulated by changing the amplitude of a DC electric field. In this system, violent breakup of silicone oil drops has been observed [1] above a threshold value of the electric field, followed by multi-scale flows that exhibit scale invariance in the intensity and stress fluctuations [17]. The flows in this "strong hydrodynamic" regime - *i.e.* hydrodynamic forces dominating over dipolar forces - are reminiscent of turbulent behavior. Turbulence in fluid mechanics is often associated with high Reynolds number R_e, but in this system $R_e < 10^{-5}$. Low Reynolds number turbulence, at R_e ranging from $10^{-5} - 10^{-1}$, has indeed been observed and studied in visco-elastic polymer solutions [18], and in electrokinetically forced pressure-driven flow in microchannels [19]. In the present experimental system, however, the underlying mechanisms for the multi-scale flow remains unclear. While the leaky dielectric model provides useful insights, it is likely

to break down where the Debye screening length, κ^{-1}, is of order the droplet size, a; this is the case in the current study. Studies that account for electrokinetic transport near the droplet interface [20, 21] have thus far either considered $\kappa^{-1} \ll a$ (and large external fields), or the limit of small deformations for a range of κ^{-1}.

A key question relates to what role the dimensionality of the sample, or confinement by the bounding substrates, plays. This question is relevant because the sample cell (see FIG. 4.1 and description in the Methods and Techniques section) is much thinner in the vertical dimension (a few hundred micrometers) than in its lateral extent (centimeters). The bounding plates in the vertical dimension are conducting substrates, which are also the electrodes. It is thus unclear if this microfluidic system is effectively two-dimensional or three-dimensional. To address this question, we vary the cell thickness, d, in order to examine the substrate-droplet interactions and the differences between quasi-two dimensional systems and three dimensional ones. As a function of cell thickness, and at different electric fields, we examine droplet size distributions, mean-squared displacement of the drops versus time, and droplet velocities.

4.3 Methods and techniques

FIG. 4.1 shows a schematic design of a test cell with the electric field perpendicular to the microscope slide and parallel to gravity. Two indium tin oxide (ITO) coated cover glass slides are separated by glass or plastic spacers with defined thicknesses. The plates and spacers are held together with ultraviolet-curable epoxy (Norland Optical Adhesive 61 and 68). The ITO slides are optically transparent and electrically conductive, which enables their use both as electrodes and to image through them as with regular glass. The cell is filled by pipetting an emulsion of silicone oil (dielectric

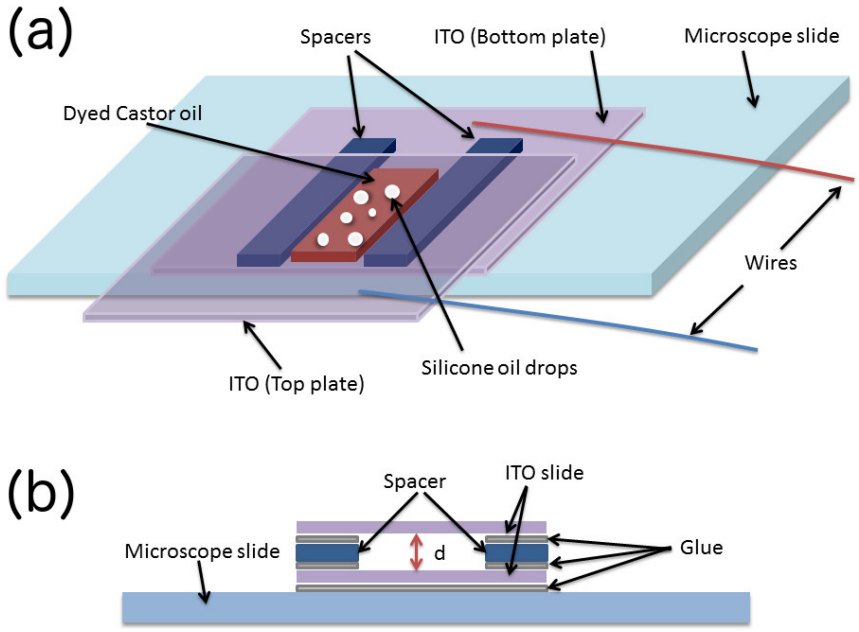

Figure 4.1: **A schematic design of the microfluidic cell geometry**: (a): perspective and (b): side view. Electric field is perpendicular to the substrate and parallel to gravity.

constant $\varepsilon_{in}/\varepsilon_0 = 2.4$, conductivity $\sigma_{in} = 3.95 \times 10^{-11}$ S/m, and viscosity $\mu_{in} = 0.137$ Pa $\cdot$ s) and castor oil (dielectric constant $\varepsilon_{ex}/\varepsilon_0 = 3.6$, conductivity $\sigma_{ex} = 4.0 \times 10^{-10}$ S/m, and viscosity $\mu_{ex} = 0.819$ Pa $\cdot$ s). The subscripts in and ex are used to represent the droplet and the suspending fluid, respectively. The emulsion was prepared first by mixing silicone oil and castor oil in a volume ratio of 1:16. Then, it was vortexed by a vortex mixer for 5 minutes. This leads to a uniform dispersion of tiny silicone oil drops, with different sizes, in the castor oil. The cell was immediately filled after preparing the emulsion.

The lateral dimension of cells is between 0.5 and 1 cm, while the vertical dimension, or the cell thickness, d, varies as 27, 55, 96, or 202 μm. The strength of the DC electric field is varied from 0 up to 18 V/μm in intervals of 1V/μm.

The conductivity and the dielectric constant of oils were measured by impedance

spectroscopy using an impedance analyzer, a potentiostat/galvanostat (Princeton Applied Research model 273A) attached to a lock-in amplifier (Signal Recovery model 5210), in the 0.1 Hz to 100 kHz frequency range. The frequency dependence, $|Z| = R/\left(1+(fRC)^2\right)^{1/2}$, was fitted and R and C were obtained. The conductivity, $\sigma = d/RA$, and the dielectric constant, $\varepsilon = \varepsilon_0 A/Cd$, where d, A, ε_0 are the gap distance between the two parallel plates, cell area, and permittivity of vacuum, respectively, were then calculated from R and C.

After recording an experiment with a water-cooled digital sCMOS camera (pco.edge 5.5), the shapes and positions of the droplets are found. An edge finding algorithm, written in the image processing software, Fiji (`http://fiji.sc/Fiji`), is used to find the edge of the drops based on the gradient of image intensity as the edge finding method. For every frame in a video sequence, or stack, the centroid, (x, y), and area of every drop is measured. After identifying the coordinates of the droplets one is able to track their motion using particle tracking. This is done using code described by Crocker and Grier [22].

From this, we obtain the mean square displacement, $MSD \equiv \langle r^2 \rangle$, where r is the magnitude of the displacement of each drop as a function of the time t (from a reference start time t_0), and $\langle \cdot \rangle$ is an average over all the drops in the system, and over the reference time. One can write MSD $\sim t^\gamma$, where $\gamma = 1$ for diffusive motion, and is larger for advection and smaller for constrained diffusion.

For particle imaging velocimetry (PIV) an open source implementation, *CivX*, is used [23, 24]. Interrogation windows with a size that is roughly twice the drop diameter are used and the displacement is estimated from cross-correlation of consecutive frames. Here, we are using PIV as a form of interfacial velocimetry (the analog of the "tracer particles" are the points on the drop interface).

We also carry out experiments with fluorescent PMMA colloids (diameter of 1 μm)

suspended in castor oil and in a volume ratio of 1:80. The PMMA particles are charged, and when the sign of the electric field is switched, particles migrate from the positive to the negative electrode with a speed proportional to the electric field (7 μm/s for E = 1 V/μm, yielding an electrophoretic mobility $M \sim 7\ \mu\text{m}^2/\text{V}\cdot\text{s}$). We also carried out experiments on the diffusion of the dye (Nile red) in castor oil, using white light illumination and time-lapse macro scale photography. These results are presented in section 4.4.5.

4.4 Results and discussion

4.4.1 Breakup and coalescence of drops

The droplet breakup mechanism is studied as a function of the cell thickness, d, and amplitude of the DC electric field, E. We begin with the thinnest cell ($d = 27\ \mu$m). Upon increasing the electric field, one observes, at a threshold field of 8.5 V/μm that large drops, with lateral (cross-section) radius roughly between 80 and 180 μm (*i.e.* much wider than the cell thickness), break up into smaller ones. FIG. 4.2(a) shows the breakup of one such large drop at $E = 9.5$ V/μm. The bottom of the drop is in complete contact with the substrate while most of the top is in contact with the top electrode, except for a meniscus which is roughly 50 μm wide. As the magnitude of the electric field increases, the edges of the drops fluctuate and create a natural wavelength ($\simeq 40 \pm 9\mu$m), and droplets are generated with diameter that are all comparable or slightly larger than the natural wavelength and roughly twice the cell thickness of $d = 27\ \mu$m. The white rectangles highlight the three breakup events that occur in the region of interest over several seconds. This may be seen in Supplementary information, Section 4.7.1, Movie 4.1 (left panel).

For a cell that is roughly twice as thick ($d = 55\ \mu$m), shown in FIG. 4.2(b),

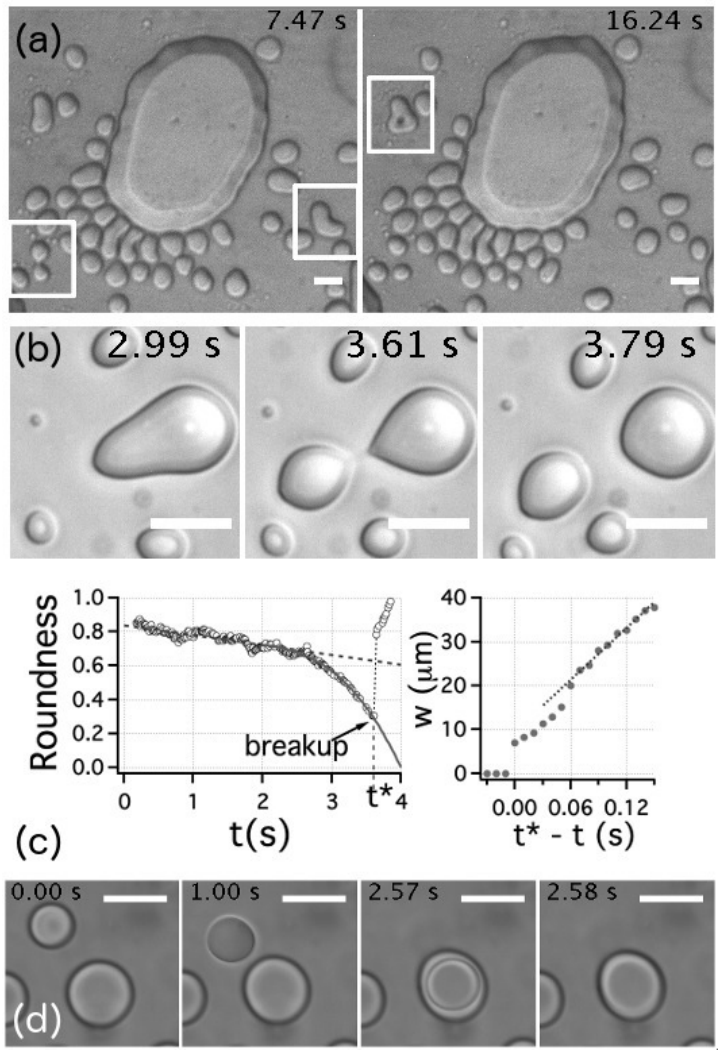

Figure 4.2: **Drop breakup and coalescence in a DC electric field.** (a): $d = 27$ μm. The edge of a big drop fluctuates with a wavelength of roughly 40 μm and drops of comparable diameter are generated from these fluctuations. The white boxes highlight regions where drop breakup is occurring. $E = 9.5$ V/μm. (b): $d = 55$ μm. Droplet breakup phenomenon for oblate spheroidal deformations occurs with drop being pulled apart laterally, perpendicular to the electric forcing. (c): The breakup is slow with a linear decrease in roundness for 2 seconds, prior to a more rapid decrease until breakup occurs (at $t = t^* = 3.61$ s); the latter is accompanied by a decrease in the width w of the neck: just prior to breakup the neck is 7 μm wide. (b, c) $E = 8.5$ V/μm. (d): $d = 96$ μm. Coalescence of two deformed (oblate spheroidal) droplets. Drop coalescence is achieved by the self-alignment and attraction along the DC electric field; the cell is now thick enough to accommodate two drops atop each other. $E = 3.5$ V/μm. In all figures, the electric field is perpendicular to the page, and the scale bar is 50 μm.

drop deformation is observed first for the largest drops (with initial cross-section radius roughly between 20 and 115 μm) at $E = 4.5$ V/μm. At 6.5 V/μm, the edge deformations gives rise to droplet breakup and smaller droplets are generated from the bigger ones. At this threshold field, the interfacial tension is overcome by the electric stress at the interface.

The breakup of one such drop, at $E = 8.5$ V/μm, shown in FIG. 4.2(b) obtained at 100 frames per second for the complete time evolution), can be tracked as a function of time by any measure of the curvature: we use the "roundness", defined as $4 \times Area/\left(\pi D^2_{\mathrm{major-axis}}\right)$. FIG. 4.2(c, left) shows that the roundness as a function of time decreases linearly for more than 2 seconds before there is a sharper decrease (fitted to a power law) that coincides with the formation of a thin "neck" that eventually breaks. FIG. 4.2(c, right) shows the width of this neck, w, which decreases rapidly over the fractions of a second prior to breakup, from 40 μm to about 7 μm. This dynamics may be seen in Supplementary information, Section 4.7.1, Movie 4.1 (middle panel). What we are observing is crossover between two regimes of thinning: this has previously been observed in the thinning dynamics of liquid drops before breakup [25].

A third cell, again roughly twice as thick as the previous one, was made with a thickness of $d = 96$ μm. The initial cross section radius of drops varied from 9 to 282 μm. The breakup phenomenon in this case began at 3.5 V/μm. A notable qualitative difference at this thickness is the much higher frequency of coalescence events. While for the thinnest cell ($d = 27$ μm) no coalescence of drops was observed even at high fields (18.5 V/μm), coalescence was readily observed here. An example is seen in FIG. 4.2(d): at t = 0 s, a drop detaches from the substrate, and approaches a second drop, riding on top of it so their flattest faces are in contact. This may also be seen in Supplementary information, Section 4.7.1, Movie 4.1 (right panel). This is clearly easier to achieve in a thicker cell, and thus coalescence is seen at the modest

fields that drive drops into motion.

For the last and thickest cell, $d = 202$ μm, the initial cross sectional radii are between 17 and 244 μm. The coalescence and breakup of drops start at low field, somewhere between $E = 1.5$ V/μm and $E = 2.5$ V/μm and the cell is thick enough to let drops move freely vertically. Although three-dimensional motion also happens in the third cell, it is more dominant and frequent in this thicker fourth cell.

Given the importance of the bounding surfaces, it is of interest to know if the contact angle changes with electric field. The contact angle of a silicone oil drop on glass, and in a castor oil environment, is measured (using a field geometry where the viewing direction is perpendicular to the field) to be $125 \pm 1°$. There is only a $2°$ difference between zero and high fields; therefore, given the uncertainties, we may say that there was no discernible change in contact angle with field strength.

Steady equilibrium deformation of a drop no longer exists if the electric field strength exceeds a critical value. The reported dynamics is either a tip-streaming deformation when $\varepsilon_{in}/\varepsilon_{ex} > 1$ [26–29], or a pinch-off deformation which produces a bulbous-ended deformation and breakup when $\varepsilon_{in}/\varepsilon_{ex} < 1$ [26, 28, 29]. FIG. 4.2(b) shows a pinch off breakup with the electric field perpendicular to the thin thread. A new kind of deformation, a hole in the middle of a bigger drop, prior to the breakup event was also seen at $d = 27\mu$m, FIG. 4.2(a).

4.4.2 Droplet size statistics in thin and thick cells

Next, we examine the drop size statistics, as a function of cell thickness for increasing electric fields. The cross-sectional area of the drops, A, is used to calculate the distribution of drop sizes. The size distributions for $d = 27$, 55, 96, and 202 μm, each for a range of electric fields, are shown in FIG. 4.3. One can obtain an effective cross section radius $R = \sqrt{A/\pi}$ representing the radius of a circle with the same area as the

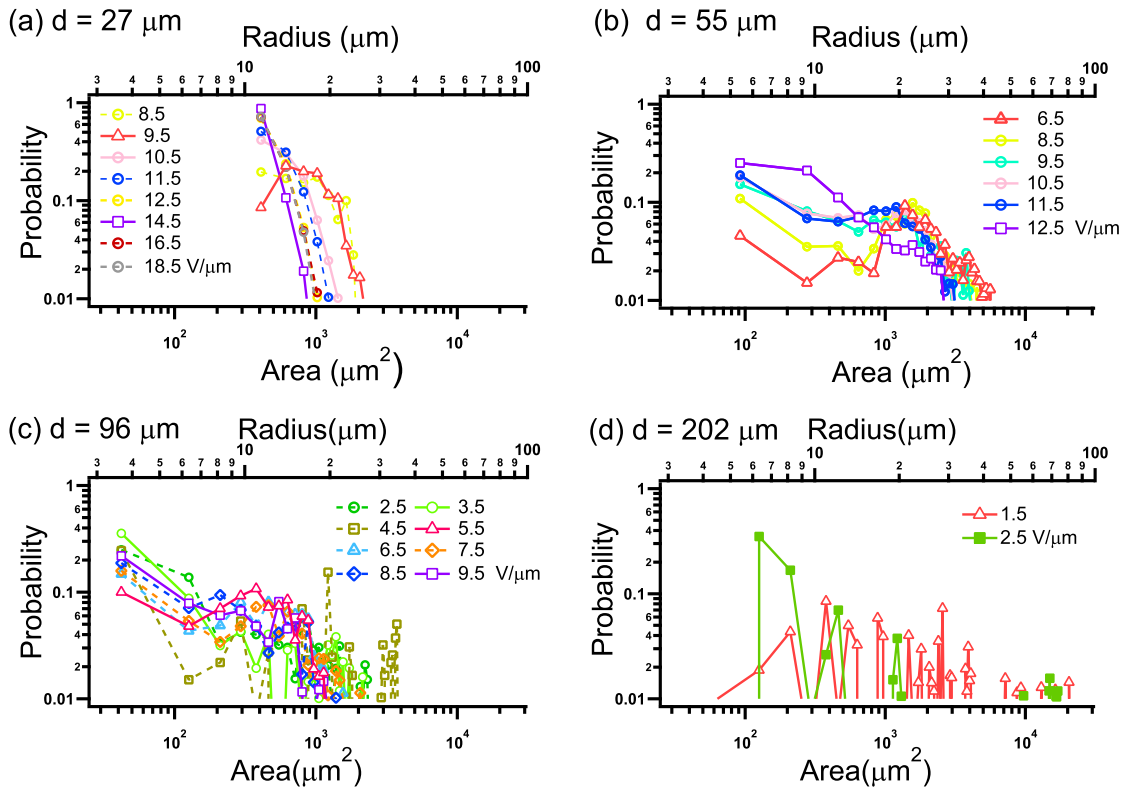

Figure 4.3: **Normalized drop size distribution obtained from 1000-image time series**. The top axes shows the corresponding radius for different areas. (a): $d = 27$ μm: intermediate-field peak in the distribution at $R_0 \simeq 10 - 20$ μm shifts to 10 μm at highest fields. (b): $d = 55$ μm: intermediate-field peak at $R_0 \simeq 20 - 25$ μm shifts to lower R for higher fields. In both cases $2R_0/d \sim 1$. (c): and (d): $d = 96$ μm and $d = 202$ μm: There is no peak at $2R/d = 1$, but merely a continuous shift of the size distribution to smaller R. Coalescence events are more common; this could be the cause of a small peak (in the $d = 96$ μm cell) at $R \simeq 10 - 20$ μm.

roughly, but not completely, circular drops: this radius is depicted on the top axes of each graph. It should be noted that the initial average lateral size of the drops in all cases is much larger than the cell thickness: the initial drops are shaped like hockey pucks. Once the field exceeds a threshold, and the lateral extent of the drop is smaller than the thickness, the drops are closer to spherical.

The size distributions are obtained from image sequences of typically 1000 frames, obtained at different DC electric fields. At zero fields for all cell thicknesses there are

only a few drops, with discrete peaks at high areas (corresponding to radii of 100 μm or greater) in each of the size distributions. These initial conditions (not shown in FIG. 4.3) are determined when the sample cell is filled. For non-zero fields, the image sequences are acquired once the system has reached a steady state. In order to obtain the lateral size of the droplet, the images must allow us to find the edge; this is, for example, not possible for fast-moving or fast-deforming drops. It is noteworthy to mention that the size distribution is obtainable up to higher fields for thinner cells: up to 12.5, 9.5, and 2.5 V/μm for cell thicknesses of $d = 55$, 96, and 202 μm respectively. For the thinnest ($d = 27$ μm) cell, the size distribution is measurable up to highest field probed, *i.e.* 18.5 V/μm.

First, we examine the thinnest two cells. FIG. 4.3(a) shows the drop size distribution for the first cell ($d = 27$ μm). For fields at and above 8.5 V/μm (which is shown with red triangles), a shallow peak emerges at around $R_0 \sim 15$ μm: this corresponds to a diameter $2R$ that is roughly equal to the cell thickness d. For higher fields the peak shifts towards lower R and increases in magnitude. For the second cell ($d = 55$ μm, FIG. 4.3(b)), a peak at $R_0 \approx 20 - 25$ μm emerges for $E \geq 6.5$ V/μm (shown with red triangles). This is, once again, consistent with $2R \sim d$. The magnitude of this peak, again, decreases for increasing fields with another peak emerging at lower radius. For both the first and second cells, the peak in the size distribution function corresponding to a drop size that is comparable to the cell thickness likely arises from a stabilization of the drops by pinning at the top and bottom substrates. Eventually, however, at high enough fields, drops break up further and generate drops much smaller than the thickness of the cell. The smallest cross-sectional radius observed for these two sample thicknesses is around 10 μm.

Next, we examine the thicker cells. For the third cell, $d = 96$ μm (FIG. 4.3(c)), there is no clear peak at intermediate radii, but simply a continuous shift of the

distribution towards lower radii as the field is increased, with a mean drop radius $\overline{R}$ (shown in FIG. 4.4(a)) that is roughly between 10 and 20 μm for all fields. Here, $2\overline{R} \ll d$. The fourth cell, $d = 202$ μm (FIG. 4.3 (d)), is clearly in the bulk regime – the mean drop sizes (shown in FIG. 4.4(a)) are again much smaller than the cell thickness – and the static drop size distribution measurements are only possible for the lowest fields. Drop sizes are already strongly peaked at $R \sim 6$ μm for a (relatively) low field of $E = 2.5$ V/μm. The statistics are poorer for the thickest cells, because the out-of-plane motion of the drops is increasingly important, and this makes it hard to get static droplet sizes from a single-plane image at fields. Notably, for both these cell thicknesses, there is no peak at intermediate fields at $2R = d$. As well, for all samples at high field, the drop size distribution develops a peak for $R \leq 10$ μm.

The mean drop radius, $\overline{R}$, versus electric field and for all thicknesses is shown in FIG. 4.4(a). Above the threshold, in the ranges $8.5 - 18.5$ V/μm, $8.5 - 12.5$ V/μm, $2.5 - 9.5$ V/μm, and $1.5 - 2.5$ V/μm for $d = 27$, 55, 96, and 202 μm, respectively, the radius decreases with increasing field. For all measurements made at high fields, $\overline{R}$ approaches a value of between 10 and 20 μm.

We can now use the above information to get some insight into when the role of substrate becomes important. The importance of the electric stress relative to interfacial tension is measured by the electric capillary number, which for small drop deformations may be written as [30]

$$Ca_E \equiv \frac{9 \mid S^{-1}H - 1 \mid M^{-1}}{10\left(H+2\right)^2\left(M^{-1}+1\right)} \frac{\varepsilon_0 k_{in} a E^2}{\gamma}. \tag{4.1}$$

In this system $S = \varepsilon_{in}/\varepsilon_{ex} = 0.67$, $H = \sigma_{in}/\sigma_{ex} = 0.10$, $M = \mu_{in}/\mu_{ex} = 0.17$, $\gamma \simeq 3 - 4$ mN/m is the interfacial tension between the oils, $\varepsilon_0 = 8.85 \times 10^{-12}$ F/m is the vacuum permittivity, $k_{in} = 2.4$ is the dielectric constant of drop, a is radius of the

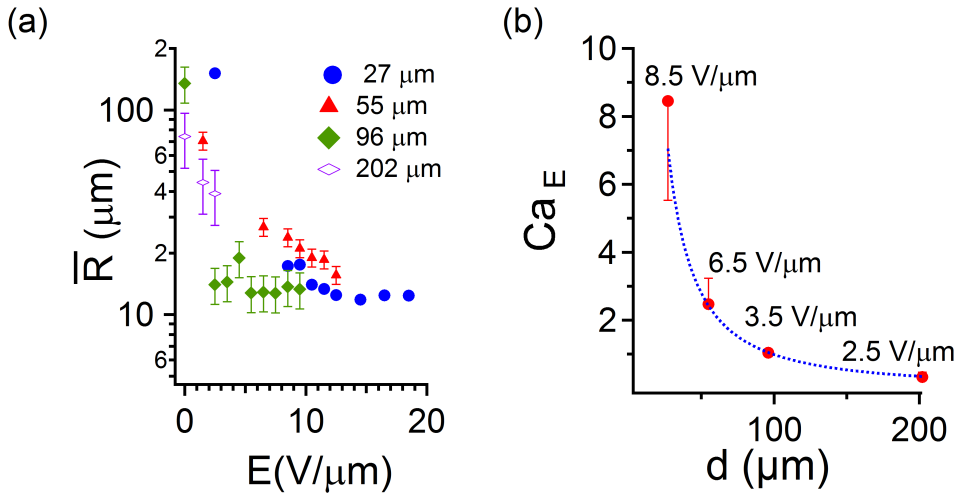

Figure 4.4: (a): Mean drop radius $\overline{R}$ as a function of electric field, for the samples of 4 cell thickness, d. (b): Capillary number versus cell thickness at the critical values of electric fields where drop breakup is observed. The electric capillary number Ca_E decreases as the cell thickness increases.

drop and E is the strength of the applied electric field. The electric capillary number is often defined simply as $Ca_E = \varepsilon_0 k_{ex} a E^2/\gamma$. We follow instead Feng [30], where one uses $Ca_E = \mu_{ex} U/\gamma$ with U being the maximum velocity at the drop surface calculated from the solution for a spherical drop. As the capillary number approaches unity one would expect the smooth liquid-liquid interface to become destabilized, and develop waves. In this system the electric capillary number can be written as $Ca_E = 0.9 \times 10^{-9} a E^2$ (where a and E are expressed in mks units). FIG. 4.4(b) shows the electric capillary number, for initial size of drops depending on the cell thickness, 130, 65, 95, and 60 μm for $d = 27$, 55, 96, and 202 μm, respectively, and at the critical electric field. The error bar symbol here denotes the extreme value if an average initial drop size of 85 μm is used instead for all estimates. For cells of thickness above ~ 100 μm, breakup occurs at $Ca_E \sim 0.3 - 1$ but increases as d decreases (the dotted line in Figure 4(b) is a phenomenological fit to $1/d^{\alpha}$ with $\alpha = 1.5$). This is an indication that substrate interactions (which stabilize large droplets) are important

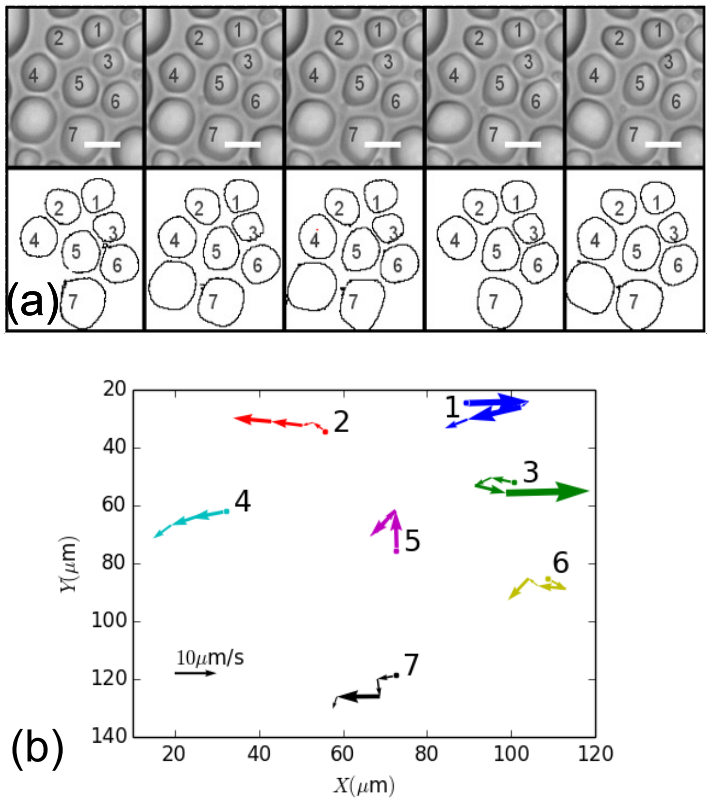

Figure 4.5: (a): $d = 55$ μm. The deformation of drops (upper panel) tracked by edge detection (lower panel) for short times $t < 0.8$ s (from left to right, Δt = 0, 0.2, 0.4, 0.6, and 0.8 s). Scale bar is 35 μm. $E = 12.5$ V/μm (out of page). (b): Velocity vectors indicating direction of displacement of each labelled drops over 0.8 s. A small displacement of the particles between the frames is observed, with no clear directed motion.

for the lowest two cell thicknesses.

4.4.3 Drop motions: 2D motions in thin cells

The motion of drops, for $t < 0.8$ s, is shown by a sequence of images for $d = 55$ μm. FIG. 4.5(a)(upper panel) shows 4 frames with time interval of 0.2 s. One can see that the seven drops labelled in these frames deform and change shape slightly (as can be seen clearly from the edge of the drops (lower panel) found by the edge finding

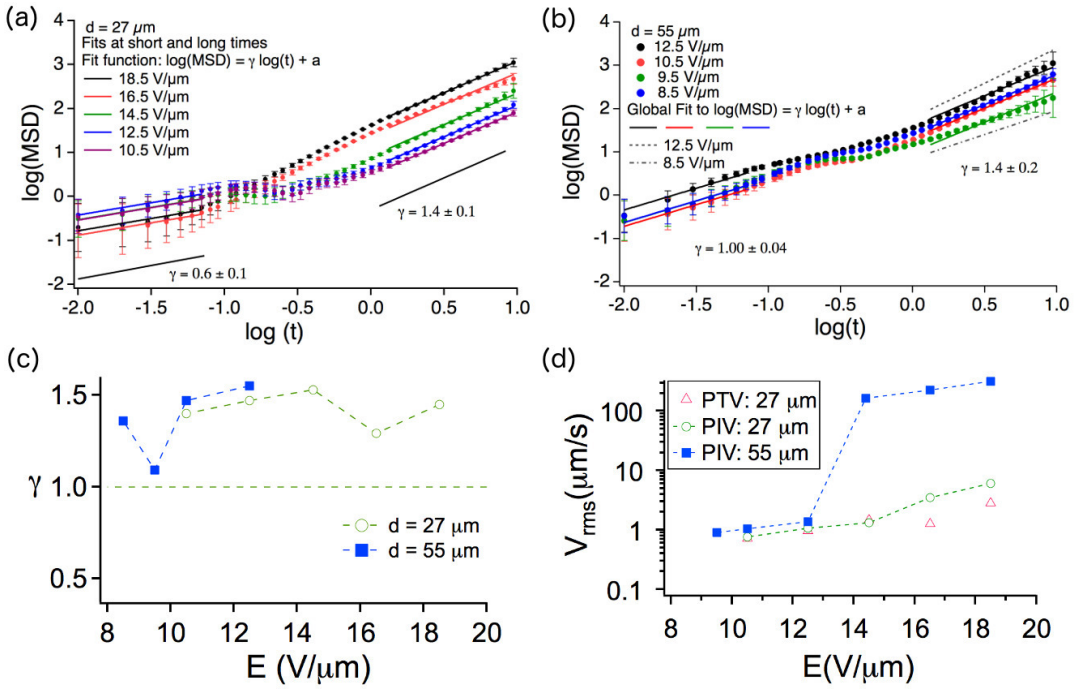

Figure 4.6: **Motions in thin cells.** Mean-squared displacement *vs* time obtained from particle tracking for (a): $d = 27$ μm and (b): $d = 55$ μm. If one writes MSD $\sim t^{\gamma}$, a plot of $\log(\text{MSD})$ *vs* $\log(t)$ shows a short-time regime ($\log(t) < -0.5$) where the dynamics appears either sub-diffusive or diffusive ($\gamma \leq 1$), and a long-time regime ($\log(t) > 0$) where the dynamics is clearly super-diffusive ($\gamma \sim 1.4$).(c): γ at long times and (d): V_{rms} using particle imaging velocimetry (PIV) as a function of electric field for the above two samples shows the remarkable, order-of-magnitude, increase in motions at high fields. For $d = 27$ μm, V_{rms} from PIV is compared with velocities obtained using particle tracking.

method. The velocity vectors, indicating the direction of displacement, are shown in FIG. 4.5(b).

The mean-squared displacements over the droplet centroids are shown in FIG. 4.6(a) and (b) for $d = 27$ and $d = 55$ μm, respectively. One may write MSD $\sim t^{\gamma}$, where $\gamma < 1$, $= 1$ and > 1 represent sub-diffusive, diffusive, and super-diffusive motion. For times $\log(t) < -0.5$, $\gamma \leq 1$ for both $d = 27$ μm and $d = 55$ μm cells. The errors in γ at short times are large; we therefore fit results for all fields to a single γ. For times $\log(t) > 0$, the dynamics is clearly super-diffusive, with $\gamma \sim 1.4$, FIG. 4.6(c).

Supplementary information, Section 4.7.2, Movie 4.2 displays the motion of drops over short times, $t = 1.0$ s, and long times, $t = 10$ s.

At higher electrohydrodynamic forcing, detecting droplet edges is challenging, but we can employ particle imaging velocimetry (PIV) to obtain the rms speeds, $V_{\rm rms}$. The results of the PIV method are compared, for $d = 27$ μm, with the velocity of the fluid flow measured by particle tracking. For particle tracking, the function $MSD = K_1\, t + K_2\, t^2$ is used to fit the data. This is shown in Supplementary information, Section 4.7.2, Figure 4.11. Based on this function, $\sqrt{K_2}$ is the effective velocity magnitude of the fluid. Also, comparisons of the velocities, via PIV and particle tracking, are only possible when tracking is viable. For thin cells, $d = 27$ and 55 μm, the velocity can be measured by tracking, but this method cannot be applied for the thicker cells, where PIV is the only feasible method.

FIG. 4.6(d) shows the measured velocities. A comparison between tracking and PIV for $d = 27$ μm shows that the results from two methods are consistent in the low-field regime, where the flows are slow enough that droplet centroids move only a few pixels between successive time frames of image capture. The results are dramatic. While the maximum velocity observed for $d = 27$ μm is 7 μm/s, it is 300 μm/s for $d = 55$ μm, and there is a sharp threshold above $E = 12.5$ V/μm, where the transition to strong electrohydrodynamic flow occurs. There is a clear link between the reduction of droplet sizes and the onset of super-diffusive motion. For example, in FIG. 4.4(a), for $d = 55\mu$m, $2\overline{R}$ decreases to a value below the cell thickness d for $E = 6.5$ V/μm and greater. FIG. 4.6 shows that the motions for all fields ($E = 8.5$ V/μm and above) is super-diffusive.

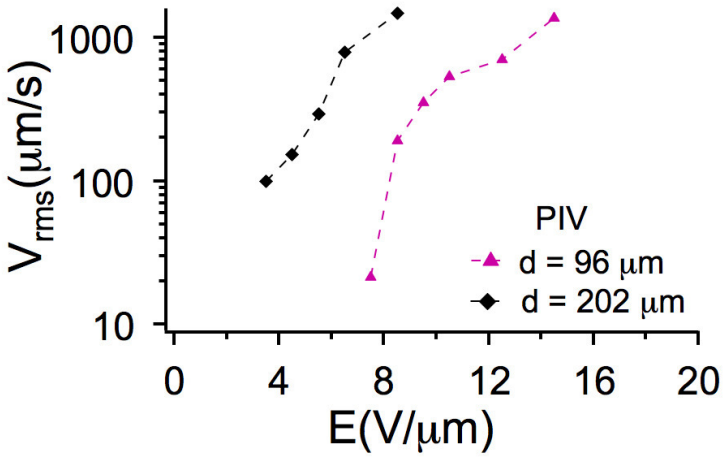

Figure 4.7: **Motions in thick cells.** PIV analysis shows a sharp increase, by more than two orders of magnitude in $V_{\rm rms}$ from $10\mu{\rm m}/s$ to $1500\mu{\rm m}/s$ with increasing electric field. The threshold field for an increase above 300 $\mu{\rm m}/s$ is much smaller ($E = 5.5$ V/μm) for the cell thickness $d = 202$ μm than for $d = 96$ μm ($E = 8.5$ V/μm).

4.4.4 From 2D to quasi-3D motions

For thin cells, we saw three behaviors: first, a low-field regime where the mean-square droplet displacements are sub-diffusive or diffusive; second, an intermediate-field regime where the MSD is super-diffusive but still two-dimensional, and finally a high-field regime, where tracking is not possible, but PIV results show very large droplet velocities up to 300 μm/s.

For the samples with cell thickness $d = 96$ and 202 μm, we find that above a relatively low field threshold, the droplets exhibit visible out-of-plane motions. With increasing thickness, the maximum rms velocity observed is 7 μm/s, 300 μm/s, 1.4 mm/s, and 1.6 mm/s, respectively. Here the PIV analysis, based on only the X-Y components of displacements, are only indicative, and provided a lower bound on estimates of rms velocity, which is related to the droplet kinetic energy: $V_{\rm rms} \propto \sqrt{E_{\rm kin}}$. We find (FIG. 4.7) that there is a two orders-of-magnitude increase in the $V_{\rm rms}$, cor-

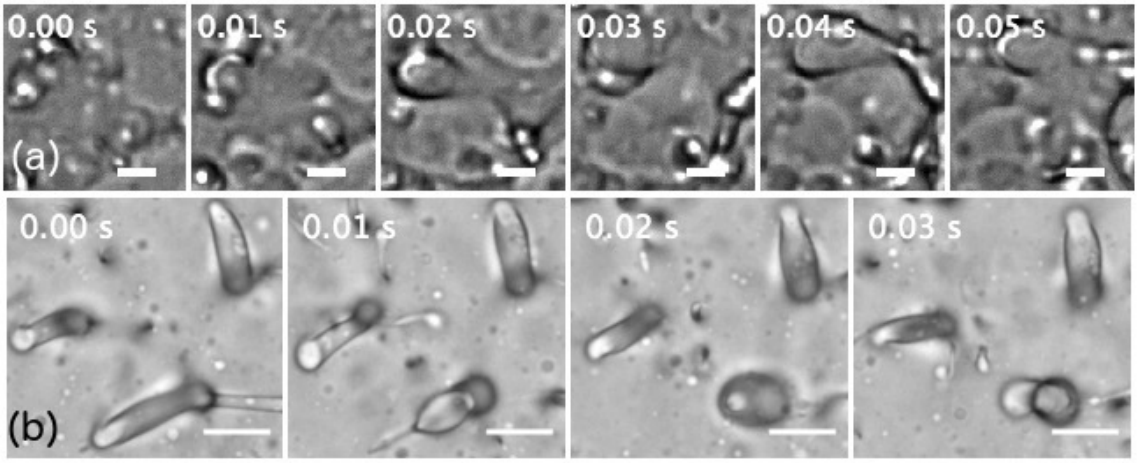

Figure 4.8: (a): $d = 55$ μm, $E = 18.5$ V/μm, perpendicular to the page. Time series shows 6 frames in 0.01 s intervals, displaying violent breakup, and coalescence of drops. Scale bar: 10 μm. (b): $d = 202$ μm, $E = 8.5$ V/μm, perpendicular to the page. Dynamics in the strong hydrodynamic regime results in "inversion": local dynamical regions with cylindrical drops of castor oil inside a silicone oil background, which in turn is surrounded by castor oil. Scale bar: 50 μm.

responding to an order-of-magnitude increase in E_{kin}.

4.4.5 Onset of the regime of strong hydrodynamics

The regime of strong hydrodynamics is one where hydrodynamic forces dominate over dipolar forces. Much of the previous analyses focus on the onset of droplet motions and do not address the out-of-plane motions seen in the movies for the thicker cells, which resemble the vertical overturning observed in Rayleigh-Bénard convection [31]. Second, at high fields, very vigorous droplet motion that resembles a boiling liquid is observed. This is shown in FIG. 4.8(a) and (b) for $d = 55$ μm (and $E = 18.5$ V/μm) and for $d = 202$ μm ($E = 8.5$ V/μm), respectively.

To examine this phenomenon in a simpler system, we put fluorescent PMMA tracer particles in castor oil (with no silicone oil) to track the flows. This is challenging, because castor oil has a large Debye length, ($\kappa^{-1} \sim 1\mu$m), and the tracer particles

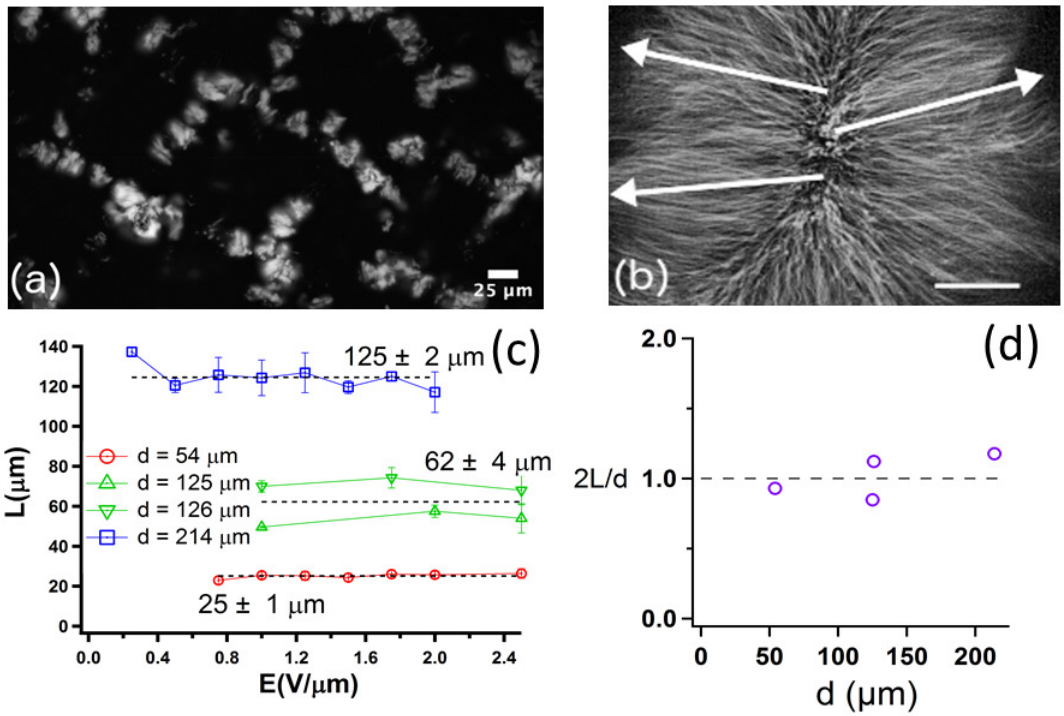

Figure 4.9: **Convective Instability in fluorescent PMMA colloids in castor oil**. (a): Snapshot of several convection cells in a cell of thickness $d = 54$ μm. Scale bar: 25 μm. (b): Convection rolls are observed for cells of different cell thickness d; shown is a timelapse series (for the $d = 125$ μm cell) that captures the flow of particles from a "source" in the centre (tail of the arrows) to a "sink" at the edge of the cell (head of the arrows). Scale bar: 25 μm. (c): The characteristic length associated with the roll L scales with d. (d): The ratio $2L/d \sim 1$, which is consistent with a two-roll structure; see text.

acquire a charge in a partially polar medium [32]. Nevertheless, we can examine the phenomena at the threshold of particle motions. Shown in FIG. 4.9(a) is a snapshot of several convection cells for a cell with thickness of 54 μm. Upon increasing the strength of the electric field from 0 to 2.4 V/μm circulation patterns are observed inside the cell (see Supplementary information, Section 4.7.4, Movie 4.3). An example of circulation patterns is shown in the time-lapse projection in FIG. 4.9 (b). The arrows show the direction of circulations. The lengthscale of these circulations can be characterized by the lateral distance L between upward and downward flows (sources and sinks

in a 2-dimensional time series). This lengthscale scales with the cell thickness d, with $2L/d \sim 1$ (see FIG. 4.9 (c)). Typical "one-roll" structures in Rayleigh-Bénard convection (between rigid boundaries) are defined by a wavelength $\lambda_c = 2L \sim 2d$ [31]. What we observe appear to be two-roll structures, which have been reported in numerical studies of electrohydrodynamics [33, 34]. Thus, while the mechanism for the unsteady (and seemingly turbulent) motions is as yet unknown, the above observations suggest that the onset of unsteady motions is related to an electrical analog of Rayleigh-Bénard convection.

In the leaky dielectric picture, toroidal flows are the results of a liquid-liquid interface. The question arises, therefore, whether the flows observed for solid particles in castor oil are due to the presence of the particles (*i.e.* a kind of electro-osmotic flow). In a final experiment, the dye, Nile red, was mixed with castor oil. A cell was filled as follows: one end containing the dyed castor oil and the other end containing the non-dyed castor oil, as shown in the panels of FIG. 4.10(a) and (b) which are obtained from a sequence of millimeter-scale photographs. In the first 3 hours, FIG. 4.10(a), the electric field was off and the two regions are separable with a distinguishable boundary for all times. With the field on, $E = 8$ V/μm (pointing into the page), and in 16 minutes, FIG. 4.10(b), there is a blurring of the boundaries between the dyed and non-dyed regions (Supplementary information, Section 4.7.5, Movie 4.4). FIG. 4.10(c) shows $(h - h_0)^2/2$, half the mean squared displacement of the interface between dyed and non-dyed regions vs time; while h and h_0 are the position of the interface at time t and 0, respectively. An effective diffusion of coefficient can be calculated from $2D_{eff}^{E\neq 0}t = (h - h_0)^2$ which is $D_{eff}^{E\neq 0} = (0.31 \pm 0.01) \times 10^{-2}$ mm^2/s. We could also measure the effective diffusion of dye molecules in the absence of the field, $D_{eff}^{E=0} \approx 0.56 \times 10^{-6}$ mm^2/s, and compare it with the effective diffusion of mixing. There is clearly enhanced dynamics, $D_{eff}^{E\neq 0}/D_{eff}^{E=0} \approx 5500$, in the presence of the

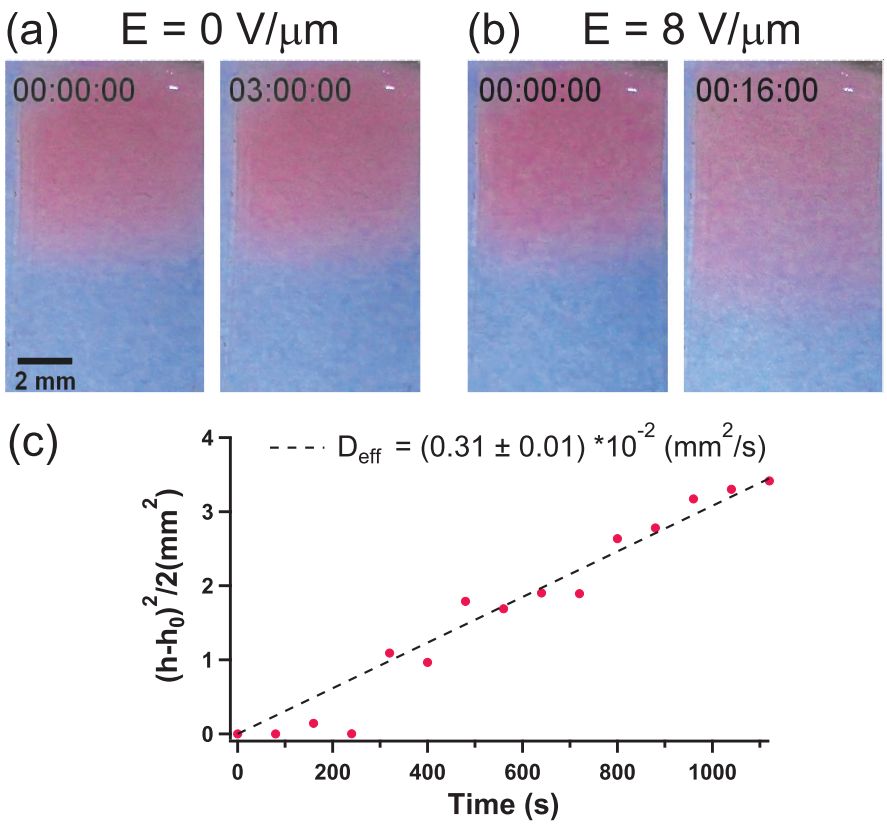

Figure 4.10: **Mixing of dyed and non-dyed castor oil in the presence of electric field**: (a): $E = 0\text{V}/\mu\text{m}$ at $t = 0$ and $t = 3$ hours, no mixing of two regions was observed in the absence of field. (b): $E = 8$ V/μm (pointing into the page) at $t = 0$ and $t = 16$ minutes, enhanced mixing was observed in the presence of the field. (c): Half the mean squared displacement of the interface between dyed and non-dyed regions vs time. The slope gives the effective diffusion coefficient of mixing at $E = 8$ V/μm.

electric field. Since this enhanced motion occurs in the absence of either a second liquid or of solid tracer particles, neither the classic leaky-dielectric model for liquid-liquid interfaces nor electro-osmotic flows at the particle-fluid interface are relevant here. A possible mechanism is suggested by the work of Posner and Santiago [35], which showed that electrokinetic flows can become unstable when conductivity gradients exist. While the ion concentration in the bulk of our samples is uniform, there are likely ionic gradients near the electrodes which give rise to the convective instability.

4.5 Conclusion

The collective behavior of electrohydrodynamically driven dielectric oil droplets in a leaky dielectric medium is studied in this work as a function of the cell thickness. The effect of sample thickness on droplet size distribution is studied first, followed by an examination of droplet dynamics, using two complementary methods: direct tracking of droplet centroids (particle tracking) as well as imaging velocimetry of the droplet interfaces (PIV).

The initial condition involves drops that have a lateral extent that is much larger than their thickness. The interactions of the drops with the substrate is therefore very important. For drop size and fields corresponding to $Ca_E \sim O(0.1)$, or smaller, droplets are not broken up further: this results in a peak in drop size distribution of $R \sim 10$ μm. For thin cells, $d = 27$ and 50 μm, drop dynamics is practically two dimensional, and few coalescence events are observed.

The question of what is thick or thin can be addressed in two ways. First, the threshold field for drop breakup decreases with increasing the cell thickness, and for these fields the $Ca_E \gg 1$. Second, the threshold field, where particle tracking is feasible also decreases. A practical conclusion is that cells of thickness equal or larger than 100 μm, while still much smaller than the lateral extent of a few centimeters, are thick enough for bulk behavior to emerge.

For the thinnest cells, $d = 27$ and $d = 55$ μm, a transition from 2D random-walk-like motion with $\gamma \leq 1$ (likely driven by the stick-slip of the fluid-fluid-substrate contact line) to advective motion (characterized by MSD $\sim t^{\gamma}$ with $\gamma \sim 1.4$) is observed as a function of field. Droplet speeds of order 1 μm/s are seen for $d = 27$ μm, while speeds of order 100 μm/s are observed for $d = 27$ to $d = 55$ μm; at higher fields and higher cell thicknesses, one sees even more vigorous droplet motions $V_{rms} \sim 1000$ μm/s. For drop sizes $a > 10$ μm (and given $\kappa^{-1} \sim 1$ μm), $\kappa a > 10$,

the leaky dielectric model (valid for $\kappa a \gg 1$) [15] is likely a reasonable description of the phenomena. However, in the strong hydrodynamic regime, where drop sizes $a < 10$ μm, κa is of order unity, and modeling the phenomena will also be more complicated.

For the thicker cells we additionally observe vertical overturning at remarkably low fields. The system is clearly more 3-dimensional and the pinning of the drops at the substrate is much less strong. Once again, at high fields, we see a transition to vigorous, unsteady flows. Analysis of these motions is more difficult because of the need to image the system in 3 dimensions; this will be the focus of future work. The overturning in thicker cells, prior to the onset of strong hydrodynamics, is reminiscent of Rayleigh-Bénard convection, and is also observed for PMMA colloidal particles in castor oil, where the convection rolls have a lateral scale that is proportional to the cell thickness. Counter to the expectation from the leaky dielectric model, we find that enhanced dynamics exists even in the absence of liquid-liquid interfaces, and also in the absence of solid-liquid interfaces. It is feasible that the origin of the convective flows is due to the presence of ionic gradients near the confining electrodes.

Recent efforts towards a more quantitative electrokinetic description [15, 21] of the electrohydrodynamic problem could provide a starting point for comparison with the phenomena described here. This work provides clear observations to look for, as a function of cell thickness: the drop size distribution versus electric field (FIG. 4.3), the magnitude of the drop breakup threshold (FIG. 4.4), and the transition from slow motions to super-diffusive motions (FIG. 4.5 - 4.8). In addition, both the vertical overturning seen in emulsions as well as particle-laden fluid (FIG. 4.9 and Supplementary information, Section 4.7.4, Movie 4.3) and the mixing of the carrier fluid in the presence of electric fields (FIG. 4.10 and Supplementary information, Section 4.7.5, Movie 4.4) suggest the importance of a proper electrokinetic description.

4.6 Acknowledgments

Zena Aljabal is thanked for carrying out the impedance measurements. We thank Len Zedel for suggestions that led to this study, and Atul Varshney for useful discussions. This research was supported by National Science and Engineering Research Council of Canada (NSERC).

Bibliography

[1] A. Varshney, S. Ghosh, S. Bhattacharya, and A. Yethiraj. Self organization of exotic oil-in-oil phases driven by tunable electrohydrodynamics. *Scientific Reports*, 2:738, 2012.

[2] A. P. Gast and W. B. Russel. Simple ordering in complex fluids. *Physics Today*, 51(12):24–30, 1998.

[3] W. Poon. Colloids as big atoms. *Science*, 304(5672):830–831, 2004.

[4] A. Yethiraj. Tunable colloids: control of colloidal phase transitions with tunable interactions. *Soft Matter*, 3(9):1099–1115, 2007.

[5] J. Dobnikar, A. Snezhko, and A. Yethiraj. Emergent colloidal dynamics in electromagnetic fields. *Soft Matter*, 9(14):3693–3704, 2013.

[6] D. A. Saville. Electrohydrodynamics: The Taylor-Melcher leaky dielectric model. *Annual Review of Fluid Mechanics*, 29(1):27–64, 1997.

[7] P. F. Salipante and P. M. Vlahovska. Electrohydrodynamics of drops in strong uniform dc electric fields. *Physics of Fluids*, 22(11), 2010.

[8] B. Kirby. *Micro- and nanoscale fluid mechanics: transport in microfluidic devices*. Cambridge University Press, New York, 2010.

[9] M. Singh, H. M. Haverinen, P. Dhagat, and G. E. Jabbour. Inkjet printing: Inkjet printing-process and its applications. *Advanced Materials*, 22(6):NA–NA, 2010.

[10] C. T. O'Konski and H. C. Thacher. The distortion of aerosol droplets by an electric field. *The Journal of Physical Chemistry*, 57(9):955–958, 1953.

[11] R. S. Allan and S. G. Mason. Particle behaviour in shear and electric fields. I. deformation and burst of fluid drops. *Proceedings of the Royal Society of London. Series A, Mathematical and Physical Sciences (1934-1990)*, 267(1328):45–61, 1962.

[12] G. I. Taylor. Studies in electrohydrodynamics. I. The circulation produced in a drop by electrical field. *Proceedings of the Royal Society of London. Series A, Mathematical and Physical Sciences (1934-1990)*, 291(1425):159–166, 1966.

[13] J. R. Melcher and G. I. Taylor. Electrohydrodynamics: A review of the role of interfacial shear stresses. *Annual Review of Fluid Mechanics*, 1(1):111–146, 1969.

[14] S. Torza, R. G. Cox, and S. G. Mason. Electrohydrodynamic Deformation and Burst of Liquid Drops. *Philosophical Transactions of the Royal Society of London. Series A, Mathematical and Physical Sciences (1934-1990)*, 269(1198):295–319, 1971.

[15] E. Zholkovskij, J. Masliyah, and J. Czarnecki. An electrokinetic model of drop deformation in an electric field. *Journal of Fluid Mechanics*, 472:1–27, 2002.

[16] J. A. Lanauze, L. M. Walker, and A. S. Khair. Nonlinear electrohydrodynamics of slightly deformed oblate drops. *Journal of Fluid Mechanics*, 774:245–266, 2015.

[17] A. Varshney, S. Gohil, M. Sathe, S. Rao R V, J. B. Joshi, S. Bhattacharya, A. Yethiraj, and S. Ghosh. Multiscale flow in an electro-hydrodynamically driven oil-in-oil emulsion. *Soft Matter*, 12(6):1759–1764, 2016.

[18] A. Groisman and V. Steinberg. Elastic turbulence in a polymer solution flow. *Nature*, 405(6782):53–5, 2000.

[19] J. D. Posner, C. L. Pérez, and J. G. Santiago. Electric fields yield chaos in microflows. *Proceedings of the National Academy of Sciences of the United States of America*, 109(36):14353–6, 2012.

[20] J. C. Baygents and D. A. Saville. Electrophoresis of drops and bubbles. *Journal of the Chemical Society, Faraday Transactions*, 87(12):1883–1898, 1991.

[21] O. Schnitzer and E. Yariv. The Taylor–Melcher leaky dielectric model as a macroscale electrokinetic description. *Journal of Fluid Mechanics*, 773:1–33, 2015.

[22] J. C. Crocker and D. G. Grier. Methods of digital video microscopy for colloidal studies. *Journal of Colloid and Interface Science*, 179:298–310, 1996.

[23] A. M. Fincham and G. R. Spedding. Low cost, high resolution DPIV for measurement of turbulent fluid flow. *Experiments in Fluids*, 23(6):449–462, 1997.

[24] A. Fincham and G. Delerce. Advanced optimization of correlation imaging velocimetry algorithms. *Experiments in Fluids*, 29(1):S013–S022, 2000.

[25] J. Petit, D. Riviére, H. Kellay, and J. Delville. Break-up dynamics of fluctuating liquid threads. *Proceedings of the National Academy of Sciences of the United States of America*, 109(45):18327–31, 2012.

[26] J. D. Sherwood. Breakup of fluid droplets in electric and magnetic fields. *Journal of Fluid Mechanics*, 188(1):133–146, 1988.

[27] R. Pillai, J. D. Berry, D. J. E. Harvie, and M. R. Davidson. Electrokinetics of isolated electrified drops. *Soft Matter*, 12(14):3310–3325, 2016.

[28] R. Karyappa, S. Deshmukh, and R. Thaokar. Breakup of a conducting drop in a uniform electric field. *Journal of Fluid Mechanics*, 754:550–589, 2014.

[29] H. Nganguia, Y. N. Young, A. T. Layton, M. C. Lai, and W. F. Hu. Electrohydrodynamics of a viscous drop with inertia. *Physical Review E*, 93(5):053114, 2016.

[30] J. Q. Feng. Electrohydrodynamic behaviour of a drop subjected to a steady uniform electric field at finite electric Reynolds number. *Proceedings of the Royal Society A: Mathematical, Physical and Engineering Sciences*, 455(1986):2245–2269, 1999.

[31] A. V. Getling. *Rayleigh-Bénard convection: structures and dynamics*. Advanced series in nonlinear dynamics. World Scientific, River Edge, NJ, 1998.

[32] A. Yethiraj and A. van Blaaderen. A colloidal model system with an interaction tunable from hard sphere to soft and dipolar. *Nature*, 421(6922):513–7, 2003.

[33] P. A. Vázquez, G. E. Georghiou, and A. Castellanos. Numerical analysis of the stability of the electrohydrodynamic (EHD) electroconvection between two plates. *Journal of Physics D: Applied Physics*, 41(17):10, 2008.

[34] A. Kourmatzis and J. S. Shrimpton. Characteristics of electrohydrodynamic roll structures in laminar planar couette flow. *Journal of Physics D: Applied Physics*, 49(4):13, 2016.

[35] J. D. Posner and J. G. Santiago. Convective instability of electrokinetic flows in a cross-shaped microchannel. *Journal of Fluid Mechanics*, 555:1–42, 2006.

4.7 Supplementary information

Movies 4.1 to 4.4 can be found in a CD attached to this thesis.

4.7.1 Drop breakup and coalescence

Breakup: Movie 4.1 (left panel, $E = 9.5$ V/μm) shows a time series for the breakup of a large pancake-shaped drop. Breakup events can be spotted at 7.4 s, 14.6 s, and 16.9 s Cell thickness $d = 27$ μm. The middle panel ($E = 8.5$ V/μm) shows the breakup a drop in a thicker ($d = 55$ μm) cell. Here the drop is close to spherical, and breakup occurs by deformations in the plane perpendicular to the field. Breakup occurs at 3.60 s.

Coalescence: Movie 4.1 (right panel, cell thickness $d = 96$ μm, $E = 3.5$ V/μm) shows a drop coalescence event. The third dimension is crucial to the coalescence event, with a drop detaching from a bounding substrate at around 0.7 s, moving above a larger drop. Both drops are oblate, so this configuration allows their flat faces to touch. Coalescence occurs at ≈ 2.5 s.

4.7.2 Drop dynamics

Movie 4.2 (left panel) shows a time series for the short-time dynamics of drops for $t < 0.9$ s. In this regime, the mean-square displacements are linearly dependent on time. $d = 55$ μm. $E = 12.5$ V/μm.

Movie 4.2 (right panel) shows the long-time dynamics ($t < 9$ s) for the same sample conditions. Some directed motion is observable.

Supplementary Figure 4.11 shows the mean square displacements as a function of time for the thinnest cell ($d = 27$ μm). This dependence can be fitted to a linear form for intermediate electric fields, and to MSD $= K_1 t + K_2 t^2$ for larger electric fields.

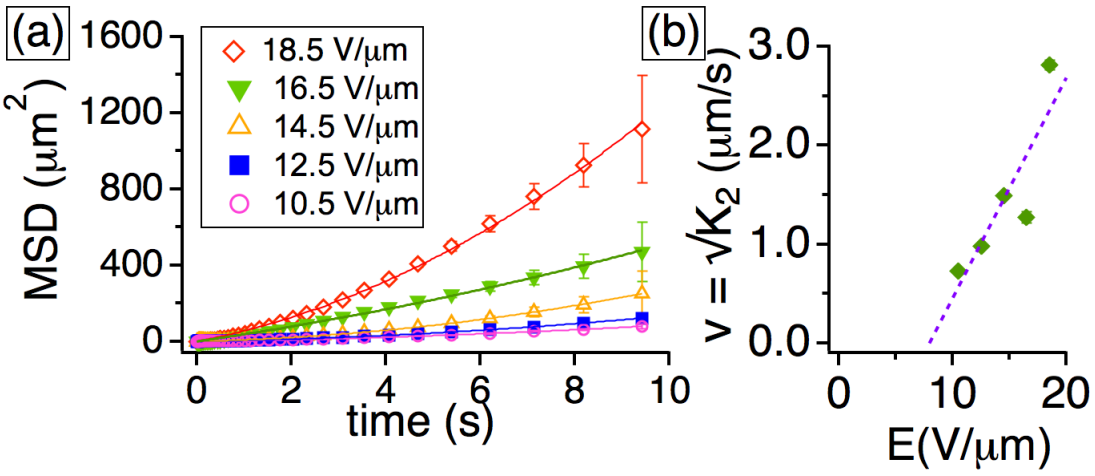

Figure 4.11: **Drop Dynamics.** (a): Mean-squared displacement as a function of time shows a roughly linear dependence at intermediate fields and quadratic dependence at higher fields. (b): The advective term can be obtained from the fits in (a). A linear fit is shown.

There is no motion at all for low fields. The prefactor to the quadratic term yields the advection: $v = \sqrt{K_2}$. Since the square of this speed is proportional to the kinetic energy, and E^2 is proportional to the injected electric field energy, one would expect that $v \propto E$.

4.7.3 Field thresholds

Two field thresholds are identified from the thickness dependence study and shown in FIG. 4.12. The first is the field threshold, as a function of cell thickness, where drop breakup occurs. The second is the field threshold, as a function of cell thickness, when drops are displacing and changing shape rapidly enough that particle tracking is not feasible.

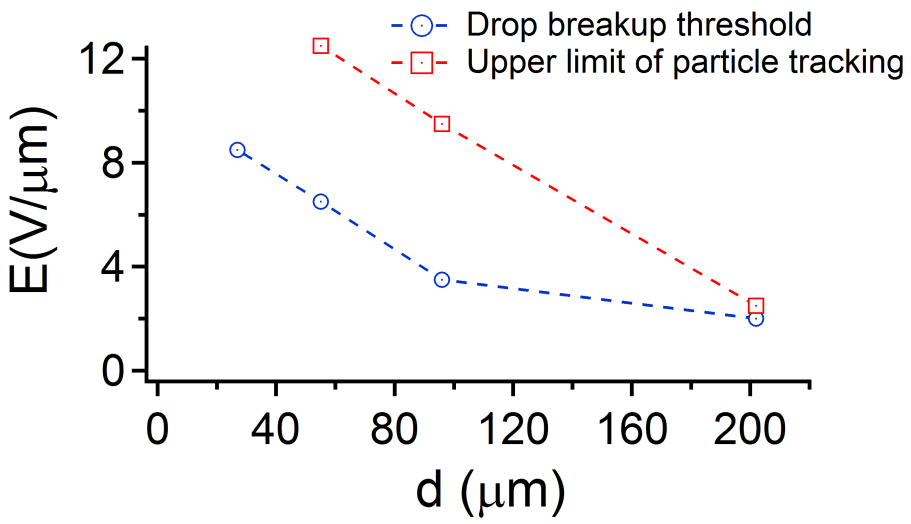

Figure 4.12: **Field Thresholds.** Field thresholds for drop breakup and for vigorous drop motion (evaluated by inability to track drops) as a function of cell thickness. For the $d = 27$ μm cell, particle tracking is always possible.

4.7.4 Convection with droplets and PMMA colloids

Movie 4.3 shows convection of droplets (left panel, $E = 4.5$ V/μm) and particles (PMMA colloids, right panel, $E = 2.4$ V/μm) close to the instability threshold.

4.7.5 Mixing of dyed and non-dyed castor oil in the presence of the electric field

Movie 4.4 shows the dynamics of the interface, obtained with time-lapse macro scale photography and white light illumination, between dyed castor oil (top) and non-dyed castor oil (bottom), without and with an applied electric field. Left panel: With $E = 0$ V/μm, there is no distinguishable motion of the interface over a period of 3 hours. Right panel: with the field on, $E = 8$ V/μm, rapid blurring of the interface between the dyed and non-dyed regions between the dyed and non-dyed regions is observed over a time scale of ≈ 15 minutes.

Chapter 5

Tunable hydrodynamics: A field-frequency phase diagram of a non-equilibrium order-to-disorder transition

Synopsis: Reprinted (adapted) with permission from Soft Matter (Royal Society of Chemistry Publishing Group)13(40), pp 7412-7424, 2017. S. Khajehpour Tadavani carried out the experiments and analysis and wrote the initial draft of the manuscript and implemented subsequent revisions. A. Yethiraj supervised the project, provided comments on the drafts and contributed to the final text of the manuscript.

5.1 Abstract

We present experiments on a model system consisting of dielectric (silicone oil) drops in a "leaky dielectric" (castor oil) carrier fluid that exhibits dynamic non-equilibrium phases as a function of the amplitude and frequency of an external AC electric field. At high frequencies, the dielectric drops are pinned to a periodic lattice by dielectrophoretic forces induced by a patterned bottom electrode. Beginning with this state of imposed order, we examine the processes that take this system from order to disorder, with decreasing frequency corresponding to an increase in the range of the hydrodynamic forces. We find two kinds of disordering, shape- and translational disordering, that occur in frequency – amplitude space. We also find regimes where drop breakup is dominant, and where order/disorder of large drops can be probed without significant drop breakup. With decreasing frequency (*i.e.*, increasing the hydrodynamic coupling between drops) and on timescales from seconds to minutes, the drops exhibit motion that resemble Brownian motion of particles in a crystal, with an effective temperature that increases with the strength of the electrohydrodynamic driving. In this limit, the system behaves like a thermal system and the lattice is seen to melt at an effective Lindemann parameter of $L_{\text{eff}} \sim 0.08$. This non-equilibrium thermodynamics, probed on timescales from seconds to minutes, likely arises from the pseudo-random velocity fields in the carrier fluid, as evidenced by the fractional, $t^{3/2}$, super-diffusive tracer dynamics at shorter timescales.

5.2 Introduction

Self-organization in colloidal systems has uncovered new phases that arise from a competition between entropy and tunable interactions between building blocks [1–5]; controlling interactions has been a powerful means to examine the nature of crys-

tal phases and phase transitions [6–10]. While there remain significant challenges to making highly ordered structures [11, 12], controllable *disorder* also has applications in natural systems: examples are the role of amorphous structures in biomineralization [13] and the role of disorder in the brilliant whiteness in beetle scales [14]. Thus, a better understanding of self-organization either in systems with greater complexity or in systems farther from equilibrium is necessary.

Self-organization in systems with greater complexity has been explored in Brownian colloidal suspensions by examining anisometric particle shape [15–17], soft and floppy microgel particles [18, 19] as well as particles with anisotropic [6, 20] and patchy interactions [21, 22]. In all these cases, the goal has been monodispersity in particle geometry, in order to keep the systems simple.

An understanding of non-equilibrium phase transitions is also relevant in biological systems: here, two examples are the relevance of principles of polymer physics inside cells [23, 24], and the relevance of model active matter systems [25, 26] for transport processes within cells. Granular systems with building blocks of size 10 μm or greater are invaluable as model systems that extend the statistical physics of phase transitions to non-Brownian systems [27–29]; this includes the study with single-particle resolution of dynamical phase transitions such as jamming. However, a key ingredient in biological cells is the existence of soft liquid-liquid interfaces and the formation of compartments with or without membranes [30]. In contrast with colloidal suspensions, even the particle size in liquid-liquid emulsions is achieved by self-organization, so they are inherently more complex.

A recently introduced model system in a liquid-liquid emulsion [31] with drop size on the $10 - 100$ μm scale is directly tunable *via* an electrically driven hydrodynamic interaction. Decreasing the frequency of the driving electric field has been shown to enhance the hydrodynamic coupling between drops [31], with multiscale flows remi-

niscent of turbulence observed in the zero-frequency (d.c.) limit [32, 33]. Moreover, non-uniform fields have been employed to create periodic droplet arrays for microlens applications [34]. This tunability of collective behaviors suggests that it could be valuable as a non-equilibrium model system: this is the focus of the current study. Aqueous media have been employed as well in order to induce and control structure formation using electrohydrodynamics [35–38], so concepts developed in this system could be transferred to aqueous environments.

In this study we employ a time-varying external AC electric field with *two* control parameters, the amplitude and the frequency, to examine non-equilibrium order-to-disorder processes in a hexagonal array of silicone oil drops, as internal liquid, surrounded by castor oil, as a partially charged external liquid. For a two-dimensional array of drops, we study the shape deformation of drops, as well as their translational and orientational dynamics, as the driving force is increased in two ways, either by increasing field amplitude or by decreasing frequency.

5.3 Methods and techniques

5.3.1 Samples and hardware

FIG. 5.1(a) shows the side view of a test cell with the electric field perpendicular to the microscope slide (*i.e.* perpendicular to our field of view) and parallel to gravity. Two indium tin oxide, ITO, coated cover glass slides are separated by glass spacers with defined thickness of h = 140 μm. As shown in FIG. 5.1(b), the ITO bottom plate, is selectively etched by photo-lithography such that a hexagonal array of roughly circular ITO-free regions, diameter $\sim$ 50 μm and with nearest-neighbor center-to-center spacing $d_{nn} \sim 100$ μm, is obtained. The plates and spacers are held together with ultraviolet-curable epoxy, Norland Optical Adhesive 61 and 68.

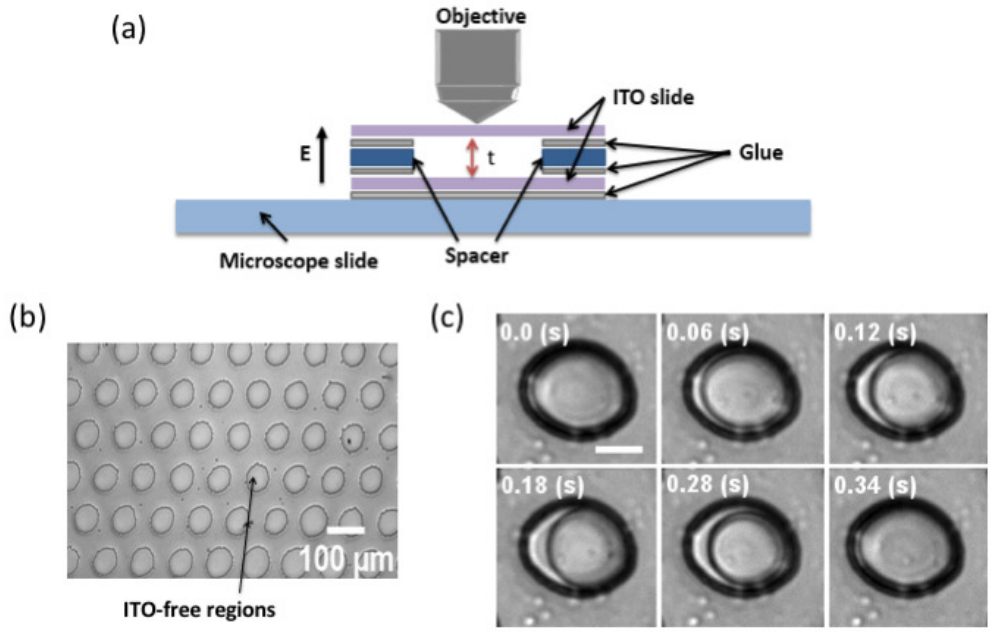

Figure 5.1: (a): A schematic design: side view of the cell geometry, (b): Bottom electrode with ITO-free regions shown by circles. (c): Drop shape within one field cycle. When one images a drop rapidly, one sees periodic oscillations at intermediate times of $0.06, 0.12, 0.18$ and 0.28 s between the two maximums of oscillation, at 0 s and 0.34 s. The dark edges show the edge of the circular pattern and overlaid droplets. In intermediate times, the edge of the drops are not overlaid on the edge of patterns. $f = 3$ Hz, $E = 5.6$ V/μm and is perpendicular to the page. Scale bar is 25 μm.

The ITO slides are optically transparent and electrically conductive, which enables their use as electrodes and to image through them as with regular glass. The cell is filled by pipetting an emulsion of silicone oil, dielectric constant $\varepsilon_{in}/\varepsilon_0 = 2.4$, conductivity $\sigma_{in} = 3.95 \times 10^{-11}$ S/m, and viscosity $\mu_{in} = 0.137$ Pa $\cdot$ s, and castor oil, dielectric constant $\varepsilon_{ex}/\varepsilon_0 = 3.6$, conductivity $\sigma_{ex} = 4.0 \times 10^{-10}$ S/m, and viscosity $\mu_{ex} = 0.819$ Pa $\cdot$ s, in a volume ratio of $1 : 16$. The subscripts in and ex are used to represent the droplet and the suspending fluid, respectively. The lateral dimension of cells is ~ 0.75 cm.

A sinusoidal AC voltage, provided by Tektronix model $AFG3022$ function genera-

tor, is applied to the cell, while the output voltage of the power generator is amplified by a high voltage amplifier, provided by Trek model $PZD2000A$ wideband high-voltage amplifier. Bright field microscopy is used to observe and record the image sequences.

5.3.2 Image processing

The long-time dynamics of trapped droplets, located on the etched-out patterns, is studied by filtering out the periodic oscillations *via* the expedient of stroboscopic imaging at the frequency of oscillation. The usefulness of this technique has been shown in FIG. 5.1(c) by 6 snapshots at equal intervals within a full cycle of oscillation at 3 Hz. The first and last frame are the beginning and end of the cycle, while the four intermediate oscillations are ignored in the strobe technique.

The second channel of the AC function generator produces a square wave with the driving frequency and a peak-to-peak amplitude of 2.5 V in order to trigger image acquisition by the camera. To get the maximum of drops' deformation a phase difference of $+90^\circ$ between the two periodic waves is applied to the sinusoidal wave while the bottom and the top electrodes are connected to negative and positive electrodes, respectively.

After recording the experiment, the shape deformation and positions of the droplets are studied. A typical field of view (such as those shown in FIG. 5.4) consists of 21 drops. All analyses were repeated in different regions of the same cell and also for a new cell with the thickness roughly equal to the current cell. To lowest order, a deformed circle may be approximated as an ellipse. An ellipse-fitting algorithm (`http://www.asu.cas.cz/~sos/software/mpfitellipse.pro`, written in IDL (Interactive Data Language), is used to fit an approximate ellipse to the points forming the drops in a binary image. The output consists of the major axis L, the minor axis

l, centroid (x, y), and angle of the major axis with respect to the x-axis. The shape deformation of the drop is quantified by the unitless "roundness",

$$R = 4A_{cs}/\left(\pi L^2\right) = 1/S, \tag{5.1}$$

where the area $A_{cs} = \pi Ll/4$ and $S = L/l$ is the aspect ratio of the drop. R can vary between 0 and 1 with unity representing perfectly round objects. Using the centroid of the fitted ellipse, one is also able to track droplet motion using standard particle tracking techniques [39]. From this, we obtain (Section 5.5.4) the 2D mean square displacement, $\langle \triangle r^2 \rangle$, where r is the magnitude of the displacement of each ellipse as a function of the time t (from a reference start time t_0), and $\langle \cdot \rangle$ is an average over all the ellipses in the system, and over the reference time. Using the centroid of the drops, one can also obtain the pair correlation function, $g\,(r)$, and bond order parameter, $\langle \Psi_6 \rangle$.

The time correlation of drop orientations, obtained for different frequencies and amplitudes using an auto-correlation function, is implemented in IDL (`http://www.harrisgeospatial.com/docs/A_CORRELATE.html`).

5.3.3 Brief summary of experiments

The silicone oil drops are prepared prior to each experiment so that they are located, using the negative dielectrophoretic force, described in Section 5.4.2, at the patterned holes in the ITO-film electrode and have a diameter of 50 μm. While the cell has a thickness of 140 μm, there is free space (filled with the leaky dielectric, castor oil) above the silicone oil drop, which thus assumes the shape of a section of a hemisphere, which in a top view is circular.

The non-deformed state of each drop is roughly hemispherical; this is the drop

shape at low amplitudes or high frequencies. In our experiments, we hold the electric field amplitude fixed and observe the time dependence of drop deformations for a sweep of frequencies. Then, we change the amplitude and repeat the experiment. For each experiment, we image the drop stroboscopically (except in Section 5.5.5 where we probe dynamics at times much shorter than one period of the sinusoidal electric field oscillation). The drop is imaged close to the bottom substrate, 10 μm above it, in order to put the edge of the ITO pattern area out of focus and yet not changing the detected drop area significantly.

5.4 Background and theory

In order to incorporate tunable hydrodynamics into a model granular crystal we combine three elements: electrohydrodynamics in a two-fluid emulsion, dielectrophoresis as a means of droplet trapping, and a methodology to measure displacement fluctuations in a crystal. In what follows, we present the related background concepts.

5.4.1 Electrohydrodynamics of two-fluid emulsions

In an emulsion of two immiscible dielectric liquids ("internal" and "external"), the shape of a drop of the internal liquid is spherical in the absence of external forces due to the minimization of surface energy. An external electric field induces bound polarization charge resulting in a force normal to the liquid-liquid interface that changes the shape to a prolate ellipsoid. This shape deformation occurs when the dimensionless electric capillary number, which is the ratio of electric forces and restoring interfacial tension acting on a drop, *i.e.*, $Ca_E \sim \varepsilon_{ex} a E^2/\gamma$, is comparable to unity. In a suspension composed of a dielectric internal fluid and a "leaky dielectric" external fluid with large enough ionic conductivity, σ_{ex}, an electric field results in continuous steady state

electrohydrodynamic flows. In an AC electric field, the field amplitude and frequency can both be utilized to tune the strength and the range of the resulting electrohydrodynamic (EHD) interactions. The generic behavior is rather well described by the lumped-parameter leaky dielectric model (LDM) [40–42] which ignores the finite Debye screening length at the liquid-liquid interfaces [43]. The deformations of the internal liquid is characterized by a balance of three forces: the bound polarization charge (normal to the interface), the induced free charge (normal and tangential to the interface), and viscous forces (also normal and tangential to the interface) [43]. The drop deformation $D = \left(d_{\parallel} - d_{\perp}\right) / \left(d_{\parallel} + d_{\perp}\right)$ can be measured experimentally, and may be related to the system parameters:

$$D = \Phi \, \frac{a \, \epsilon_{ex} E^2}{\gamma}, \tag{5.2}$$

where a is the radius of a non-deformed drop and Φ is a shape-discriminating function that is given by

$$\Phi = \frac{9}{16}\left(1 - \frac{H^{-1}\left(11M+14\right) + H^{-2}\left(15\left(M+1\right) + S\left(19M+16\right)\right) + 15\tau^2\omega^2\left(1+M\right)\left(1+2S\right)}{5\left(1+M\right)\left(\left(2H^{-1}+1\right)^2 + \tau^2\omega^2\left(S+2\right)^2\right)}\right). \tag{5.3}$$

Φ may be used to classify deformations as non-spherical (prolate or oblate), or spherical [42]. In Equation (5.3), for our system, $S = \dfrac{\varepsilon_{in}}{\varepsilon_{ex}} = 0.67$, $H = \dfrac{\sigma_{in}}{\sigma_{ex}} = 0.10$, $M = \dfrac{\mu_{in}}{\mu_{ex}} = 0.17$, $\tau = \dfrac{\varepsilon_{ex}}{\sigma_{in}} = \dfrac{\varepsilon_0 k_{ex}}{\sigma_{in}} \simeq 0.81$ s, $\omega = 2\pi f$. The parameters ε, σ, and η are absolute permittivity, conductivity, and viscosity of liquids, while k and ε_0 are the relative permittivity and the vacuum permittivity, respectively. The frequency of the field f is the only variable in the equation. The subscripts in and ex are used to represent the droplet and the surrounding fluid, respectively. Prolate and oblate deformations result when $\Phi > 0$ and $\Phi < 0$ respectively, while the drop stays spherical

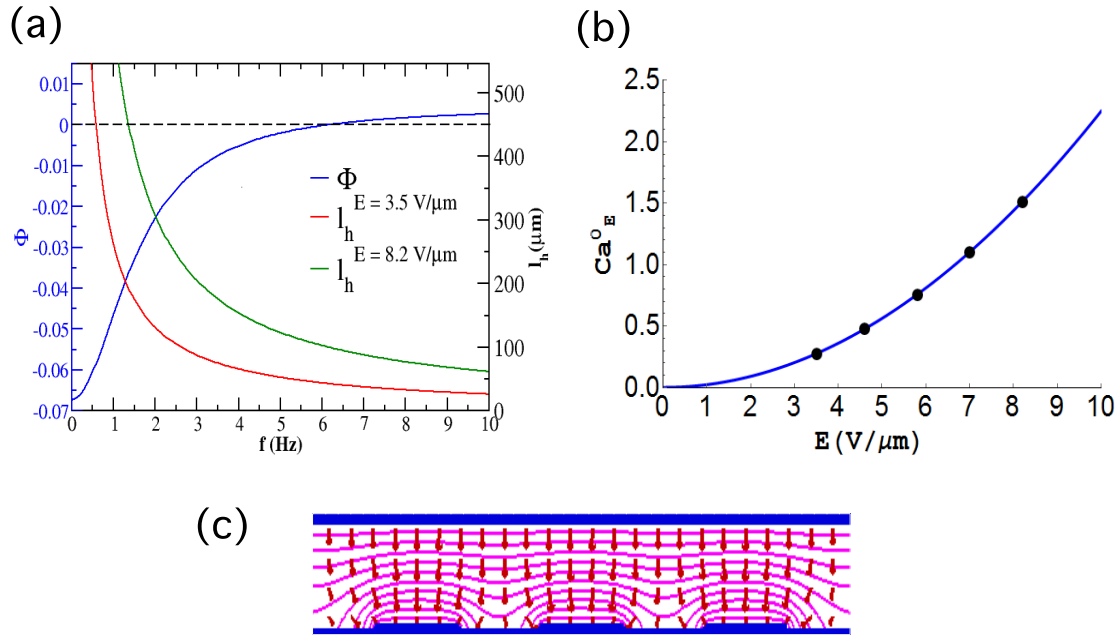

Figure 5.2: (a): The shape-discriminating function, Φ, is greater than zero at high frequency (prolate drops), but becomes negative (oblate drops) at roughly 6 Hz. The hydrodynamic length, l_h decreases inversely with frequency, but increases proportionally with field amplitude. (b): Electric capillary number, Ca_E^0, versus electric field amplitude, E. As Ca_E^0 approaches unity, the smooth liquid-liquid interface should destabilize and lead to drop breakup. The points indicate the experimental field values used. (c): Simulation of electric field in a cell with a uniform top conducting electrode and a bottom electrode with non-conducting holes. The low electric field regions have less dense equipotential lines and smaller electric fields vectors (denoted by arrows). The gradient of this non-uniform electric field forces the liquid with lower dielectric constant, ε, into low electric field regions.

when $\Phi = 0$. FIG. 5.2(a) represents Φ versus f for the current system, where the crossover frequency from oblate to prolate is roughly 6.1 Hz.

The strength of EHD forces, and the strength of the resulting drop deformations, is governed by the electric field amplitude. Feng [44] wrote a modified electric capillary number for EHD using the maximum velocity assuming creeping flows around a non-deformed drop,

$$Ca_E^0 \equiv \frac{9 \mid S^{-1}H - 1 \mid M^{-1}}{10\,(H+2)^2\,(M^{-1}+1)} \frac{\varepsilon_{in} a E^2}{\gamma}, \tag{5.4}$$

where $\gamma \simeq 3 - 4$ mN/m is the interfacial tension between the oils, $\varepsilon_{in} = \varepsilon_0 k_{in} = 21.24 \times 10^{-12}$ F/m, a is radius of the non-deformed drop and E is the strength of the field. For the current system, we can write $Ca_E^0 = 0.9 \times 10^{-9} a E^2$ where $a = 25$ μm is the initial drop radius, (a and E are expressed in mks units). The superscript "0" refers to the electric Capillary number at the initial drop diameter. Variation of Ca_E^0 versus E is plotted in FIG. 5.2(b): circles are the values of electric field amplitude used in this work.

The range of the electrohydrodynamic (EHD) interactions can be modulated by changing the frequency, f. Varying f affects the lengthscale of hydrodynamics interactions, $l_h = v_d/f$, where $v_d = \mu_E E$ is the ionic drift velocity, that is set by the electric mobility μ_E and the electric field, E. The electric mobility in turn is $\mu_E = z_i e_0 / 6\pi r \mu_{ex}$ [45], where $z_i e_0$ is the ions' charge, and r is the radius of ions. The electric mobility of the current system is $\mu_E \simeq 75$ μm^{2}V^{-1}s^{-1}. FIG. 5.2(a) shows the inverse relation of the hydrodynamic length versus frequency for two field amplitudes. At the crossover frequency of ≈ 6 Hz, l_h is < 50 μm for $E = 3.5$ V/μm and ≈ 100 μm for $E = 8.2$ V/μm; i.e, it is smaller than and equal to, respectively, the drop nearest-neighbor spacing $d_{nn} = 100$ μm, while at 2 Hz, $l_h > d_{nn}$ for all field amplitudes probed. The frequency regime below 6 Hz is therefore where we expect interesting electrohydrodynamic behaviors.

Φ is a function of frequency (and not field amplitude), while the electric Capillary number, Ca_E^0, is a function of field amplitude (and not frequency). Both control deformation of individual drops. The hydrodynamic length, l_h, which is a function of both, defines the lengthscale over which drops couple with neighboring drops.

5.4.2 Dielectrophoretic trapping of drops

We employ dielectrophoresis to prepare a periodic lattice of drops, using the methods demonstrated previously [34]. A patterned electrode creates a non-uniform electric field. A dielectric drop in a dielectric liquid responds to the field non-uniformity *via* the dielectrophoretic force, F_{DEP},

$$F_{DEP} = \frac{1}{2}\left(\varepsilon_{in} - \varepsilon_{ex}\right) \nabla \left(\mathbf{E} \cdot \mathbf{E}\right), \tag{5.5}$$

which, in the long-time steady state, creates a spatially localized array of silicone oil drops in castor oil, or more generally, a patterned arrangement of two immiscible dielectric liquids with different dielectric constants [34]. FIG. 5.2(c) shows a simulation (using Poisson Superfish `http://laacg.lanl.gov/laacg/services/serv_codes.phtml`) of the equipotential lines, as well as the electric field amplitude and direction (vectors on a grid) above a patterned electrode. The region with holes in the conducting surface has sparse collections of equipotential lines as well as vectors with the most rapidly changing amplitude, and this region attracts the oil with lower dielectric constant. These holes in the bottom electrode are thus a trap for the silicone oil, and thus make this system quasi-two-dimensional.

5.4.3 Bond-orientational order

Order and disorder in two-dimensions is characterized by a bond-orientational order parameter [46]. For 6-fold symmetric structures, such as the symmetry of the periodic lattice imposed by dielectrophoretic methods in this work, the relevant order

parameter is

$$\Psi_N = \left| \frac{1}{N} \frac{\sum_{j=1}^{N} l_j e^{i6\theta_j}}{\sum_{j=1}^{N} l_j} \right|, \tag{5.6}$$

where N is the number of nearest neighbors at drop j, l_j is the line segment that connects the neighbors $j-1$ and j, and θ_j is the angle which the vector from the selected drop to the jth neighbor makes with respect to the x axis [47, 48]. Ψ_6 can vary between 0 and 1, with 1 indicating perfect 6-fold symmetry. For drops designated as 6-fold sites ($\Psi_6 > 0.7$), $\langle \Psi_6 \rangle$, is calculated in one frame and then averaged over an image stack that represents a time series.

5.4.4 Study of dynamics in a soft crystal

When electric fields are applied in our leaky dielectric model system, they generate pseudo-random flows in the carrier fluid. These flows, in turn, generate drop motions, that can be examined as if it were effective diffusion [33]. Since we have drops on a lattice in this work, we examine our system by employing an analog to that of colloid diffusion in a crystal lattice.

In a fluid and in a crystal, the mean-squared displacements of atoms yields important information: the self-diffusivity in a fluid, and the elastic constant in a crystal. In soft crystals, and in two dimensions, one can write the mean-squared displacement (MSD), following Weiss *et. al.* [49], as

$$\mathrm{MSD} = \left\langle \left(r\left(t\right) - r\left(0\right) \right)^2 \right\rangle = \frac{\beta k + \dfrac{1}{4Dt}}{\left(\dfrac{\beta k}{2} + \dfrac{1}{4Dt} \right)^2}, \tag{5.7}$$

where $\beta^{-1} = k_B T$, k is the spring constant, D is the effective diffusion coefficient, and t is time. At $t \to 0$, the behavior is simply diffusive: $\mathrm{MSD}_{t \to 0} = 4Dt$. Due to

the stroboscopic imaging, the shortest time probed is $t = 1/f$, and we have limited data with which to access to short time behavior to extract the effective diffusivity D; however, the asymptotic long-time value of the MSD yields

$$\mathrm{MSD}_{\mathrm{t}\to\infty} = \langle (r\,(t) - r\,(0))^2\,(t \longrightarrow \infty)\rangle = \frac{4}{\beta k}. \tag{5.8}$$

A similar interplay of linear time dependence followed by a plateau is seen in colloids (which display Brownian diffusion) in the presence of an optical trap (which acts as a harmonic restoring force [50] at least at small trapping strengths [51]). One may relate the long-time saturation value of the MSD with an effective Lindemann parameter

$$L_{\mathrm{eff}} = \frac{1}{d_{nn}}\sqrt{\frac{3}{4}\,MSD_{t\longrightarrow\infty}} = \frac{1}{d_{nn}}\sqrt{\frac{3}{\beta k}}, \tag{5.9}$$

where d_{nn} is the crystal nearest-neighbor distance [52].

5.5 Results and discussion

5.5.1 Electrohydrodynamic drop deformation

In the presence of an external AC electric field, for frequencies below the crossover frequency shown in FIG. 5.2(a) where $\Phi < 0$, a silicone oil drop becomes oblate, *i.e.*, it undergoes a vertical compression, and thus expands laterally. The two-dimension, lateral view of this time-dependent, periodic expansion can either be symmetric and circular or non-circular, depending on the strength of the driving field, but it is roughly periodic due to the time-dependence of the AC electrohydrodynamic forces. By imaging the system stroboscopically, one can follow subtle deviations from periodicity in the long-time lateral orientational and translational dynamics of the drops, once per cycle, as a function of the amplitude and the frequency of the driving electrohydro-

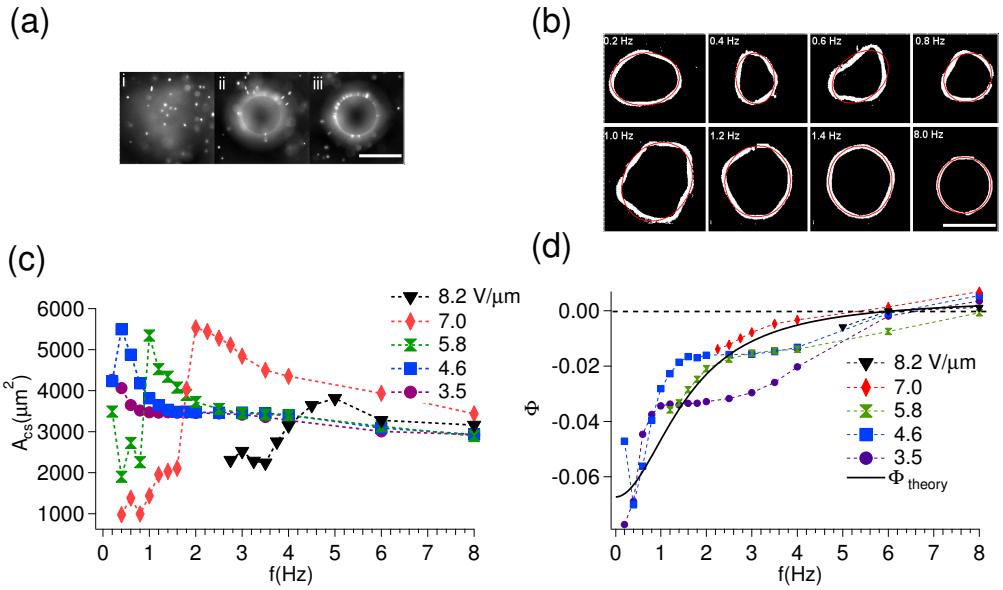

Figure 5.3: (a): A silicone oil drop in an emulsion of castor oil with fluorescent PMMA tracer particles is imaged at (i) 110 μm, (ii) 10 μm and (iii) 0 μm from the bottom electrode by fluorescence microscopy. The drop is roughly hemispherical and does not touch the top electrode. $f = 8$ Hz, $E = 7.0$ V/μm, perpendicular to the page. Scale bar is 50 μm. (b): A binarized image of the drop at the first few lower $(0.2, 0.4, 0.6, 0.8, 1.0, 1.2, 1.4$ Hz) and the highest (8.0 Hz) frequencies with fitted ellipse overlaid in red. $E = 5.8$ V/μm and is perpendicular to the page. Scale bar is 50 μm. (c): Variation of the fitted ellipse lateral cross-sectional area, A_{cs}, of one drop with frequency, for different field amplitudes. (d): Experimental plot of Φ, obtaining from 2D images of deformed droplets at different electric fields. A good agreement between observations and the theoretical expectation for the frequency dependence is observed, both in terms of (the negative to positive) crossover frequency and magnitude of Φ.

dynamic forces.

One can measure Φ experimentally using Equation (5.2). When a uniform sphere becomes an oblate spheroid, the lateral cross-sectional image shows a circle with increased area. To measure D from 2D snapshots, one needs to measure $d_{\parallel}$ (*i.e.*, parallel to the vertical electric field) and $d_{\perp}$ (in the image plane, which is perpendicular to the vertical electric field). In actual fact, in the image plane the drop is a deformed circle which can be approximated as an ellipse. A fit therefore yields two values,

$d_{1\perp} = L/2$ and $d_{2\perp} = l/2$, where L and l are the major and minor axes of an ellipse with area $A_{cs} = \pi d_{1\perp} d_{2\perp} = \pi Ll/4$.

Snapshots of a drop shown in FIG. 5.3(b) ($E = 5.8$ V/μm) show that with decreasing frequency, the drops become larger in cross section and also increasingly non-circular. Below 1 Hz in FIG. 5.3(c), the drop shrinks in size due to the breakoff of tiny droplets from the large drops. The sudden increase or decrease in area of the drops at low frequencies is due to the breakup/coalescence of droplets. The variation of the fitted ellipse cross-sectional area, A_{cs}, of a drop at different frequencies is plotted in FIG. 5.3(c) for the field amplitudes employed in this work. While A_{cs} is roughly the same at high frequencies for all field amplitudes, with decreasing frequency there is first an increase, corresponding to a shape change from spherical to oblate spheroidal. This larger cross-section correlates with a smaller vertical extent due to volume conservation of the drop.

For a non-deformed drop, close to crossover frequency, where $a = d_{\parallel} = d_{1\perp} = d_{2\perp}$, the volume can be measured using $V_0 = 4\pi\ a^3/3$. By lowering the frequency, before the breakup of the drop, a spherical drop changes into an ellipsoid, while the volume of the drop stays constant, $V_{ellipsoid} = V_0$, so one can measure $d_{\parallel} = V_0/\left(4\pi d_{1\perp} d_{2\perp}/3\right) \equiv V_0/\left(4A_{cs}/3\right)$. In addition, we may simply obtain $d_{\perp}$ using $d_{\perp} = \sqrt{A_{cs}/\pi}$. The experimental values of Φ, obtained from the experimental D using Equation (5.3), are shown in FIG. 5.3(d) (symbols refer to experiments at different electric field amplitudes), and are in good agreement with the theoretical value (solid black curve) in both the crossover frequency, $\simeq 6$ Hz, and the decrease of the amplitude of Φ at low frequency.

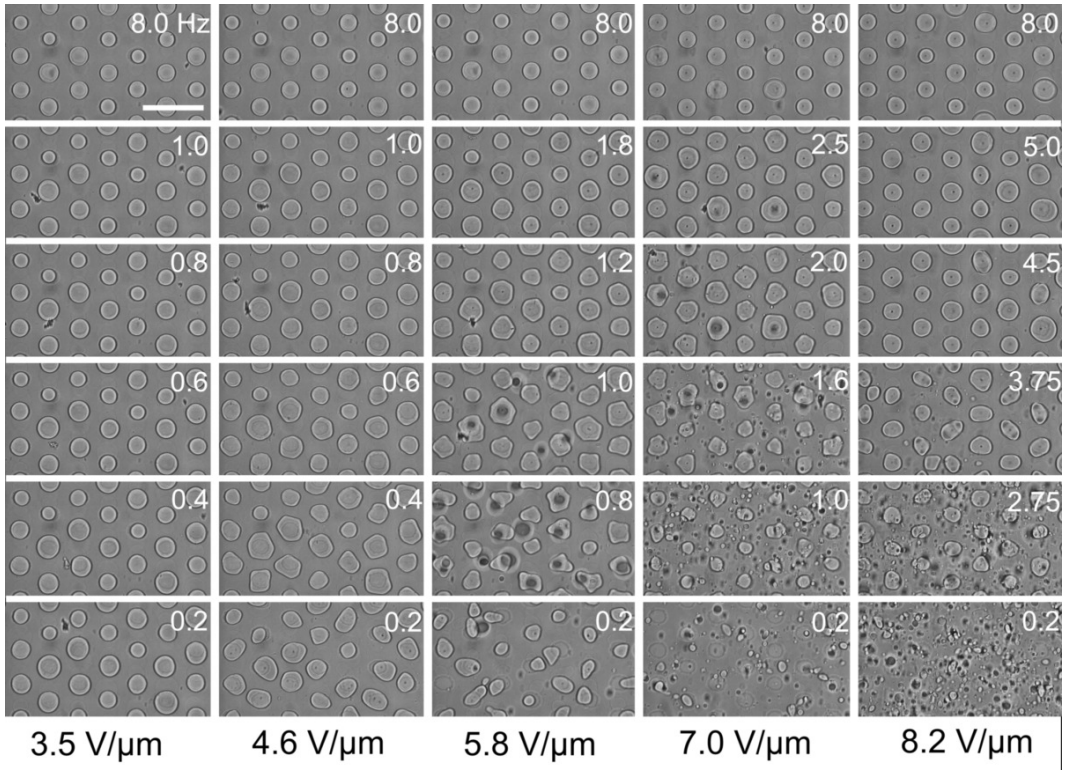

Figure 5.4: Order to disorder phase transition of the silicone oil array, surrounded in castor oil, by decreasing frequency (top to bottom) and increasing strength (left to right) of an AC electric field. The darker spots are out of focus droplets. A snapshot from each value of amplitude and frequency may be seen in Supplementary information, Section 5.9.2, Movie 5.1. Scale bar is 200 μm; and the electric field is perpendicular to the page.

5.5.2 An order-disorder transition

FIG. 5.4 shows pictorially the field- and frequency-dependence of an order-to-disorder transition in a silicone oil drop array in a castor oil background. A snapshot from each value of amplitude and frequency may be seen in Supplementary information, Section 5.9.2, Movie 5.1. At each field amplitude, we see the effect of lowering the AC frequency, and thus increasing the hydrodynamic length. For the lowest field amplitude reported ($E = 3.5$ V/μm, $Ca_E^0 \simeq 0.27$), we find that upon decreasing frequency from 8 Hz to 0.2 Hz (top to bottom in the first vertical panel in FIG. 5.4) we

see a modest increase in cross-sectional area of the drop (purple circles in FIG 5.3(c)). The drops are also slightly more displaced from their equilibrium position at the lowest frequencies, driven by fluid motion; this can be deduced qualitatively from the motion of a black dust particle (seen at different locations in the $1, 0.8$, and 0.2 Hz graphics).

At a higher field amplitude ($E = 4.6$ V/μm, $Ca_E^0 \simeq 0.48$), one observes by decreasing frequency from 8 Hz to 0.8 Hz (top to bottom in the second left vertical panel in FIG. 5.4) that drops not only have larger lateral area (blue squares in FIG 5.3(c)), but that below a threshold frequency, the circular droplets changed into faceted drops, going from circular to polygonal, at 0.6 and 0.4 Hz and then to disordered and random shapes at 0.2 Hz. No drop breakup/coalescence is observed for $E = 3.5$ V/μm and $E = 4.6$ V/μm.

At the next higher field ($E = 5.8$ V/μm, $Ca_E^0 \simeq 0.76$) one new element is introduced: the breakup. This is seen at and below 1 Hz (middle panel in FIG. 5.4): the darker spots in FIG. 5.4 are locations of drop break up, and drops get depinned from their trap locations. There is a balance between breakup of larger drops and coalescence of smaller droplets, with the end result being a shift of the peak in the drop size distribution to smaller values; this has been discussed in earlier work [32, 33]. With the consequent reduction in drop size and Ca_E^0, the polygonal shapes are transformed to curved-edge shapes at 0.8 Hz. For 0.4 Hz and 0.2 Hz, the drops appear rather detached from the traps.

At $E = 7.0$ V/μm ($Ca_E^0 \simeq 1.1$), (the fourth vertical panels in FIG. 5.4), much the same behavior is observed, except at a higher frequency of about 2.0 Hz. Similarly, the polygonal deformation is observed from 2.75 to 2.0 Hz, followed by curved-edge shapes from 1.8 Hz to 1.4 Hz.

At the highest field, however, $E = 8.2$ V/μm ($Ca_E^0 \simeq 1.51$), rather than a tran-

sition from circular to polygonal, one observes orientational deformation between 5.0 and 3.5 Hz. The increase in drop area (black triangles in FIG 5.3(c)) is also much less pronounced than for lower field amplitudes, owing to earlier onset of drop breakup. Drop breakup and coalescence are nevertheless observed at frequencies below 4 Hz.

One can quantify these observations by tracking the height of the first peak of the pair correlation function, $g(\sigma)$, and the roundness, R (defined in Equation (5.1)), of droplets as a function of frequency and amplitude: these are shown in FIG. 5.5 (a) and (b), respectively. A common transition at all field amplitudes is a transition to non-circular lateral drop shapes with decreasing frequency, which is followed by depinning of drops from their trapped positions at slightly lower frequency: the latter correlates with a decrease in the height of the nearest neighbor peak. This happens (filled circles in FIG 5.5(b)) at 4.5 Hz at $E = 8.2$ V/μm and 0.6 Hz at $E = 4.6$ V/μm. For all fields above $E = 3.5$ V/μm, the roundness reaches a low value between 0.75 and 0.85. The highest field ($E = 8.2$ V/μm) is different, because there is a fall with decreasing frequency in roundness, first near 3.75 Hz, then an increase, then a second decrease near 2 Hz.

In general, the non-monotonic increase in R likely arises from a decrease in Ca_E due to a reduction in drop size after breakup. The dynamics of the droplets close to the frequency threshold separating circular from non-circular droplets is seen for different field amplitudes in Supplementary information, Section 5.9.2, Movie 5.2.

The transition from order to disorder is quantified using $\langle \Psi_6 \rangle$ (defined in Equation (5.6)), and is shown in FIG. 5.6 for different frequencies and field amplitudes. $\langle \Psi_6 \rangle$ is close to 1 for all field amplitudes at a frequency of 8 Hz; the small deviation from 1 at this frequency comes from a small asymmetry in the lattice. $\langle \Psi_6 \rangle$ decreases from 1 as frequency is decreased: there is noticeable decrease already at 6 Hz for $E = 8.2$ V/μm, while for $E = 3.5$ V/μm, the decrease in $\langle \Psi_6 \rangle$ is only noticeable

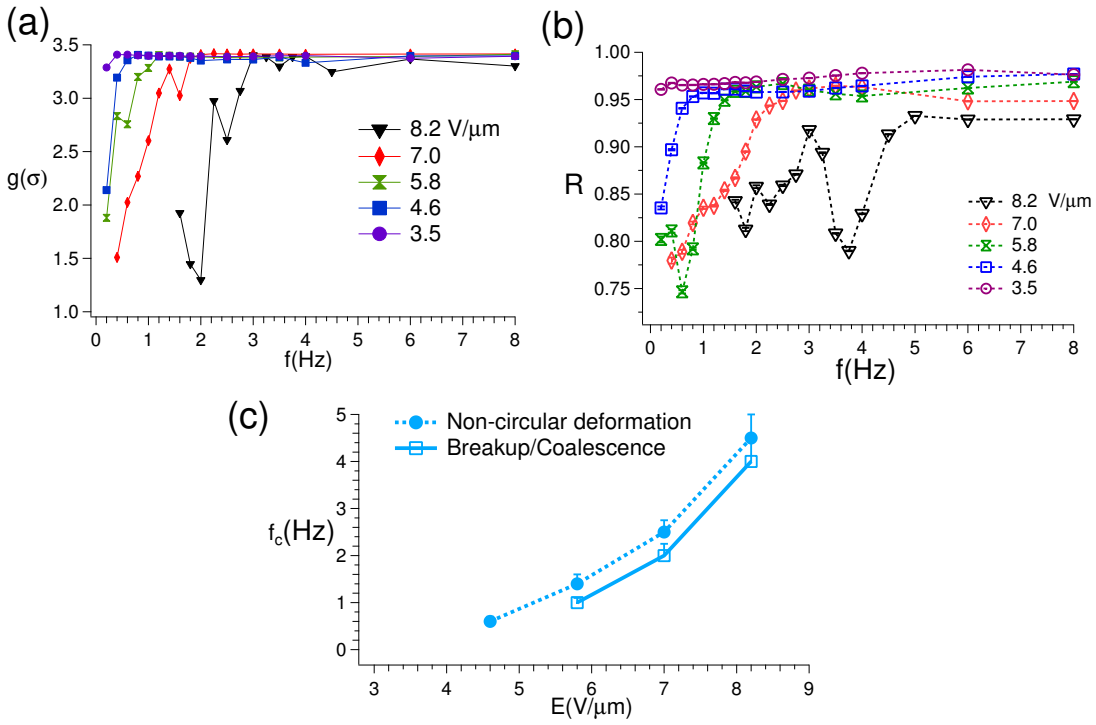

Figure 5.5: (a): The height of the first peak of the $g(r)$, *i.e.* $g(\sigma)$, where σ is the nearest-neighbor distance, versus frequency and for different field amplitudes. $g(\sigma)$ decrease with decreasing frequency for each field amplitude. (b): Roundness, R, as a function of frequency and field amplitude. For a perfect circle drop, roundness is close to 1. R decreases with either increasing field amplitude or decreasing frequency, with a low value of about 0.75. (c): The characteristic frequency, f_c, versus field amplitude, for non-circular deformation (filled circles) and for breakup (squares). f_c in all cases increases with field amplitude.

below 1 Hz. At high enough fields or low enough frequency, strong EHD flows result in the loss of drops due to escape or breakup. Because $\langle \Psi_6 \rangle$ depends on the existence of an intact neighborhood, it is not so useful in characterizing the disordered state. To quantify this state, we examine next orientational and translational dynamics, both of which are accessible via single-drop quantities.

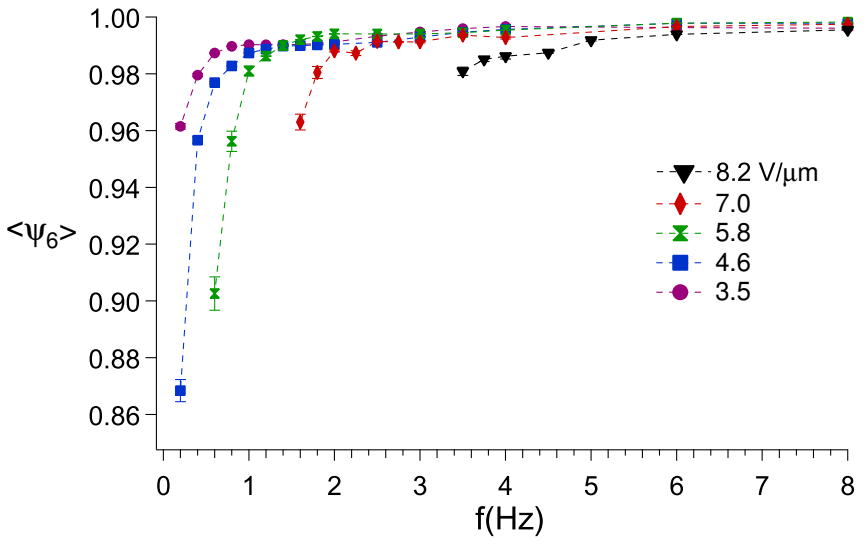

Figure 5.6: Average local bond-orientational order parameter $\langle \Psi_6 \rangle$ versus frequency and for each field amplitude. The 6-fold symmetry decreases by lowering the frequency.

5.5.3 Orientational dynamics of drops

Having measured roundness, we next look at the dynamics of deviation of the lateral shape of a drop from roundness. For small fluctuations, each drop can be treated as an ellipse with a major and minor axis. We follow the orientational dynamics of drops as a function of frequency and amplitude, using the auto-correlation of angular variation in ellipticity of the drop. The auto-correlation function, $C(t)$, with respect to $t = 0$, *i.e.*, $C(t) = \cos(\theta - \theta_0)$, where θ and θ_0 are the angles of fitted ellipse on the binary drop at time t and t_0, respectively. Then, in the frame of interest, a spatial average of $C(t)$ over all drops is calculated. An example, at 8.2 V/μm and 4 Hz, is shown in FIG. 5.7(a): here the correlation decays rapidly to a value close to zero in around 10 s. Note that $C(t)$ can be negative, but the negative values are small. Other methods to analyze image time series exist, one example is differential variance analysis reported in [53]. We find that this analysis results in characteristic times that

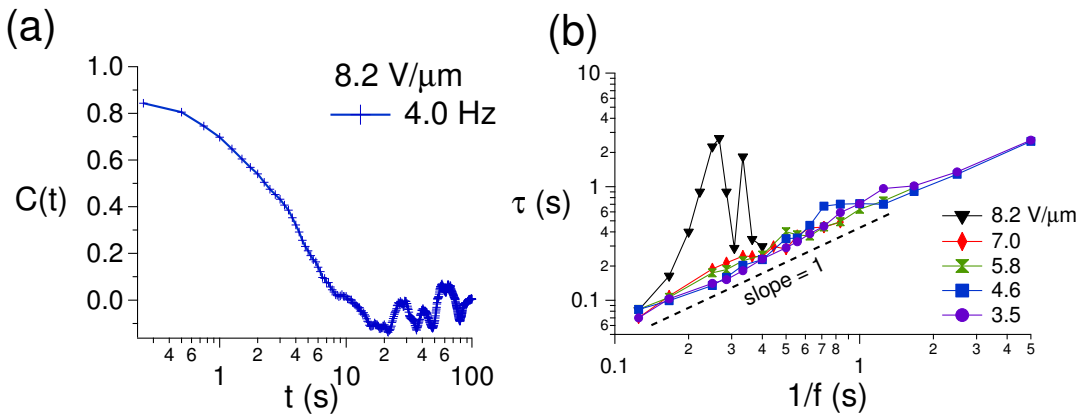

Figure 5.7: (a): The auto-correlation function, $C(t)$, at $E = 8.2$ V/μm and $f = 4$ Hz. $C(t)$ decays from 1 at $t = 0$ s to a value close to zero in roughly 10 s. (b): Identifying $C(t)$ with a dynamic order parameter, the characteristic time τ when $C(t)$ reaches a fraction 0.5 of its maximum value of 1, is plotted against $1/f$. The slope of 1 corresponds to $\tau = 1/f$, which is an intrinsic lower limit of measurable τ.

are comparable to those obtained using the above orientational correlation analysis (see FIG. 5.12 in Supplementary information, Section 5.9.1).

The decay of $C(t)$ shows no clear functional form (it is neither exponential nor a power law) but if one identifies $C(t)$ as a dynamic order parameter, there is a characteristic time $t = \tau$ when $C(t)$ reaches a fraction 0.5 of its maximum value of 1, and one can then plot τ versus $1/f$ (FIG. 5.7(b)).

The "universal" low curve for all fields (corresponding to a straight line with slope of 1, *i.e.*, $\tau \sim 1/f$) is an intrinsic limit: we cannot probe shorter times due to the stroboscopic imaging. For low τ (*i.e.* at high frequency or low $1/f$), the drops are essentially static. At each field amplitude, as the drop is driven more strongly by lowering frequency, the timescale increases (very significantly for $E = 8.2$ V/μm and less so for lower amplitudes) and then decreases again. As an example, at $E = 8.2$ V/μm, the peak in τ occurs at 0.25 s, correlating very well with the minimum in roundness in Figure 5.5(b). The subsequent decrease in τ at lower frequency,

corresponds with break up of the drop, and consequent decrease in electric Capillary number.

5.5.4 Long-time dynamics: Translational dynamics of drops

The translational dynamics of drops as a function of frequency and amplitude was studied by measuring the mean-squared displacement (MSD) of drop centroids. FIG. 5.8(a) shows the trajectory of each drop in a small region consisting of 7 drops over 600 s for four different frequencies, $0.2, 0.6, 1.0$, and 1.4 Hz at $E = 5.8$ V/μm. It is clear that the trajectories are most localized at 1.4 Hz and the least localized at 0.2 Hz. The mean-squared displacement (MSD) of the entire drop array, for the same frequencies and amplitude, is plotted in FIG. 5.8(b). Since we employ stroboscopic imaging, the minimum time we can probe (for $t > 0$) is $t = 1/f$. The maximum time probed (600 s) is much longer than the typical orientational decay times of interest, which are of order 10 s or less. We observe that for each frequency, the MSD increases linearly until it saturates. With increasing frequency, the saturation value of the MSD decreases. This is consistent with the localization of trajectories seen in FIG. 5.8(a).

For translational dynamics of charge-stabilized colloidal particles in a crystalline suspension, the individual particle dynamics is constrained by the harmonic interactions with its neighbors. In the colloidal study of Weiss *et al.* [49], this behavior has been analyzed as the combination of diffusive particle motion and harmonic (elastic) restoring force. In our system, a similar restoring force from the negative F_{DEP}, attracts the drops to the ITO-free regions. In the colloidal crystal, each colloidal particle diffuses with a diffusion coefficient, D, but is constrained by the potential of mean force.

In our droplet system, the diffusion of droplets is provided by hydrodynamic interactions, characterized by the fractional dynamics in the outer fluid shown in

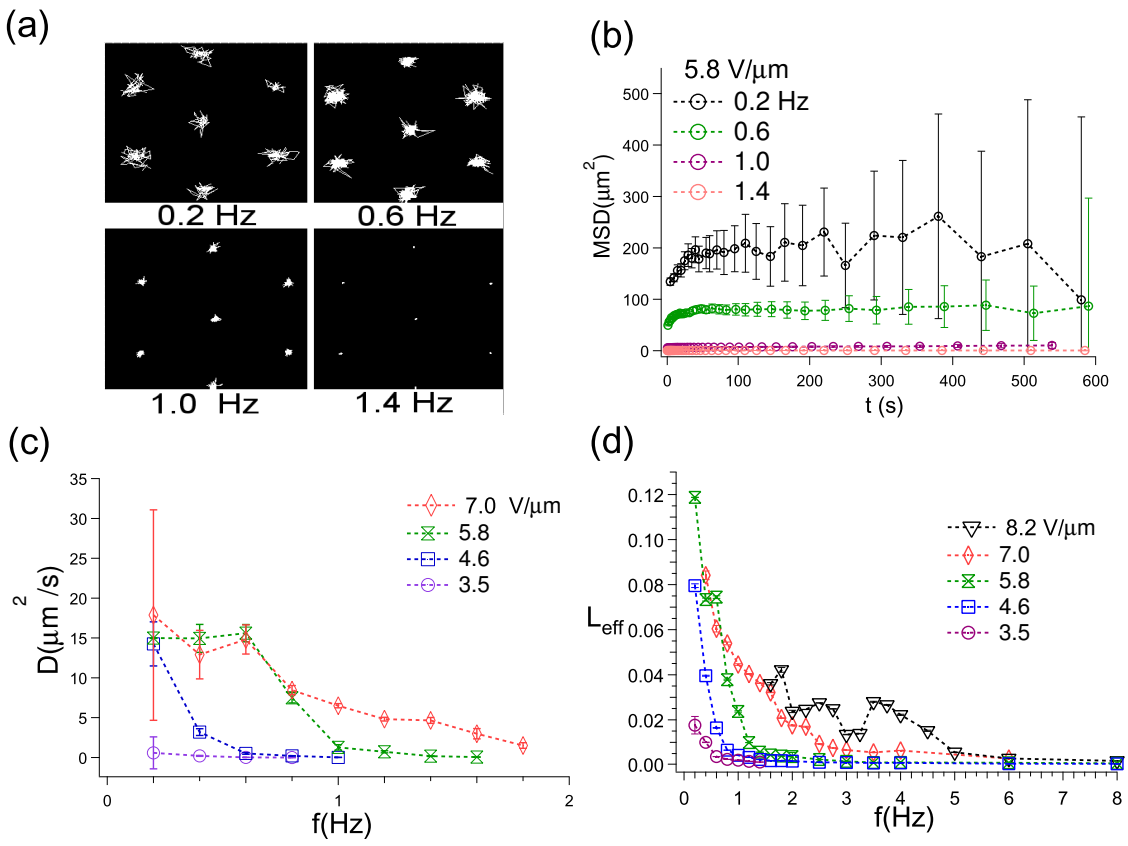

Figure 5.8: (a): Trajectories of droplets over 600 s ($E = 5.8$ V/μm). (b): Mean-squared displacement (MSD) of the droplets in (a). (c): Diffusion coefficient obtained for different field amplitudes and frequencies. (d): Effective Lindemann parameter, L_{eff}, for all frequencies and amplitudes. With increasing field amplitude, the transition from order to disorder occurs at higher frequencies.

FIG. 5.10, which tend to free the drops from their trapped potential. Decreasing the frequency increases the range of the hydrodynamic interactions, and thus enhances the effective-diffusive contribution. We can thus use the formalism represented by Equations (5.7), (5.8), and (5.9) to extract effective diffusion coefficients D and Lindemann parameter L_{eff} as we disorder the droplet lattice *via* EHD forces.

The diffusion coefficient, D versus frequency f for various field amplitudes, shown in FIG. 5.8(c), allows us to cross-check some assumptions. While the data for diffusion is limited at short times, we nevertheless can obtain reasonable data for $f < 2$ Hz

and at all field amplitudes except $E = 8.2$ V/μm, due to breakup events that have an onset at higher frequencies, which make the identification of the patterned drops difficult. There is a common plateau, for $E > 3.5$ V/μm, at around 15 μm$^2/s$. Given that the orientational correlations have a lifetime τ of between 0.1 and 10 s, this implies that the contribution of drop deformation to the centroid MSD is of order $D\tau \sim 1.5 - 150$ μm^2. As can be seen in FIG. 5.8(a), for all frequencies, except the lowest ones, the orientational and translational dynamics are not clearly separable in the mean-square displacements. Nevertheless, it will be shown that the dynamics and shape deformation analysis overlap in final phase diagram. The plateau diffusion coefficient of 15 μm^2/s (FIG. 5.8(c)) corresponds to a thermal system with an effective temperature $T_{\text{eff}} = 6\pi\mu_{ex}aD/k_B \sim 4 \times 10^8$ K.

The effective Lindemann parameter, L_{eff}, is shown in FIG. 5.8(d). With decreasing frequency, a transition from $L_{\text{eff}} \simeq 0$ to values greater than zero is seen at a characteristic frequency, f_c, for each field amplitude. f_c is plotted versus field amplitude in FIG. 5.11. The regime of strong hydrodynamics is expected to occur at higher frequencies with increasing field amplitudes, consistent with FIG. 5.8(d). Supplementary information, Section 5.9.2, Movie 5.2 shows the dynamics of a sub-region of a lattice of drops very close to the threshold of drop breakup. Two values of f_c when $L_{\text{eff}} \geq 0.01$ and 0.02 are considered for possible correspondence with the characteristic frequencies for non-circular deformation and breakup in FIG. 5.5(b), because all the L_{eff} are seen to increase in that range.

For comparison, Zahn and Maret [54] saw melting manifest itself as a second rise of the MSD (they refer to this as γ_L) above the plateau value beyond a critical value of an interaction strength. This critical plateau value of MSD is around $0.02 - 0.03 d_{nn}^2 \sim (0.15 d_{nn})^2$. The static Lindemann parameter (in units of d_{nn}) is generally of order 0.1 at the onset of melting in 2D [55, 56]. While this particular criterion for melting

is not valid in usual 2D melting because it diverges in the crystal as well, in the current study, *i.e.*, a crystal with an imposed lattice (and fluctuations suppressed), it is probably a reasonable disorder parameter.

It should be noted that our measurements contain a self-selection: only drops that remain trapped are included in either R or L_{eff}. Therefore, the measurements of the trapped-drop lattice are a very good representation of the entire system in the ordered state, but less so as one approaches the onset of melting. We observe that L_{eff} increases to a maximum value of about 0.08 for $E = 4.6$ V/μm and $E = 7.0$ V/μm, and to 0.12 for $E = 5.8$ V/μm. These increases occur in the frequency range $\sim 0.2 - 0.4$ Hz. Shown in Supplementary information, Section 5.9.2, Movie 5.3 is the dynamics at 0.2 Hz for $E = 4.6$ V/μm and $E = 5.8$ V/μm. For $E = 4.6$ V/μm ($Ca_E^0 \simeq 0.48$), there is no drop breakup, and the lattice is near the disorder threshold: further lowering the frequency would correspond most closely with the straightforward phenomenon of lattice melting. At the higher amplitude, most of the original drops have broken into tiny droplets, and the lattice is melted concurrently.

Next, we discuss the role of drop breakup at higher Ca_E^0. Breakup (FIG. 5.8(d)) already begins at the low value of $L_{\text{eff}} \approx 0.02$ for field amplitudes $E = 5.8$ V/μm ($Ca_E^0 \simeq 0.76$) and higher. Note that, this corresponds to frequencies $f \sim 1$ Hz, 2 Hz, and 4 Hz, respectively for $E = 5.8$ V/μm, 7 V/μm, and 8.2 V/μm, which is very close to the thresholds that can be identified with first breakup in the image panels in FIG. 5.4, and the threshold frequencies obtained in the roundness plot (FIG. 5.5(b)). Since we are only tracking the dynamics of the trapped drops, there are numerous unrecorded smaller droplets generated after breakup which are moving *much* faster. Shown in Supplementary information, Section 5.9.2, Movie 5.4 is the dynamics at 0.8 Hz and 1.6 Hz for $E = 7.0$ V/μm. At both frequencies, there is simultaneously an increase in drop breakup and drop translational motions.

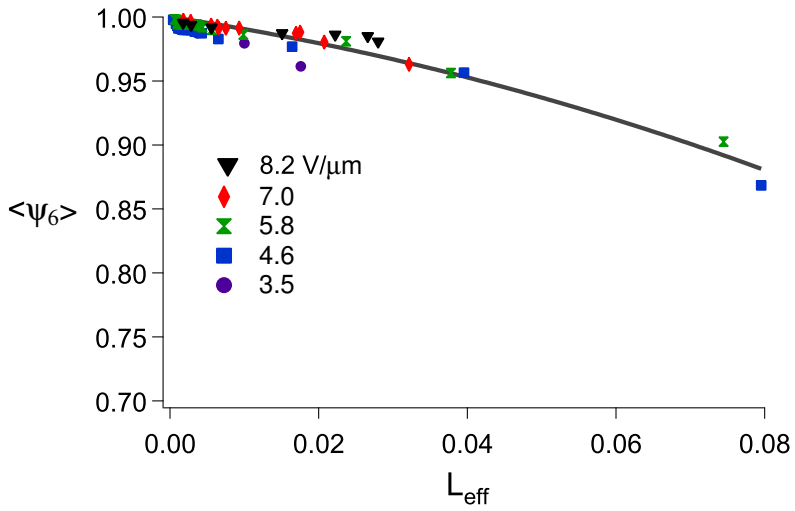

Figure 5.9: The average bond order parameter, $\langle\Psi_6\rangle$ correlates well with L_{eff}: $\langle\Psi_6\rangle$ is close to 1 where $L_{eff} \to 0$, and decreases monotonically with increasing L_{eff}; the solid line is a guide to the eye. Unlike $\langle\Psi_6\rangle$, however, L_{eff} can be obtained far into the disordered regime.

At higher driving, the system re-adjusts, *via* drop breakup, to lower Ca_E^0 by reducing the trapped drop size, and thus the system remains at the threshold of disorder without the lattice melting. Additionally, at $E = 8.2$ V/μm ($Ca_E^0 \simeq 1.5$), the circular-to-noncircular transition occurs without faceting (as seen in the right panel Supplementary information, Section 5.9.2, Movie 5.5 at 3.5 Hz), and the frequency threshold (4 Hz) is much closer to the crossover of 6 Hz, thus implying a mechanism of drop breakup that has a much stronger dipolar contribution.

A strong correlation between $\langle\Psi_6\rangle$ and L_{eff} is seen in FIG. 5.9. $\langle\Psi_6\rangle \simeq 1$ deviates from 1 to lower values as L_{eff} increases. While either parameter is useful in characterizing disorder, L_{eff} is practically easier to obtain from our image time series, as it depends on single-particle trajectories.

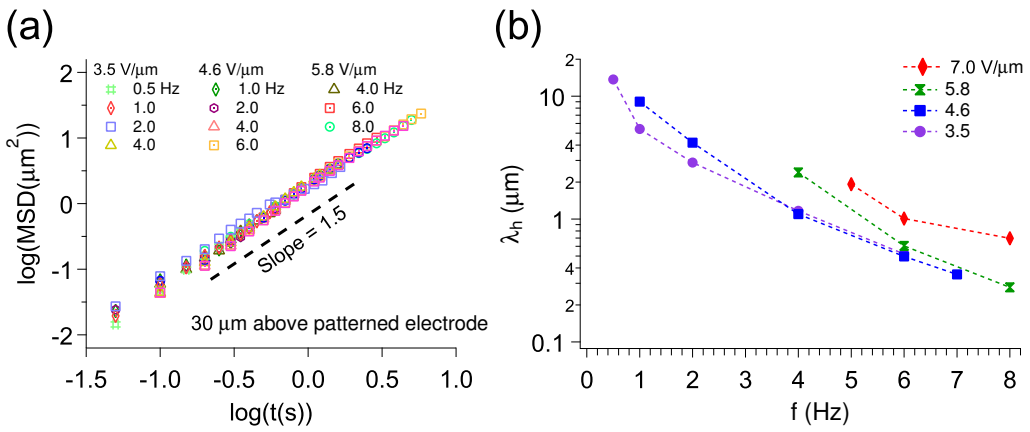

Figure 5.10: (a): Fractional tracer particle dynamics in the outer fluid is observed *via* linearity of a log (MSD) versus log (time) plot (the slope yields the power law γ). Data is obtained from an image time series obtained 30 μm above the bottom (patterned) electrode, *i.e.*, in the plane of the drop. γ is measured to be equal to 1.42 ± 0.17, showing enhanced super-diffusive dynamics consistent with a 3/2 power law that is independent of frequency and field amplitude.(b): From the prefactor K_γ we can construct an *experimental* hydrodynamic lengthscale $\lambda_h = \sqrt{K_\gamma / f^\gamma}$, which increases with decreasing frequencies.

5.5.5 Short-time dynamics: The underlying flow mechanism

Prior to the drop deformation experiments, non-stroboscopic experiments were carried out in emulsions with castor oil seeded with fluorescent PMMA tracer particles with diameter of ~ 1 μm. After an external AC electric field is imposed, the MSD of PMMA particles around the silicone oil drops was measured for various frequencies and amplitudes. The colloidal particles used are not ideal passive tracers, because a small fraction of these particles tend to adhere to drop interfaces. Thus, it is best to study drop dynamics without tracers; nevertheless, it is informative to first probe the fluid flow of the drops using tracer motions. One can write MSD $\propto t^\gamma$, where $\gamma = 1$ represents diffusive motion while $\gamma > 1$ represents super-diffusive (enhanced) motions. FIG. 5.10 shows log (MSD) versus log (time), at very short times, $0.05 < t < 10$ s, for the current system at 30 μm above the bottom electrode where $\gamma = 1.42 \pm 0.17$.

Super-diffusive motion with a $\frac{3}{2}$ power law has been observed before in active motor-driven motion inside cells [57] and ascribed to Brownian motion in the presence of random fluid velocity fields [58, 59] (alternatively termed fractional Brownian motion [60]). The $\gamma \sim 1.5$ power law for the super-diffusive dynamics of the carrier fluid at very short times, observed in Figure 5.10(a), is thus consistent with random velocity fields in the carrier fluid. These random flows would give random kicks to the large drops. Brownian motion in colloidal systems arises from random kicks from solvent molecules at much shorter timescales. The apparent Brownian motion of the drops at long times ($t \gg 1s$) and large spatial scales (drop diameter of 50 μm) also likely arises from the observed fractional dynamics at short ($0.05 < t < 10s$) times. We may write

$$\text{MSD} = K_\gamma t^\gamma. \tag{5.10}$$

Fitting the MSDs with $\gamma = 1.5$, we obtain K_γ, a generalized diffusion constant with units of $\text{m}^2/\text{s}^{1.5}$. Each $\log(\text{MSD})$ in FIG. 5.10 was shifted vertically by subtracting $\log(K_\gamma)$ and thus achieving collapse of all the data onto one master curve. We can plot $\lambda_h = \sqrt{K_\gamma / f^\gamma}$, which gives us a (frequency- and amplitude-dependent) lengthscale that is the experimental analog of the hydrodynamic lengthscale introduced in FIG. 5.2(a). The distances traveled by tracer particles in the outer fluid between successive images is a meaningful lengthscale flow between trapped drops for the stroboscopic imaging of drops employed in the remainder of this work. It should be noted that λ_h is difficult to measure under strong driving conditions, but $\lambda_h < l_h$ in all cases where it is measurable.

5.6 A non-equilibrium field–frequency phase diagram

The structural study of order to disorder in Section 5.5.2 found first a loss in circularity, and then a second characteristic frequency that we identified with the first incidence of drop breakup. The increase of f_c (corresponding to either drop deformation or breakup) with E is nonlinear and not fittable to a quadratic E^2 dependence that would be expected from a dipolar system. Indeed, the importance of hydrodynamic flows (i.e, interactions beyond dipolar) is seen clearly in the superdiffusive $t^{3/2}$ tracer particle motions in the outer fluid that is observed (FIG. 5.10) even when there is minimal drop deformation; e.g., at 8 Hz and $E = 5.8$ V/μm.

In FIG. 5.11, we see that these characteristic frequencies that we identified with a transition from circular to non-circular shape and for a transition into the drop breakup regime FIG. 5.5(b) correspond rather closely to those from translational dynamics FIG. 5.8(d) when $L_{\text{eff}} = 0.01$ and 0.02, respectively. This correspondence is only strictly valid at amplitudes of $E = 4.6$ V/μm and above; *i.e.*, $Ca_E^0 \simeq 0.5$. no breakup is seen for lower amplitudes.

On the other hand, L_{eff} continues to increase at low frequencies, and a higher L_{eff} near 0.08 likely corresponds to an approach to melting, given that the Lindemann criterion used in Gilvarry [55] is directly applicable to the 2D lattice in this study where fluctuations in the mean lattice position are suppressed by the dielectrophoretic trap. This also corresponds visually (see Supplementary information, Section 5.9.2, Movie 5.1) with the amplitude and the frequency where tiny droplets are leaving the pattern for $Ca_E = 0.75$ and higher. The solid black line between $f_c = 0.2$ and 0.45 Hz is close to the criterion for melting; this line is close to the drop deformation transition at the smaller field amplitudes, but is distinctly lower at higher E.

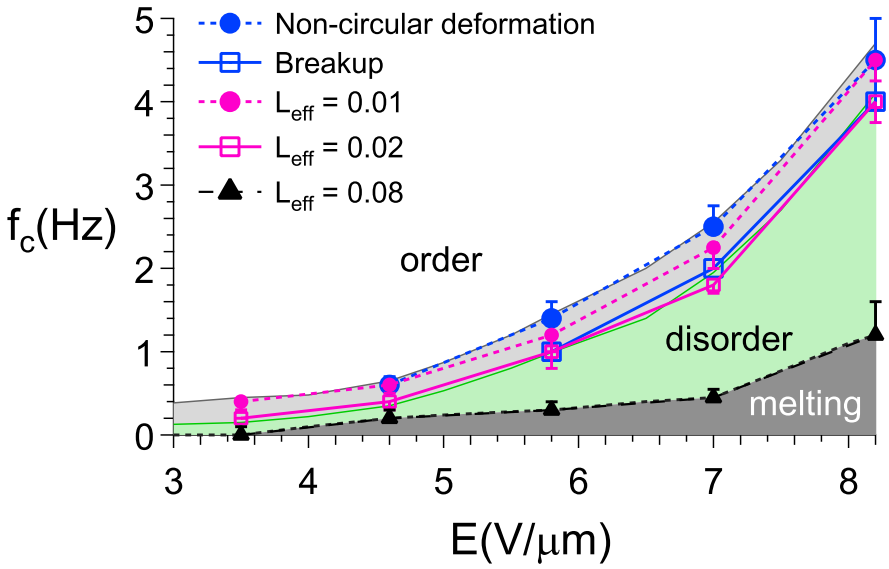

Figure 5.11: Characteristic frequencies obtained for a transition from circular to non-circular shape (blue filled circles) and for a transition into the drop breakup regime (blue open squares) correspond rather closely (at field amplitudes larger than $E = 4.6$ V/μm and $Ca_E^0 \geq 0.5$) with those from translational dynamics when $L_{\text{eff}} = 0.01$ (pink filled circles) and 0.02 (pink open squares) respectively. Higher L_{eff}, corresponding to the green region in (f_c, E) space, is the regime of disordering. Supplementary information, Section 5.9.2, Movie 5.2 shows dynamics along the threshold (light grey region in plot). The unshaded region above is the ordered regime. $L_{\text{eff}} \sim 0.08 - 0.12$ (dark grey region near bottom) corresponds to a classic criterion for melting [55].

In between, in the green region of the dynamic phase diagram (FIG. 5.11), the system remains self-organized with drop breakup decreasing Ca_E while keeping the system at the threshold to disorder. In both regimes of strong driving (the green region and the dark grey region at the bottom of the phase diagram), the system behaves like a thermal system with an effective temperature $T_{\text{eff}} \sim 10^8$K.

5.7 Conclusion

Far-from-equilibrium systems for studying two-dimensional disordering exist: examples are shaken granular media [27] and complex plasmas [61]. The advantage of the current system is that it is a simple driven, dissipative system with liquid-liquid interfaces where there are two continuously variable parameters with which to directly control the strength and range of hydrodynamic interactions. In addition, it is a real-space far-from-equilibrium system which affords the possibility of droplet trapping (*via* dielectrophoresis in this case), thus providing a great degree of control of droplet shape and kinetics.

We note the similarities and differences to a de-pinning transition [62]. In a typical de-pinning transition, there is a steady driving that drives the system from pinned to moving, often in coherence. In this system, the driving is not coherent, but is itself pseudo-random and thus mimics thermal motion; thus increasing the driving force resembles increasing the temperature. This is in contrast with a field-induced dipolar system, where increasing the driving force resembles a *decrease* in temperature.

How is fractional tracer dynamics consistent with the apparent Brownian motion of granular drops? The super-diffusive dynamics is at short times ($0.05 < t < 10$ s), and at longer times these pseudo-random flows result in giving the drops random kicks that can feasibly resemble Brownian motion at much longer times (seconds to minutes). All the drop dynamics and the emergent effective thermodynamics analyzed in this work thus likely arises from these underlying pseudo-random fluid flows in the outer fluid of the oil-in-oil emulsion.

In this system, we are able, at intermediate field amplitudes $Ca_E^0 \sim 0.5$ to approach a pure disordered state by lowering frequency f with no interference from drop breakup processes. At higher field amplitudes, $Ca_E^0 \geq 0.75$, drop breakup and disordering are concurrent processes as f decreases. Indeed, rather than disordering the

lattice with increased driving, tiny droplets break off from the large drop (decreasing its Ca_E), and the large-drop lattice restabilizes. Thus the system self-organizes to remain at the disorder threshold. This process goes on until the effective Lindemann parameter $L_{\text{eff}} \sim 0.08$ (dark grey regime at the bottom of the phase diagram), at which point the lattice melts.

5.8 Acknowledgments

We thank S. Ghosh for suggestions that led to this work. This research was supported by the National Science and Engineering Research Council of Canada (NSERC).

Bibliography

[1] A. Yethiraj. Tunable colloids: control of colloidal phase transitions with tunable interactions. *Soft Matter*, 3(9):1099–1115, 2007.

[2] D. G. Grier and C. A. Murray. The microscopic dynamics of freezing in supercooled colloidal fluids. *The Journal of Chemical Physics*, 100(12):9088–9095, 1994.

[3] W. K. Kegel and A. van Blaaderen. Direct observation of dynamical heterogeneities in colloidal hard-sphere suspensions. *Science*, 287(5451):290–293, 2000.

[4] E. R. Weeks, J. C. Crocker, A. C. Levitt, A. Schofield, and D. A. Weitz. Three-dimensional direct imaging of structural relaxation near the colloidal Glass transition. *Science*, 287(5453):627–631, 2000.

[5] U. Gasser, E. R. Weeks, A. Schofield, P. N. Pusey, and D. A. Weitz. Real-space imaging of nucleation and growth in colloidal crystallization. *Science*, 292(5515):258–262, 2001.

[6] A. Yethiraj and A. van Blaaderen. A colloidal model system with an interaction tunable from hard sphere to soft and dipolar. *Nature*, 421(6922):513–7, 2003.

[7] D. Strickland, Y. Lin, E. Wagner, C. M. Hope, J. Zayner, Chloe Antoniou, Tobin R. Sosnick, Eric L. Weiss, and Michael Glotzer. TULIPs: tunable, light-controlled interacting protein tags for cell biology. *Nature Methods*, 9(4):379–384, 2012.

[8] T. E. Kodger, R. E. Guerra, and J. Sprakel. Precise colloids with tunable interactions for confocal microscopy. *Scientific Reports*, 5:14635, 2015.

[9] P. S. Mohanty, P. Bagheri, S. Nöjd, A. Yethiraj, and P. Schurtenberger. Multiple path-dependent routes for phase-transition kinetics in thermoresponsive and field-responsive ultrasoft colloids. *Physical Review X*, 5(1):011030, 2015.

[10] Y. Yang, L. Fu, C. Marcoux, J. E. S. Socolar, P. Charbonneau, and B. B. Yellen. Phase transformations in binary colloidal monolayers. *Soft Matter*, 11(12):2404–2415, 2015.

[11] M. Pichumani, P. Bagheri, K. M. Poduska, W. González-Viñas, and A. Yethiraj. Dynamics, crystallization and structures in colloid spin coating. *Soft Matter*, 9(12):3220, 2013.

[12] J. Dobnikar, A. Snezhko, and A. Yethiraj. Emergent colloidal dynamics in electromagnetic fields. *Soft Matter*, 9(14):3693–3704, 2013.

[13] L. Addadi, S. Raz, and S. Weiner. Taking advantage of disorder: amorphous calcium carbonate and Its roles in biomineralization. *Advanced Materials*, 15(12):959–970, 2003.

[14] P. Vukusic, B. Hallam, and J. Noyes. Brilliant whiteness in ultrathin beetle scales. *Science*, 315(5810):348–348, 2007.

[15] M. Adams, Z. Dogic, S. L. Keller, and S. Fraden. Entropically driven microphase transitions in mixtures of colloidal rods and spheres. *Nature*, 393(6683):349–352, 1998.

[16] F. M. van der Kooij, K. Kassapidou, and H. N. W. Lekkerkerker. Liquid crystal phase transitions in suspensions of polydisperse plate-like particles. *Nature*, 406(6798):868–871, 2000.

[17] A. van Blaaderen. Materials science: Colloids get complex. *Nature*, 439(7076):545–546, 2006.

[18] H. Senff and W. Richtering. Temperature sensitive microgel suspensions: Colloidal phase behavior and rheology of soft spheres. *The Journal of Chemical Physics*, 111(4):1705–1711, 1999.

[19] D. Paloli, P. S. Mohanty, J. J. Crassous, E. Zaccarelli, and P. Schurtenberger. Fluid–solid transitions in soft-repulsive colloids. *Soft Matter*, 9(11):3000, 2013.

[20] U. Dassanayake, S. Fraden, and A. van Blaaderen. Structure of electrorheological fluids. *Journal of Chemical Physics*, 112:3851, 2000.

[21] S. Jiang, Q. Chen, M. Tripathy, E. Luijten, K. S. Schweizer, and S. Granick. Janus particle synthesis and assembly. *Advanced Materials*, 22(10):1060–1071, 2010.

[22] E. Bianchi, R. Blaak, and C. N. Likos. Patchy colloids: state of the art and perspectives. *Physical Chemistry Chemical Physics*, 13(14):6397, 2011.

[23] C. P. Brangwynne, P. Tompa, and R. V. Pappu. Polymer physics of intracellular phase transitions. *Nature Physics*, 11(11):899–904, 2015.

[24] A. A. Hyman and K. Simons. Beyond oil and water-phase transitions in cells. *Science*, 337(6098):1047–1049, 2012.

[25] A. Morin, N. Desreumaux, J. Caussin, and D. Bartolo. Distortion and destruction of colloidal flocks in disordered environments. *Nature Physics*, 13(1):63–67, 2017.

[26] C. J. Reichhardt and C. Reichhardt. Collective motion: Disorder in the wild. *Nature Physics*, 13(1):10–11, 2017.

[27] R. P. Behringer, K. E. Daniels, T. S. Majmudar, and M. Sperl. Fluctuations, correlations and transitions in granular materials: statistical mechanics for a non-conventional system. *Philosophical Transactions of the Royal Society of London A: Mathematical, Physical and Engineering Sciences*, 366(1865):493–504, 2008.

[28] M. P. Ciamarra, P. Richard, M. Schröter, and B. P. Tighe. Statistical mechanics for static granular media: open questions. *Soft Matter*, 8(38):9731–9737, 2012.

[29] D. W. Howell, R. P. Behringer, and C. T. Veje. Fluctuations in granular media. *Chaos: An Interdisciplinary Journal of Nonlinear Science*, 9(3):559–572, 1999.

[30] A. A. Hyman, C. A. Weber, and F. Jülicher. Liquid-liquid phase separation in biology. *Annual Review of Cell and Developmental Biology*, 30(1):39–58, 2014.

[31] A. Varshney, S. Ghosh, S. Bhattacharya, and A. Yethiraj. Self organization of exotic oil-in-oil phases driven by tunable electrohydrodynamics. *Scientific Reports*, 2:738, 2012.

[32] A. Varshney, S. Gohil, M. Sathe, S. Rao RV, J. B. Joshi, S. Bhattacharya, A. Yethiraj, and S. Ghosh. Multiscale flow in an electro-hydrodynamically driven oil-in-oil emulsion. *Soft Matter*, 12(6):1759–1764, 2016.

[33] S. Khajehpour Tadavani, J. R. Munroe, and A. Yethiraj. The effect of confinement on the electrohydrodynamic behavior of droplets in a microfluidic oil-in-oil emulsion. *Soft Matter*, 12(45):9246–9255, 2016.

[34] A. Varshney, S. Gohil, S. Khajehpour Tadavani, A. Yethiraj, S. Bhattacharya, and S. Ghosh. Large scale arrays of tunable microlenses. *Soft Matter*, 14(7):1330–1335, 2014.

[35] M. Trau, S. Sankaran, D. A. Saville, and I. A. Aksay. Pattern formation in nonaqueous colloidal dispersions via electrohydrodynamic flow. *Langmuir*, 11(12):4665–4672, 1995.

[36] N. Wu and W. B. Russel. Micro- and nano-patterns created via electrohydrodynamic instabilities. *Nano Today*, 4(2):180–192, 2009.

[37] P. G. Oppenheimer. *Electrohydrodynamic patterning of functional materials*. Springer Theses. Springer International Publishing, Heidelberg, 2013.

[38] H. Tian, C. Wang, J. Shao, Y. Ding, and X. Li. Electrohydrodynamic pressure enhanced by free space charge for electrically induced structure formation with high aspect ratio. *Langmuir*, 30(42):12654–12663, 2014.

[39] J. C. Crocker and D. G. Grier. Methods of digital video microscopy for colloidal studies. *Journal of Colloid And Interface Science*, 179(1):298–310, 1996.

[40] G. I. Taylor. Studies in Eeectrohydrodynamics. I. The circulation produced in a drop by electrical field. *Proceedings of the Royal Society of London. Series A, Mathematical and Physical Sciences*, 291(1425):159–166, 1966.

[41] J. R. Melcher and G. I. Taylor. Electrohydrodynamics: a review of the role of interfacial shear stresses. *Annual Review of Fluid Mechanics*, 1(1):111–146, 1969.

[42] S. Torza, R. G. Cox, and S. G. Mason. Electrohydrodynamic deformation and burst of liquid drops. *Philosophical Transactions of the Royal Society of London. Series A, Mathematical and Physical Sciences*, 269(1198):295–319, 1971.

[43] E. K. Zholkovskij, J. H. Masliyah, and J. Czarnecki. An electrokinetic model of drop deformation in an electric field. *Journal of Fluid Mechanics*, 472:1–27, 2002.

[44] J. Q. Feng. Electrohydrodynamic behaviour of a drop subjected to a steady uniform electric field at finite electric Reynolds number. *Proceedings: Mathematical, Physical and Engineering Sciences*, 455(1986):2245–2269, 1999.

[45] J. Bockris. *Modern electrochemistry*. Plenum Press, New York, 2nd ed.. edition, 1998.

[46] C. A. Murray. *Bond-orientational order in condensed matter systems*. Springer-Verlag, New York, 1992.

[47] A. Yethiraj, A. Wouterse, B. Groh, and A. van Blaaderen. Nature of an electric-field-induced colloidal martensitic transition. *Physical Review Letters*, 92(5):058301, 2004.

[48] P. Bagheri, A. M. Almudallal, A. Yethiraj, and K. M. Poduska. Quantitative metrics for assessing positional and orientational order in colloidal crystals. *Langmuir*, 31(30):8251–9, 2015.

[49] J. A. Weiss, A. E. Larsen, and D. G. Grier. Interactions, dynamics, and elasticity in charge-stabilized colloidal crystals. *The Journal of Chemical Physics*, 109(19):8659–8666, 1998.

[50] G. Volpe and G. Volpe. Simulation of a Brownian particle in an optical trap. *American Journal of Physics*, 81(3):224, 2013.

[51] K. Berg-Sørensen and H. Flyvbjerg. Power spectrum analysis for optical tweezers. *Review of Scientific Instruments*, 75(3):594–612, 2004.

[52] A. M. Alsayed, M. F. Islam, J. Zhang, P. J. Collings, and A. G. Yodh. Premelting at defects within bulk colloidal crystals. *Science (New York, N.Y.)*, 309(5738):1207–10, 2005.

[53] R. Pastore, G. Pesce, and M. Caggioni. Differential variance analysis: a direct method to quantify and visualize dynamic heterogeneities. *Scientific Reports*, 7(0):1–9, 2017.

[54] K. Zahn and G. Maret. Dynamic criteria for melting in two dimensions. *Physical Review Letters*, 85(17):3656–3659, 2000.

[55] J. J. Gilvarry. The Lindemann and Grüneisen laws. *Physical Review*, 102(2):308–316, 1956.

[56] P. Dillmann, G. Maret, and P. Keim. Comparison of 2d melting criteria in a colloidal system. *Journal of Physics: Condensed Matter*, 24(46):11, 2012.

[57] A. Caspi, R. Granek, and M. Elbaum. Enhanced diffusion in active intracellular transport. *Physical Review Letters*, 85(26):5655–5658, 2000.

[58] A. Ajdari. Transport by active filaments. *Europhysics Letters*, 31(2):69, 1995.

[59] G. Zumofen, J. Klafter, and A. Blumen. Enhanced diffusion in random velocity fields. *Physical Review A*, 42(8):4601–4608, 1990.

[60] R. Metzler and J. Klafter. The restaurant at the end of the random walk: recent developments in the description of anomalous transport by fractional dynamics. *Journal of Physics A: Mathematical and General*, 37(31):R161–R208, 2004.

[61] A. V. Ivlev, M. H. Thoma, C. Rath, G. Joyce, and G. E. Morfill. Complex plasmas in external fields: The role of non-hamiltonian interactions. *Physical Review Letters*, 106:155001, 2011.

[62] C. Reichhardt and C. J. Olson Reichhardt. Depinning and nonequilibrium dynamic phases of particle assemblies driven over random and ordered substrates: a review. *Reports on Progress in Physics*, 80(2):026501, 2017.

5.9 Supplementary information

Movies 5.1 to 5.5 can be found in a CD attached to this thesis.

5.9.1 Intensity variance analysis

Following the work of Pastore *et al.* [53], we examine the time dependence of the variance of intensity fluctuations, $V = I(t + \Delta t) - I(t)$, plotted for times from the minimum time of 0.25 s (due to the stroboscopic imaging) to 100 s in FIG. 5.12(a). V reaches to a plateau of approximately 200 (in units of pixel gray levels squared) in roughly $10 - 20$ s. $1 - \frac{V}{V_\infty}$, where V_∞ is the average of fluctuations at the plateau, is plotted versus time in FIG. 5.12(b). This time dependence yields a characteristic time that is roughly comparable to that obtained from the orientational correlations (FIG. 5.7(a) of the manuscript).

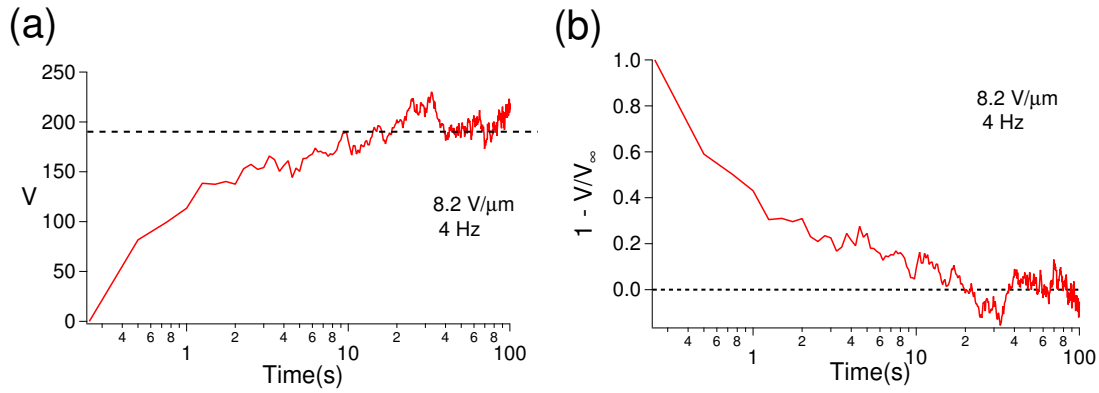

Figure 5.12: (a): Variance of intesity, V, for the same field and frequency as FIG. 5.7(a). After roughly $10 - 20$ s V reaches to a plateau of approximately 200. (b): $1 - \frac{V}{V_\infty}$, where V_∞ is the average of fluctuations at plateau. This characteristic time is comparable to the time required to lose orientational correlations (FIG. 5.7(a) of the manuscript).

5.9.2 Supplementary movies

Supplementary Movie 5.1: **Phase diagram** A small portion of entire field of view for each frequency and each amplitude is selected. Left to right corresponds to low to high amplitudes. A transition from disorder to order is seen by increasing frequency. Scale bar is 50 μm and fields are perpendicular to the page.

Supplementary Movie 5.2: **Dynamics at the disorder border.** Five panels, from left to right, show all fields from low to high amplitudes at the threshold line corresponds to order to disorder transition, light grey region in FIG. 5.11 of manuscript. Drops stay circular with lowering frequency at the lowest field amplitude, $E = 3.5$ V/μm. The non-circular deformations are accompanied with breakup events at higher fields, $E = 5.8, 7.0$ and 8.2 V/μm. Scale bar is 50 μm and fields are perpendicular to the page.

Supplementary Movie 5.3: **Dynamics at two intermediate fields and lowest frequency.** Left to right: At $f = 0.2$ Hz, the dynamics for two intermediate fields $E = 4.6$, and 5.8 V/μm is shown. The major breakup events, faster dynamics, and drops-free patterned spots are the major differences between the left and the right panels. Scale bar is 50 μm and fields are perpendicular to the page.

Supplementary Movie 5.4: **Effect of lowering frequency in the disordered regime.** From left to right: Dynamics of drops at $E = 7.0$ V/μm and 0.8 and 1.6 Hz, both located on the green zone of disorder. Lowering frequency increases drop breakup, while the smaller drops are still stabilized and localized on the patterned ITO-free regions. Scale bar is 50 μm and field is perpendicular to the page.

Supplementary Movie 5.5: **Effect of lowering frequency in the disordered regime.** From left to right: Dynamics of drops at $E = 8.2$ V/μm and 1.8 and 3.5 Hz, both located on the green zone of disorder. Smaller, stabilized patterned drops are as a results of decreasing frequency in the left panel. The non-circular deformation,

orientational deformation, is shown in the right panel. Scale bar is 50 μm and field is perpendicular to the page.

Chapter 6

Anomalous dynamics in tracer-particle motions in an electrohydrodynamically driven oil-in-oil system

Synopsis: S. Khajehpour Tadavani carried out the experiments and analysis and wrote the initial draft of the manuscript and implemented subsequent revisions. A. Yethiraj provided comments on the drafts and contributed to the final text of the manuscript. This chapter is submitted to Physical Review E (American Physical Society Publishing Group) and it can be found at arXiv:1805.03242, 2018.

6.1 Abstract

We characterize the super-diffusive dynamics of tracer particles in an electrohydrodynamically driven emulsion of oil droplets in an immiscible oil medium, where the amplitude and frequency of an external electric field are the control parameters. In the weakly-driven electrohydrodynamic regime, the droplets are trapped dielectrophoretically on a patterned electrode, and the driving is therefore spatially varying. We find excellent agreement with a $\langle x^2 \rangle \sim t^{1.5}$ power law, and find that this superdiffusive dynamics arises from an underlying displacement distribution that is distinctly non-Gaussian, and exponential for small displacements and short times. While these results are comparable with a random-velocity field model, the tracer particle speeds are in fact spatially varying in 2 dimensions, arising from a spatially varying electrohydrodynamic driving force. This suggests that the important ingredient for the super-diffusive $t^{1.5}$ behavior observed is a velocity field that is isotropic in the plane and spatially correlated. Finally, we can extract, from the superdiffusive dynamics, an experimental lengthscale that corresponds to the lateral range of the hydrodynamic flows. This experimental length scale is only non-zero above a threshold ion mobility length.

6.2 Introduction

Diffusion is characterized by a mean-squared displacement that increases linearly with time: in 1 dimension, $\langle x^2 \rangle = 2Dt$, and the underlying distribution of displacements is Gaussian. However, in many systems in colloid science and biology, it has been recognized that a relation of the form $\langle x^2 \rangle \sim t^{\gamma}$ holds, with $\gamma \neq 1$. This is often termed as anomalous transport. Apart from simple ballistic motion (corresponding to $\gamma = 2$), there are two categories of observed anomalous motion: sub-diffusive

$(0 < \gamma < 1)$ and super-diffusive $(\gamma > 1)$.

Anomalous transport that is sub-diffusive or super-diffusive can be observed in biological cells [1–4]. The essential ingredients that generate anomalous motions are macromolecular crowding (which can restrict motions) and active driving (which can enhance motions). Sub-diffusive motions have been extensively studied in the context of macromolecular crowding [3, 5, 6].

Enhanced, superdiffusive dynamics, while less common, is particularly relevant to (active or driven) systems out of equilibrium. A number of theoretical studies have found reasons for super-diffusive behavior. Ajdari [7] considered a model where particles diffuse until they are reversibly adsorbed onto active filaments which propel them. Bouchaud *et al.* [8], Zumofen *et al.* [9] and Redner [10] found superdiffusive motions arises when there are random, but spatially correlated velocity fields. These motions, in the context of the random velocity model, arise from a probability distribution of the form $P(x,t) \sim t^{-3/4} e^{-\left(x/t^{3/4}\right)^{\delta}}$, where $\gamma = 1.5$, but δ is not known. In a numerical study of Lévy random walks [11], which describe non-diffusive transport that is characterized by a coupling between free-path length and free-path duration, Trotta *et al.* found superdiffusive transport with $\gamma \simeq 1.47$; the probability distribution function is a modified Gaussian for short displacements but a power law for large displacements.

Following tracer-particle motions inside an eukaryotic cell, Caspi and coworkers [12, 13] found enhanced diffusion, likely arising from microtubule-associated motor-driven motions rather than thermal motions, with an exponent $\gamma \sim 1.5$. Ott *et al.* [14] also found enhanced diffusion in a system of polymerlike micelles, where the enhancement could be killed by decreasing the breaking time of the micelle by increasing temperature. Gal *et al.* observe enhanced motions in polymer particles that are imbibed into living cancer cells [15], while Reverey *et al.* [16] see superdiffusion in intra-cellular motion in highly crowded cytoplasm.

Transitions from sub- to super-diffusive are seen in systems where the forcing exceeds a threshold that overcomes pinning on a surface [17]. Various groups have also reported on Brownian diffusion that can co-exist with a non-Gaussian probability distribution of displacements [18–23], which possibly arise from competing effects at short and long times. Quite generally, this area of research is very active, and there is a call [1] for well-defined model systems that exhibit anomalous motions and, at the same time allow single-particle tracking of tracer-particle dynamics.

The focus of this study is tracer-particle motions in an oil-in-oil system driven by electrohydrodynamic driving forces. It has been shown previously [24, 25] that one sees both steady circulations as well as unsteady motions as a function of the driving electric field, with the unsteady motions dominating at high amplitudes leading to chaotic motions and multi-scale (seemingly turbulent) flows. In this work, we trap the oil droplets on a dielectrophoretic lattice, generating a spatially varying but periodic driving force. Given the high degree of control, the length scales on the tens of micrometers, and the presence of soft liquid-liquid interfaces, this system might be a clean and well-characterizable analog for out-of-equilibrium biological systems.

6.3 Methods and techniques

6.3.1 Sample preparation and hardware

FIG. 6.1(a) shows the side view of a sample cell with the electric field parallel to the page and to gravity. Two cover glass slides coated with indium tin oxide, ITO, are separated by glass spacers. The distance between the ITO slides is $h = 140$ μm. The bottom electrode is selectively etched out, using maskless patterning and photolithography, in the form of a hexagonal array of circular ITO-free regions, such that the diameter of each circle is approximately 50 μm and the nearest-neighbor center-to-

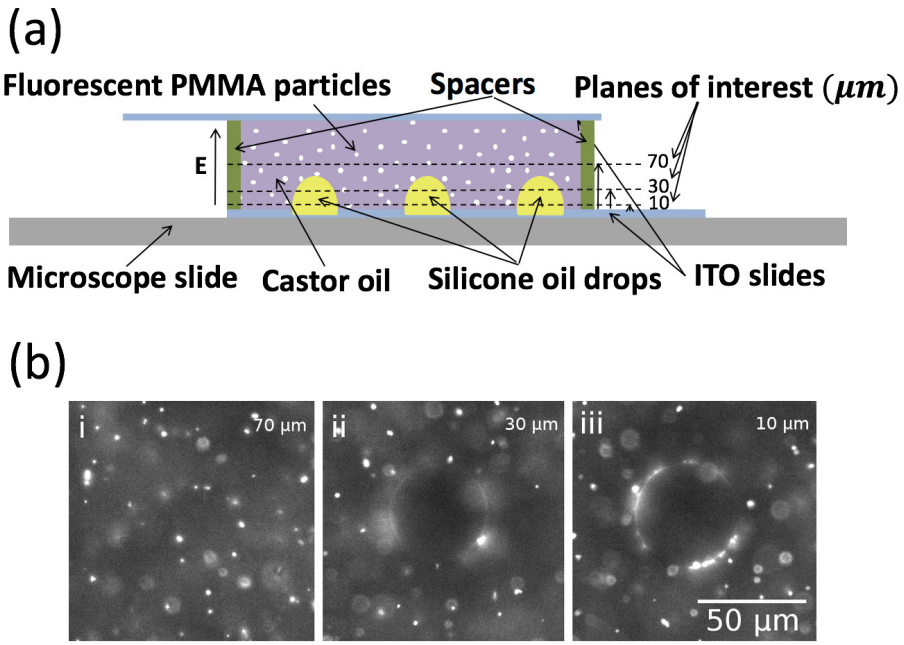

Figure 6.1: (a): A Side view of the cell geometry. Three dash lines indicate three planes at which the experiment is conducted. The top plate is an unpatterned ITO electrode. The bottom electrode is patterned with circular ITO-free regions. Silicone oil is dielectrophoretically trapped in the ITO-free regions and assumed the form of near-hemispherical drops (shown in yellow). The continuous phase is castor oil, seeded with fluorescent PMMA particles (represented by white dots). (b): Snapshots of three planes of interest at (i) $h_p = 70$, (ii) 30, and (iii) 10 μm above the patterned (bottom) electrode at $E = 4.6$ V/μm, perpendicular to the page, and $f = 1$ Hz. The PMMA particles are the bright spots in each frame. Accumulation of PMMA particles at the interface of silicone oil drop and castor oil leads to a bright edge.

center spacing, d_{nn}, is approximately 100 μm [25]. Ultraviolet-curable epoxy, Norland Optical Adhesive 61 and 68 are used to hold all parts together.

The cell is filled by pipetting an emulsion of silicone oil, dielectric constant $\varepsilon_{in}/\varepsilon_0 = 2.4$, conductivity $\sigma_{in} = 3.95 \times 10^{-11}$ S/m, and viscosity $\mu_{in} = 0.137$ Pa $\cdot$ s, and castor oil, dielectric constant $\varepsilon_{ex}/\varepsilon_0 = 3.6$, conductivity $\sigma_{ex} = 4.0 \times 10^{-10}$ S/m, and viscosity $\mu_{ex} = 0.819$ Pa $\cdot$ s, in a volume ratio of 1 : 16. The subscripts in and ex are used to represent the (silicone oil) droplet and the (castor oil) suspending carrier fluid, respectively. Fluorescent PMMA particles with diameter of 1 μm are added to

the carrier fluid, castor oil, in order to track the fluid flow.

The silicone oil drops are prepared, prior to recording the experiment, so that they are trapped at the ITO-free regions due to the negative dielectrophoretic force [25]. The experiment is carried out at four field amplitudes 3.5, 4.6, 5.8, and 7.0 V/μm and for different sets of frequencies. These fields and frequencies are chosen with reference to the field-frequency phase diagram discovered in previous work, Chapter 5 FIG. 5.11 [25], and all correspond to a region of parameter space that was identified as the "ordered regime" where the electrohydrodynamic flows are not strong enough to disrupt the hexagonal order of the trapped drops. Given that fluid flows in a leaky dielectric are governed by the boundary conditions at the interfaces, controlling the location of the interfaces enables us to follow tracer particle flows in the carrier fluid in a well-defined geometry. The experiment at each frequency and field amplitude is done at three different heights of sample cell, 10, 30, and 70μm above the patterned electrode, as shown by planes of interest in FIG. 6.1(a). FIG. 6.1(b) shows a silicone oil drop surrounded by PMMA particles in castor oil and at three heights of interest.

A sinusoidal AC voltage, provided by Tektronix model $AFG3022$ function generator, is amplified by a high voltage amplifier, Trek model $PZD2000A$, whose output is applied the sample cell. Fluorescence microscopy is used to observe and record the image sequences.

6.3.2 Image processing

For each experiment, a stack of 400 images, each with an exposure time of 4 ms, was recorded with a water-cooled digital sCMOS camera (pco.edge 5.5) and an inverted microscope, Nikon Eclipse TE2000-U. The centroid, $\vec{r'} = (x', y')$, of each PMMA particle is first identified in each image.

The particle trajectory is then obtained by standard particle tracking methods

described by Crocker and Grier [26, 27] using code programmed in IDL. Using the particle tracking information one can obtain the mean-squared displacement in 2 dimensions, $MSD = \langle r^2(t) \rangle \equiv \langle (r'(t) - r'(t_0))^2 \rangle$. $\vec{r}(t) = (x(t), y(t))$ (where $x(t) \equiv x'(t') - x'(t'_0)$ and $y(t) \equiv y'(t') - y'(t'_0)$ respectively) is the in-plane displacement of each particle as a function of time $t = t' - t'_0$, from a variable reference start time t'_0. In the above, $\langle \cdot \rangle$ is an average over all the particles in the system, and also over the reference time. We are unable to access out-of-plane motions in real time, but we obtain the same 2D information at 3 depths in the sample.

The histogram of displacements, $P(x,t)$ of all particles is calculated for a stack of 400 frames and for all field amplitudes, frequencies, and heights. The same was done for $P(y,t)$.

6.3.3 Pattern formation and flow visualization

Prior to recording the experiments, the system (*i.e.*, the droplet array) was prepared as follows. The electric field was set to $E = 7.0$ V/μm and $f = 0.05$ Hz. At very low frequency, in the regime of strong hydrodynamics where the hydrodynamic length, l_h, is on the order of hundreds of micrometers [25], large silicone oil drops are broken into many tiny droplets vigorously. The spontaneous breakup of droplets is a result of overcoming the viscous stresses by electric stresses at the interface of the droplets [24, 28–30]. The strong inhomogeneous flows, with breakup accompanied by coalescence, can be achieved by either lowering the frequency or increasing the field amplitude. At a fixed field amplitude, the frequency is increased to $f = 3$ Hz. Increasing the frequency decreases the strength of the electrohydrodynamic flows, but does not change significantly the dipolar contribution. The silicone oil drops coalesce, and are attracted to the nearest ITO-free regions by negative dielectrophoresis and an array of hexagonal silicone oil droplets, in castor oil, is created on the top of patterned

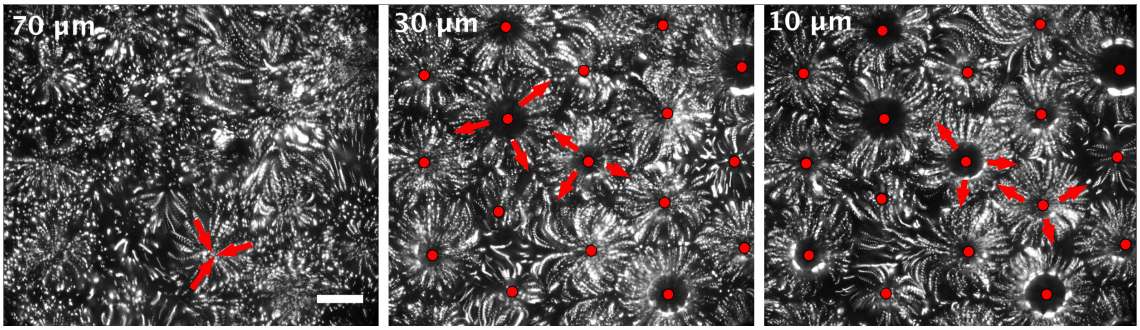

Figure 6.2: A timelapse series of 5 s for three heights of interest, from left to right $h_p = 70$, 30, and 10 μm. Flows tracked by fluorescent PMMA particles are indicated by trails in direction of arrows from sources to sinks. For $h_p = 70$ μm sources are at $d_{nn}/2 \simeq 50$ μm and sinks are at center of the drops. For $h_p = 30$ and 10 μm sources and sinks are located at edge of the drops and $d_{nn}/2 \simeq 50$ μm, respectively, indication an oblate drop deformation. Red circles show position of center of drops in the lower heights. $E = 5.8$ V/μm, perpendicular to the page, $f = 3$ Hz, and scalebar is 50 μm.

ITO slide [31].

All experiments are carried out at frequencies where the drops are always trapped on ITO-free regions. In steady state, toroidal flows known as Taylor vortices [32, 33] are generated inside and outside of each droplet. In the context of the leaky dielectric model [32, 33], these flows are generated by the tangential component of the electric stress at the interface of silicone oil drops and the surrounding castor oil medium; these are flows that arise from the accumulation of free charge carriers at these liquid-liquid interfaces. The PMMA fluorescent particles were used as tracer particles in order to visualize the outside flows: studying the nature of these flows is the main focus of this work.

FIG. 6.2 shows a timelapse of 100 frames, equivalent to 5 s, of PMMA particles motion at three heights of interest. At 70 μm above the patterned electrode (left panel), which is roughly 20 μm above the top of the silicone oil drops, particle trajectories in the plane are less clear than for the lower heights which are chosen to contain the silicone oil drops. Due to differences in the size of droplets, the flow pattern looks

disordered and asymmetric. At lower distances from the patterned electrode, 30 and 10 μm, middle and right panels, respectively, the flows are clearly initiated at the interface of silicone oil and castor oil. At steady state and for most of frequencies studied in this work, drops are oblate semi-ellipsoids with major axis perpendicular to the direction of the external electric field and the circulation patterns are generated from equator to the poles [32, 33], as shown in FIG. 6.2. Supplemental material, Section 6.8.2.1, Movie 6.1 shows an example of PMMA tracer-particle motions around a silicone oil drop at three planes, corresponding to three heights h_p, with particles at each height distinguished *via* false color as red, green and blue.

6.4 Background and theory

The mean-squared displacement or the second moment of a Gaussian distribution, in one dimension, is defined by

$$\left\langle \left(x\left(t\right)\right)^2 \right\rangle = \int_{-\infty}^{\infty} x^2 P_G\left(x,t\right) dx = 2Dt, \tag{6.1}$$

where

$$P_G\left(x,t\right) = \frac{1}{\sqrt{4\pi Dt}} \exp\left(\frac{-x^2}{4Dt}\right). \tag{6.2}$$

$P_G\left(x,t\right)$, D, and t represent the Gaussian probability distribution of displacements x, diffusion coefficient with dimension $[D] = \mathrm{m^2 s^{-1}}$, and time, respectively [18, 34]. The Gaussian-diffusive trajectories are characterized by irregular, but small and homogeneous steps.

Diffusion processes in many complex systems do not follow Gaussian statistics and the mean-squared displacement (MSD) does not vary linearly in time: this is

expressed (in d dimensions) by

$$MSD = 2dK_\gamma t^\gamma, \tag{6.3}$$

where K_γ is a generalized diffusion constant with dimension $[K_\gamma] = \mathrm{m}^2\mathrm{s}^{-\gamma}$ and γ is the anomalous diffusion exponent, with sub-diffusive motions corresponding to $0 < \gamma < 1$ and super-diffusive motions corresponding to $1 < \gamma < 2$.

The MSD is simply the second moment of the underlying probability distribution of displacements. Various anomalous diffusion processes yield fractional ($\gamma \neq 1$) dynamics [35, 36]. The simplest generalization to the Gaussian probability distribution function of Brownian motion is given by the models of fractional Brownian motion as well as the generalized Langevin equation, which both yield (in 1D)

$$P(x,t) = \frac{1}{\sqrt{4\pi K_\gamma t^\gamma}} \exp\left(\frac{-x^2}{4K_\gamma t^\gamma}\right), \tag{6.4}$$

where $0 < \gamma \leq 2$.

Enhanced diffusion with a 3/2 power law has been related to the random velocity field model, first described by Matheron *et al.* [37] to understand water transport in microscopically heterogeneous rocks. This model describes coupling between diffusion and random, but spatially correlated velocities: a particle diffuses in a stratified fluid where each layer of fluid has a random velocity. Redner [10], Zumofen *et al.* [9], and Bouchaud *et al.* [8] obtained the probability distribution of displacements for diffusion in random velocity fields,

$$P(x,t) = \frac{A}{\sqrt{t^{3/2}}} \exp\left(-\left(\frac{x^2}{4K_\gamma t^{3/2}}\right)^{\delta/2}\right). \tag{6.5}$$

In the above, A is the normalization factor with dimension $[A] = m^{-1}s^{3/4}$, and K_γ

is the generalized diffusion constant. δ is a parameter that is not fully determined within the model, but is expected to be less than 1.7, while the asymptotic behavior considering large displacements suggests $\delta \leq 4/3$ [10].

The deviation of the distribution function from a Gaussian also can be quantified using both the second moment, $\langle x^2 \rangle$, and the fourth moment, $\langle x^4 \rangle$, of the distribution of displacements (in 1D) using the non-Gaussian parameter [38]

$$\alpha_2 = \frac{\langle x^4 \rangle}{3\langle x^2 \rangle^2} - 1. \tag{6.6}$$

The value of α_2 is a sensitive measure for the type of anomalous diffusion. For Gaussian-distributed displacements $\alpha_2 = 0$, while this parameter deviates from zero for non-Gaussian distributions.

In the tracer-particle tracking experiments in this work, we can readily obtain mean-squared displacements as well the fourth moments as a function of time; we can therefore obtain the value of γ as well as α_2. For short times, we can also construct the entire probability distribution of displacements $P(x,t)$ with reasonable precision, but out-of-plane escape of particles at long times limits doing so for all times.

6.5 Results and discussion

6.5.1 Non-Gaussian distributions

The probability distribution of particle displacements in the x and y directions, as a function of t, is calculated based on the trajectories by averaging over all start times t_0 and particles. An example of $P(x,t)$ is shown in FIG. 6.3 for $E = 3.5$ V/μm, at $h_p = 10$ μm, for 0.5, 1, 2, and 6 Hz and for different times. $P(x,t)$ only obtained for short times, as the statistics gets progressively poorer for longer times. The distribution at

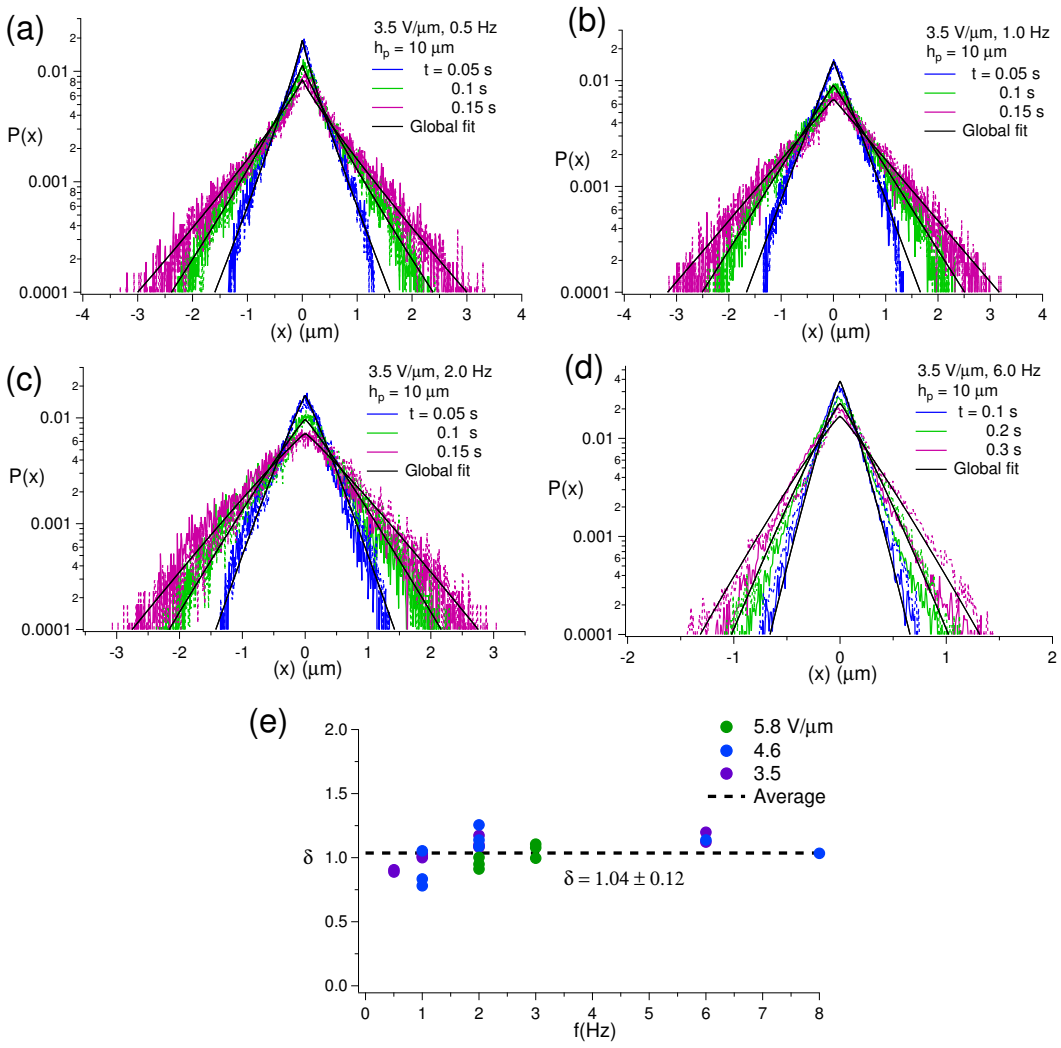

Figure 6.3: Normalized histogram: (a)-(d): show four examples of the normalized distribution histograms along x and y in three successive times and at four different frequencies, 0.5, 1, 2, and 6 Hz, respectively. $E = 3.5$ V/μm, perpendicular to the page and $h_p = 10$ μm. (e): Variation of δ versus f gives rise to mean value of 1.04 ± 0.12.

short times is distinctly non-Gaussian. Equation (6.5) is used to fit the probability distributions. For the short times examined, there is good agreement. Decreasing the field amplitude corresponds to lowering the driving, and so does increasing field frequency, because it takes us from the strong to the weak hydrodynamic regime (as described in earlier work [25, 30]. With increasing frequency, we find that the fits are

not as good at large displacements. In a few datasets, the $P(x,t)$ are asymmetric: these data were not fit. These asymmetries likely arise from drop size non-uniformities, which result in local drifts inside the cell.

From the above fits, one can get the unknown parameter δ, shown in FIG. 6.3(e). The value $\delta = 1.04 \pm 0.12$ is experimentally consistent with $\delta = 1$, which is a simple exponential dependence on the absolute value of the displacement. We note, first, that these distributions have been obtained only for short times, which correspond to small overall displacements, and the behavior at long times could be very different. While $\gamma = 3/2$ and $\delta \simeq 1$ is consistent with the prediction of $\gamma = 3/2$ and $\delta \leq 1.7$ in the random velocity field model, we emphasize that the flows here are different. In the random velocity field model, a tracer particle samples random velocities in different strata by diffusing between strata, while in the current system, all the unsteady motions are driven motions. As shown in Supplemental material, Section 6.8.2.2, Movie 6.2, the velocities in the plane are isotropic and spatially varying because they enter into the plane and emanate outward from each of the trapped drops (see FIG. 6.2), and exit out of the plane in between the drops.

6.5.2 Dynamics: Anomalous super-diffusive transport

Next, we examine the dynamics of particles, as a function of frequency, field amplitude and height, *via* the mean-squared displacement (MSD) of tracer-particles centroids. Since the motions are isotropic in the plane (*i.e.*, $\langle x^2 \rangle = \langle y^2 \rangle$), the 2D mean-squared displacement, $MSD = \langle x^2 \rangle + \langle y^2 \rangle$ is plotted instead. FIG. 6.4(a), shows an example of $\log(MSD)$ versus $\log(t)$ for $E = 3.5\ V/\mu$m for different frequencies and three heights of interest over a 10 s time interval. A longer time analysis roughly about 40 s, equivalent to a stack of 400 frame recorded at 10 fps, is also carried out. Two examples, presented in FIG. 6.7 in the Supplemental material, Section 6.8.1, show no

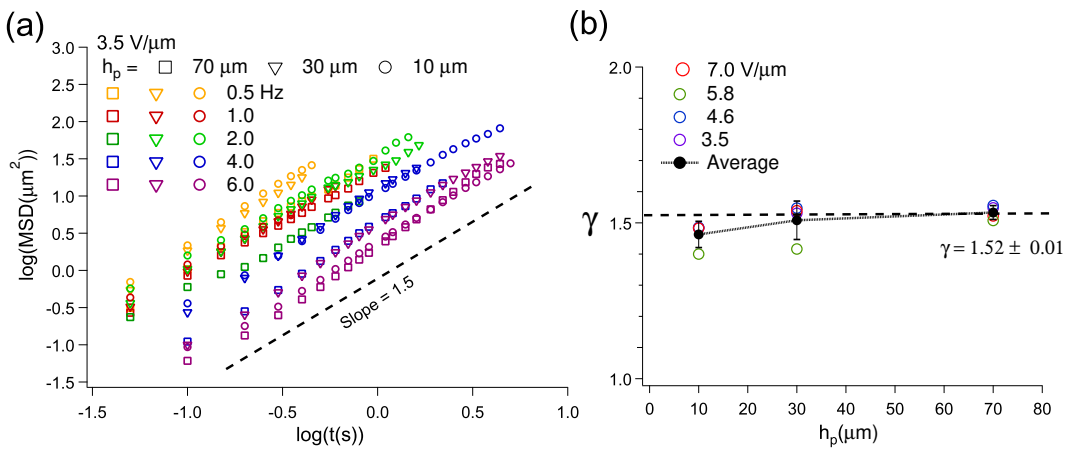

Figure 6.4: (a): $\log(MSD)$ versus $\log(t)$ shows a linear dependency with the slope of $\gamma \simeq 1.5$ consistent with enhanced super-diffusive dynamics in the outer fluid. $\gamma \simeq 1.5$ is independent of frequency, field amplitude, and the height above the bottom electrode (*i.e.*, the $x-y$ plane) at which the experiment is carried out. (b): γ versus h_p, which is averaged over frequency and amplitude, respectively, shows a mean value of $\gamma = 1.52 \pm 0.01$.

differences between the short and long time analysis, likely because the limiting time is not the duration of observation but the time the particles remain in the plane. For all fields, heights and frequencies, the dependence, viewed on a log-log scale, is linear and the slope is close to 3/2. The value of γ for each field amplitude as a function of height is reported in FIG. 6.4(b) while the average value of $\gamma = 1.52 \pm 0.01$.

There could be multiple origins for the 3/2 power law. Fractional tracer dynamics with a power law exponent $\gamma \approx 3/2$ has been reported theoretically and experimentally. A numerical study of Lévy random walks [11] finds superdiffusive transport with $\gamma \simeq 1.47$; the probability distribution function is a modified Gaussian for short displacements but a power law for large displacements. In experiments, Caspi *et al.* [12, 13] reported super-diffusive motions with a $t^{3/2}$ scaling at short times for the MSD of a microsphere inside a living cell. They argued that a time-dependent friction imposed by the non-Newtonian medium of the living cell is responsible for the power

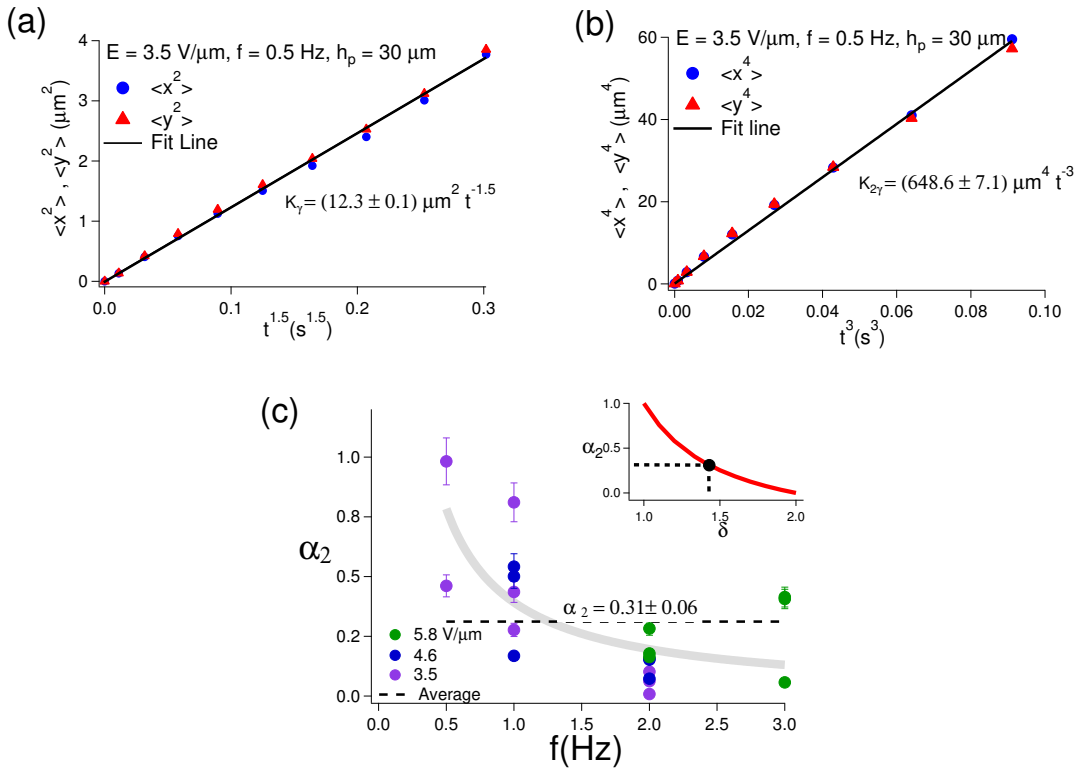

Figure 6.5: (a): The second moment of the distribution of displacements along x and y depends linearly on $t^{1.5}$: the slope $K_\gamma = 12.3 \pm 0.1 \mu\text{m}^2/\text{s}^{1.5}$ (b): The fourth moment of x and y distribution of displacements depends linearly on t^3: the slope $K_{2\gamma} = 648.6 \pm 7.1$. (c): The non-Gaussian parameter has an approximate inverse frequency dependence (shown by the light grey line), with an average value $\alpha_2 = 0.31 \pm 0.06$. The inset shows α_2 calculated from Equation (6.5) for different values of the, in principle, unknown, δ parameter. A value $\alpha_2 = 0.31 \pm 0.06$ corresponds to $\delta = 1.43 \pm 0.06$.

law scaling behavior. Regner *et al.* [39] showed theoretically and experimentally that interacellular transport, cytoskeletal transport along microtubules, follows fractional Brownian motion with power law scaling of 3/2 for short and long lag times.

One also can measure the non-Gaussian parameter, α_2, from the second and the fourth moment of the probability distribution of displacements. As a practical matter, the second and fourth moments probe large displacements more efficiently, and so this can be compared with the probability distributions obtained at short

times, and hence, small displacements. Plotted in FIG. 6.5 (a) and (b) for one field amplitude, $E = 3.5\ V/\mu$m and frequency $f = 0.5$ Hz, one sees that $\langle x^2 \rangle$ and $\langle y^2 \rangle$ have a linear relationship to $t^{1.5}$, FIG. 6.5 (a), while $\langle x^4 \rangle$ and $\langle y^4 \rangle$ have a linear relation to t^3, FIG. 6.5 (b). Fitting to the linear forms, $\langle x^2 \rangle = K_\gamma t^{1.5}$, $\langle y^2 \rangle = K_\gamma t^{1.5}$ and $\langle x^4 \rangle = K_{2\gamma} t^3$ and $\langle y^4 \rangle = K_{2\gamma} t^3$, one can explicitly obtain, for the probability distribution in Equation (6.5),

$$\alpha_2 = \frac{K_{2\gamma}}{3K_\gamma^2} - 1. \tag{6.7}$$

For all field amplitudes, α_2 is plotted in FIG. 6.5(c) as a function of the field frequency. While the results show more dispersion than those for γ, averaging over *all* datasets yields a value of $\alpha_2 = 0.31 \pm 0.06$. Within errors there is possibly an inverse relationship of α_2 with frequency. For the probability distribution in Equation (6.5), α_2 can be calculated given a value of δ: $\alpha_2 = 0.31 \pm 0.06$ corresponds to $\delta = 1.43 \pm 0.06$. This is larger than $\delta = 1$, obtained for short times, and interestingly, close to the asymptotic value $\delta \simeq 4/3$ for large displacements in the random-velocity-field model [10].

6.5.3 Hydrodynamic length scales

Next, the generalized diffusion constant, K_γ, is shown in FIG. 6.6(a). This was obtained directly from the MSD–time plot in FIG. 6.4(a). By rewriting Eq. 6.3 as $\log(MSD) = \log(4K_\gamma) + \gamma \log(t)$, K_γ was simply obtained from the y-intercept of a linear fit to each dataset in FIG. 6.4(a). K_γ decreases with increasing frequency. This is consistent with decreasing particle diffusivity in the outer fluid. From K_γ, we can construct a lengthscale $\lambda_h = \sqrt{K_{1.5}/f^{1.5}}$. λ_h is an average length one particle moves in one period of the ac oscillation, *i.e.*, f^{-1} s. λ_h versus frequency is plotted in FIG. 6.6(b) and shows a decreasing trend by increasing frequency.

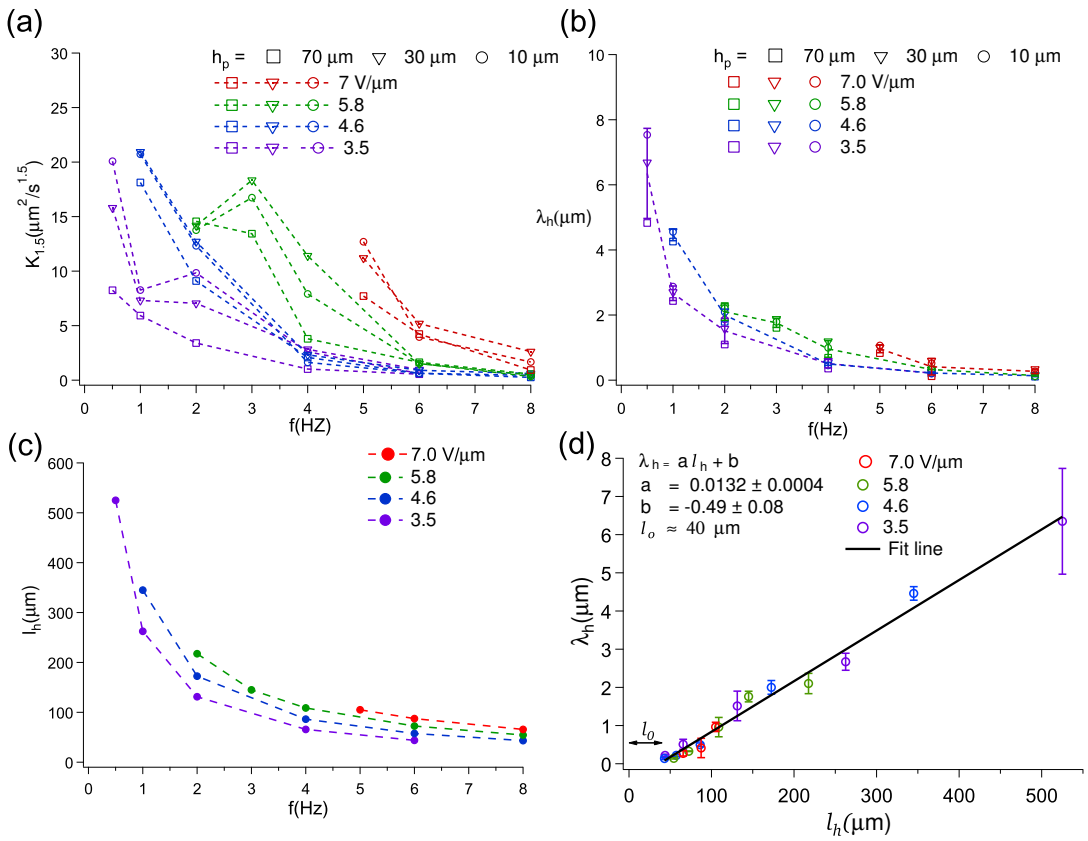

Figure 6.6: (a): Effective diffusion coefficient, K_γ, versus f. (b): An experimental length scale, $\lambda_h = \sqrt{K_{1.5}/f^{1.5}}$, versus frequency, f, for different field amplitudes, frequencies, and heights, shows a monotonic decrease with increasing f. (c): An expected ionic hydrodynamic length, $l_h = \mu_E E/f$, plotted for all field amplitudes for comparison with λ_h. (d): Experimental lengthscale, λ_h, versus ionic hydrodynamic lengthscale, $\l_h$, shows a linear dependency with an x intercept of $l_0 \approx 40$ μm.

The ion mobility length, l_h, is a characteristic length representing the range of the electrohydrodynamic interactions. l_h can be increased by decreasing the frequency, f, because $l_h = v_d/f$, where $v_d = \mu_E E$ is the ionic drift velocity. v_d, in turn, is defined by electric mobility, μ_E, and the electric field amplitude, E. The electric mobility is described by $\mu_E = z_i e_0/6\pi r \mu_{ex}$ where $z_i e_0$ is the ions' charge, and r is the radius of the ions [40]. As a results, l_h is a quantity set by $l_h \propto E/f$. For castor oil, as the carrier fluid, with $\mu_{ex} = 0.819$ Pa.s, $z_i e_0 = 1.6 \times 10^{-19}$ C, and $r \simeq 140 \times 10^{-12}$ m,

the electric mobility is $\mu_E \simeq 75\ \mu\mathrm{m}^2\mathrm{V}^{-1}\mathrm{s}^{-1}$. FIG. 6.6(c) shows l_h versus frequency for all field amplitudes and frequencies used in this work. l_h at low frequencies is about 1 order of magnitude larger than λ_h; however, they show a remarkably similar frequency dependence.

In FIG. 6.6(d), we plot λ_h versus l_h for all field amplitudes and frequencies. λ_h versus l_h shows a remarkably linear dependence, but with an x-intercept of roughly $l_0 \simeq 40\ \mu$m. This indicates that λ_h can be considered to be a kind of *lateral* hydrodynamic length. In contrast to l_h, it is determined experimentally. λ_h is only non-zero above a combination of field and frequency set by $l_h \propto E/f$. The x-intercept, l_0, is an interesting quantity that possibly indicates that there is a minimum threshold of (solvent) ionic displacement required in order to initiate fluid flow. At zero field, the system is heavily overdamped, and there are no observable motions at all. There is a minimum threshold of displacement of ions in the castor oil, l_0, that is required in order to initiate flows, which then can mimic Brownian or superdiffusive motions.

6.6 Conclusion

We have carefully characterized tracer motions, *via* particle-tracking, in an electrohydrodynamically driven system where a spatially varying and time-dependent driving can be realized. Experiments have been carried out as a function of the amplitude and frequency of the external electric field.

We find a robust $t^{3/2}$ power-law for superdiffusive motions in this system, and are able to extract the mathematical form of the underlying probability distribution of displacements, at least for short times. In particular, the parameter δ can be obtained both for short times, and small displacements, and for long times, and larger displacements. Its value is consistent with $\delta \simeq 1$ at short times, which corresponds to a prob-

ability distribution function with a simple exponential dependence on displacement. For longer times, we find $\delta \simeq 1.4$, close to the asymptotic value $\delta \leq 4/3$ obtained for large displacements in the random-velocity-field model [10]. In this model, random velocities in different strata are coupled in by particle diffusion between strata, while in the current system, all the unsteady motions are driven motions. It is interesting that a variety of experimental systems, with different underlying driving forces, display the 3/2-power superdiffusive behavior. This suggests a generic origin that is insensitive to the model details.

Finally, from the tracer motions, we find that we can extract a (frequency- and amplitude-dependent) hydrodynamic lengthscale. This lengthscale reports on the length over which tracer-particle motions are correlated, and in that sense is like the lateral (in-plane) range of hydrodynamic interactions in the system. We also measured the minimum ion mobility length, l_0, required to initiate persistent flows.

6.7 Acknowledgments

This research was supported by the National Science and Engineering Research Council of Canada (NSERC).

Bibliography

[1] R. Metzler. Gaussianity fair: The riddle of anomalous yet non-Gaussian diffusion. *Biophys Journal*, 112:413, 2017.

[2] P. Pöschke, I. M. Sokolov, A. A. Nepomnyashchy, and M. A. Zaks. Anomalous transport in cellular flows: The role of initial conditions and aging. *Physical Review E*, 94(3):032128, 2016.

[3] F. Höfling and T. Franosch. Anomalous transport in the crowded world of biological cells. *Reports on Progress in Physics*, 76(4):046602, 2013.

[4] I. M. Tolić-Nørrelykke, E. L. Munteanu, G. Thon, L. Oddershede, and K. Berg-Sørensen. Anomalous diffusion in living yeast cells. *Physical Review Letters*, 93(7):078102, 2004.

[5] D. S. Banks and C. Fradin. Anomalous diffusion of proteins due to molecular crowding. *Biophysical Journal*, 89(5):2960–2971, 2005.

[6] J. H. Jeon, M. Javanainen, H. Martinez-Seara, R. Metzler, and I. Vattulainen. Protein crowding in lipid bilayers gives rise to non-Gaussian anomalous lateral diffusion of phospholipids and proteins. *Physical Review X*, 6(2):021006, 2016.

[7] A. Ajdari. Transport by active filaments. *Europhysics Letters*, 31(2):69, 1995.

[8] J. P. Bouchaud, A. Georges, J. Koplik, A. Provata, and S. Redner. Superdiffusion in random velocity fields. *Physical Review Letters*, 64(21):2503–2506, 1990.

[9] G. Zumofen, J. Klafter, and A. Blumen. Enhanced diffusion in random velocity fields. *Physical Review A*, 42(8):4601–4608, 1990.

[10] S. Redner. Superdiffusion in random velocity fields. *Physica A: Statistical Mechanics and its Applications*, 168(1):551–560, 1990.

[11] E. M. Trotta and G. Zimbardo. A numerical study of Lévy random walks: Mean square displacement and power-law propagators. *Journal of Plasma Physics*, 81(1), 2015.

[12] A. Caspi, R. Granek, and M. Elbaum. Enhanced diffusion in active intracellular transport. *Physical Review Letters*, 85(26):5655–5658, 2000.

[13] A. Caspi, R. Granek, and M. Elbaum. Diffusion and directed motion in cellular transport. *Physical Review E*, 66(1):011916, 2002.

[14] A. Ott and L. Urbach. Anomalous diffusion in "living polymers": A genuine Lévy flight. *Physical Review Letters*, 65(17):2201, 1990.

[15] N. Gal and D. Weihs. Experimental evidence of strong anomalous diffusion in living cells. *Physical Review E*, 81(2):020903, 2010.

[16] J. F. Reverey, J. H. Jeon, H. Bao, M. Leippe, R. Metzler, and C. Selhuber-Unkel. Superdiffusion dominates intracellular particle motion in the supercrowded cytoplasm of pathogenic Acanthamoeba castellanii. *Scientific Reports*, 5:11690, 2015.

[17] M. Khoury, A. M. Lacasta, J. M. Sancho, and K. Lindenberg. Weak disorder: anomalous transport and diffusion are normal yet again. *Physical Review Letters*, 106(9):090602, 2011.

[18] A. V. Chechkin, F. Seno, R. Metzler, and I. M. Sokolov. Brownian yet non-Gaussian diffusion: from superstatistics to subordination of diffusing diffusivities. *Physical Review X*, 7(2):021002, 2017.

[19] M. V. Chubynsky and G. W. Slater. Diffusing diffusivity: a model for anomalous, yet Brownian, diffusion. *Physical Review Letters*, 113(9):098302, 2014.

[20] J. Guan, B. Wang, and S. Granick. Even hard-sphere colloidal suspensions display Fickian yet non-Gaussian diffusion. *American Physical Society Nano*, 8(4):3331–3336, 2014.

[21] G. Kwon, B. J. Sung, and A. Yethiraj. Dynamics in crowded environments: is non-Gaussian Brownian diffusion normal. *The Journal of Physical Chemistry B*, 118(28):8128–8134, 2014.

[22] B. Wang, S. M. Anthony, S. C. Bae, and S. Granick. Anomalous yet brownian. *Proceedings of the National Academy of Sciences*, 106(36):15160–15164, 2009.

[23] B. Wang, J. Kuo, S. C. Bae, and S. Granick. When Brownian diffusion is not Gaussian. *Nature Materials*, 11(6):481, 2012.

[24] A. Varshney, S. Gohil, M. Sathe, S. Rao RV, J. B. Joshi, S Bhattacharya, A. Yethiraj, and S. Ghosh. Multiscale flow in an electro-hydrodynamically driven oil-in-oil emulsion. *Soft Matter*, 12(6):1759–1764, 2016.

[25] S. Khajehpour Tadavani and A. Yethiraj. Tunable hydrodynamics: a field-frequency phase diagram of a non-equilibrium order-to-disorder transition. *Soft matter*, 13(40):7412–7424, 2017.

[26] J. C. Crocker and D. G. Grier. Methods of digital video microscopy for colloidal studies. *Journal of Colloid and Interface Science*, 179(1):298–310, 1996.

[27] J. C. Crocker and E. R. Weeks. *Particle tracking using IDL, http://www.physics.emory.edu/faculty/weeks//idl/.*

[28] G. I. Taylor. Disintegration of water drops in an electric field. *Proceedings of the Royal Society of London. Series A, Mathematical and Physical Sciences (1934-1990)*, 280(1382):383–397, 1964.

[29] S. Khajehpour Tadavani, J. R. Munroe, and A. Yethiraj. The effect of confinement on the electrohydrodynamic behavior of droplets in a microfluidic oil-in-oil emulsion. *Soft Matter*, 12(45):9246–9255, 2016.

[30] A. Varshney, S. Ghosh, S. Bhattacharya, and A. Yethiraj. Self organization of exotic oil-in-oil phases driven by tunable electrohydrodynamics. *Scientific Reports*, 2:738, 2012.

[31] A. Varshney, S. Gohil, S. Khajehpour Tadavani, A. Yethiraj, S. Bhattacharya, and S. Ghosh. Large scale arrays of tunable microlenses. *Lab on a Chip*, 14(7):1330–1335, 2014.

[32] G. I. Taylor. Studies in electrohydrodynamics. I. The circulation produced in a drop by electrical field. *Proceedings of the Royal Society of London. Series A, Mathematical and Physical Sciences (1934-1990)*, 291(1425):159–166, 1966.

[33] J. R. Melcher and G. I. Taylor. Electrohydrodynamics: A review of the role of interfacial shear stresses. *Annual Review of Fluid Mechanics*, 1(1):111–146, 1969.

[34] J. Klafter, M. F. Shlesinger, and G. Zumofen. Beyond Brownian motion. *Physics Today*, 49(2):33, 2008.

[35] R. Metzler and J. Klafter. The random walk's guide to anomalous diffusion: a fractional dynamics approach. *Physics Reports*, 339(1):1–77, 2000.

[36] R. Metzler and J. Klafter. The restaurant at the end of the random walk: recent developments in the description of anomalous transport by fractional dynamics. *Journal of Physics A: Mathematical and General*, 37(31):R161–R208, 2004.

[37] G. Matheron and G. De Marsily. Is transport in porous media always diffusive? A counterexample. *Water Resources Research*, 16(5):901–917, 1980.

[38] A. Rahman. Correlations in the Motion of Atoms in Liquid Argon. *Physical Review*, 136(2A):A405–A411, 1964.

[39] B. M. Regner, D. Vučinić, C. Domnisoru, T. M. Bartol, M. W. Hetzer, D. M. Tartakovsky, and T. J. Sejnowski. Anomalous diffusion of single particles in cytoplasm. *Biophysical Journal*, 104(8):1652–1660, 2013.

[40] J. Bockris. *Modern electrochemistry*. Plenum Press, New York, 2nd edition, 1998.

6.8 Supplementary material

Movies 6.1 and 6.2 can be found in a CD attached to this thesis.

6.8.1 Mean-squared displacements over shorter and longer times

FIG. 6.7 shows the mean-squared displacement, MSD, of PMMA particles over a 100-frame and a 400-frame image stack. Increasing the number of frames, consequently the time of analysis, does not change the slope of the MSD-time plot. It also does not affect the limiting maximum time at which the MSD sharply decreases.

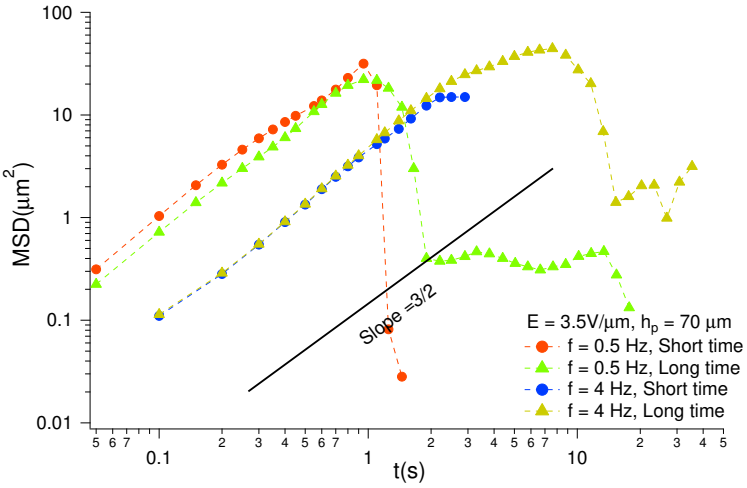

Figure 6.7: MSD versus time for short time, 100 frames recorded at 20 fps for 0.5 Hz and 10 fps for 4 Hz equivalent to 5 and 10 s, respectively. MSD versus time for long time, 400 frames recorded at 20 fps for 0.5 Hz and 10 fps for 4 Hz equivalent to 20 and 40 s, respectively.

6.8.2 Movies

Two image time series show tracer-particle motions around a single silicone oil drop immersed in the leaky-dielectric castor oil medium (Supplemental Movie 1) and over

a larger area containing an array of drops.

6.8.2.1 Supplemental movie 6.1

This image time series shows fluid flow that is tracked by fluorescent PMMA particles around a single silicone oil drop in a leaky-dielectric castor oil medium. Measurements were made in three planes (*i.e.*, heights h_p) and the time series for these three planes were merged into one RGB movie. Red, green, and blue particles represent flows at 70, 30 and 10 μm above the patterned electrode, respectively. $E = 3.5$ V/μm and it is perpendicular to the page, $f = 0.5$ Hz. The movie is a recorded at 20 fps and displayed at 5 fps. Scalebar is 50 μm.

6.8.2.2 Supplemental movie 6.2

This image time series shows motions of fluorescent PMMA particles that are used to get information of the large-scale flows between silicone oil drops in a leaky-dielectric castor oil medium. $E = 5.8$ V/μm and it is perpendicular to the page, $f = 2$ Hz, and $h_p = 10$ μm above the patterned electrode. The movie is a recorded at 20 fps and displayed at 5 fps. Scalebar is 50 μm.

Chapter 7

Summary and future work

7.1 Summary

In this thesis, I employed long-range tunable hydrodynamic interactions to study collective behavior and self-organization in a microfluidic oil-in-oil emulsion, when the outer liquid is "leaky" dielectric. The sample cell is a small capacitor made of two transparent ITO slides, while the distance between electrodes can be varied using different plastic or glass spacers with defined thicknesses. One of the electrodes is selectively etched out, for experiments done in chapters 5 and 6, in order to dielectrophoretically constrain drop motion in 2D.

In chapter 4, I first studied the role of substrate interactions on the size distribution, the mean square displacement, MSD, and velocity of drops in the presence an external DC electric field, using bright field microscopy. With an increase in the amplitude of electric field drops started to break up above a threshold value. This threshold value decreases with increasing the thickness of the cell. The electric capillary number, Ca_E, was used to distinguish quasi-2D and 3D systems at the threshold of drop breakup: for 3D systems Ca_E was close to unity while it was an order of mag-

nitude larger for quasi- 2D systems, indicating the effect of the substrate on stabilizing larger drops. In the thinnest cell, the mean radius, $\overline{R}$, was always comparable to the cell thickness, d, so the substrate was always important. Study of the MSD of silicone oil drops revealed either subdiffusive or normal diffusive behavior at short times. At longer times, the dynamics was superdiffusive. While 2D tracking of drops was inaccessible for 3D systems, we measured the V_{rms} of fluid parcels, using particle image velocimetry, and noticed that by increasing the magnitude of electric field the V_{rms} increased from roughly 10 to 1000 μm/s. Subdiffusive behavior arises from substrate pinning, only seen in thinner samples, while superdiffusive behavior was observed for all sample thicknesses.

Increasing field amplitudes further, prior to chaotic breakup and multiscale flows, led to vertical overturning of drops, resembling of the classic Rayleigh–Bénard convection. To understand the origin of these flows we conducted couple of experiments on castor oil and PMMA tracer particles, using fluorescent microscopy, and for various cell thicknesses. The vertical overturning of fluid was also observed in just pure castor oil system, *i.e.* in the absence of liquid-liquid interfaces. The lateral length scale of observed roll structures was half of the size of those observed for classic Rayleigh–Bénard convection. Another experiment, showing mixing of dyed and non-dyed castor oil in the presence of a DC electric field, recorded by white light illumination and time-lapse macro-scale photography, exhibits enhanced dynamics even in the absence of tracer particles, *i.e.* in the absence of liquid-solid interfaces. The origin of the convective flow thus likely arises from bulk properties, such as the gradient of conductivity near the confining electrodes.

In chapter 5, I studied an order to disorder phase transition, using an external AC electric field, in a silicone oil and castor oil emulsion while the silicone oil droplets were pinned to selectively etched-out spots on the bottom electrode, employing negative

dielectrophoresis. The experiments were carried out using bright field microscopy and a stroboscopic imaging technique. In this system, a negative dielectrophoretic force acts as a harmonic restoring force, that tends to keep drops in their traps. On the other hand, EHD force acts as an effective diffusive force, that tends to push the drops out of the ITO-free regions. The phase diagram was constructed using shape, structure, and dynamics studies. The phase diagram, in amplitude-frequency space, was made of four separate regions. The first region was the ordered region where all droplets were pinned into ITO-free regions and the hydrodynamic length scale was very short, so neighbor drops were not able to interact with each other, nor to break up. The second region was distinguished by polygonal or orientational shape deformations. In this region the hydrodynamic length scale was large enough so the shape of droplets were affected by the shape of their neighbors. The third region, *i.e.* the disordered region, was characterized by numerous breakup and coalescent events while strong hydrodynamic flows push the remaining droplets in different directions on their trapped potential. This region was followed by the fourth one, where very strong breakups and the hydrodynamic flows unpinned all drops from their original trapped positions. This was termed the melting region, because dynamics studies revealed that it has an effective Lindemann parameter of $L_{eff} \simeq 0.08$ which is close to onset of melting in classic 2D systems with $L \simeq 0.1$.

Depending on the amplitude of the electric field, Ca_E varied between 0.27, at low field, to 1.5, at high field, while the pure disordered state, a state without any breakup event, was achieved for $Ca_E \simeq 0.5$. A preliminary experiment was also carried out, using fluorescence microscopy, when the outer fluid was seeded with fluorescent PMMA particles. The flows around each drop were tracked and a superdiffusive tracer particle motion with power law scaling of $MSD \propto t^{3/2}$ was observed. These flows, tracked at short time scales, kicked the drops in different directions and caused

effective diffusive motion of droplets at long time scales.

In chapter 6, these tracer particles flows were studied in depth. Fluid flows in the outer fluid were tracked using PMMA particles, and fluorescent microscopy. The experiment was conducted at three heights of interest: two in the plane and one out of the plane of silicone oil drops. All the experiments were carried out in the ordered regime where hydrodynamic flows are not strong enough to break up or deform droplets. Independent of height, frequency, and amplitude of the external AC electric field an anomalous diffusion with $MSD \propto t^{3/2}$ was observed.

The underlying mechanism of the superdiffusion was studied using the probability distribution of displacements at short time scales and this revealed a non-Gaussian, exponential, distribution function. Equilibrium systems exhibit Gaussian distributions. Non-gaussianity is thus a measure of how far from the equilibrium the system is, and the non-Gaussian parameter, α_2, increases with decreasing frequency. A probability distribution function first proposed for the random velocity field model was fit reasonably well to the data. The unknown parameter δ, defined in random velocity field model, was also obtained experimentally with two different methods: in short times, using the probability distribution function, and in long times, using the non-Gaussian parameter. In short times $\delta \simeq 1$ and in long times $\delta \simeq 1.4$, both consistent with values predicted in random velocity field model for short and large displacements, respectively. Moreover, a hydrodynamic length scale, a length over which the fluid flow motion is correlated and persistent, was measured experimentally for all fields and frequencies. The minimum ion mobility length, $l_0 \simeq 40$ μm, was measured above which the hydrodynamic length scale is not zero.

7.2 Future work

The value of this thesis lies in the fact that it offers a framework for quantitative assessment of tunable hydrodynamic interactions in an oil-in-oil emulsion. However, there are still unanswered questions that one needs to answer in order to construct a full picture of collective behavior and self organization in this tunable hydrodynamic system.

Most dynamics studies thus far have been restricted to two dimensions. Three dimensional structure and dynamics can now be obtained using light-speed focusing lenses [1–4]. In particular, drop shape deformation could be obtained in 3D and real time. This will be an exciting area of future study.

The underlying flows that give rise to the $MSD \propto t^{3/2}$ behavior could be modeled. The fit to a particular distribution function, corresponding to the random velocity field model, 6, was not very appropriate because molecular diffusion is important in that model. Our system, however, is overdamped, and molecular diffusion plays no role in the transport. A simple model has seen enhanced effective diffusion in convective flows [5]. An extension of such a model to examine superdiffusive powerlaw flows would be welcome.

Another observation that we made in chapter 4 was that the maximum field applied in these experiments was determined by the threshold for dielectric breakdown. A curious observation in chapter 4 was that one can go to higher applied electric fields in thin samples than the thick ones. The observation of electro-convection implies the existence of conductivity gradient [6]. This in turn implies that the internal electric field is non-uniform along the field direction. This could explain the different breakdown thresholds, but further work is needed to confirm this.

Bibliography

[1] A. Mermillod-Blondin, E. Mcleod, and C. B. Arnold. High-speed varifocal imaging with a tunable acoustic gradient index of refraction lens. *Optics Letters*, 33(18):2146–8, 2008.

[2] M. Duocastella, B. Sun, and C. B. Arnold. Simultaneous imaging of multiple focal planes for three-dimensional microscopy using ultra-high-speed adaptive optics. *Journal of Biomedical Optics*, 17(5):050505, 2012.

[3] M. Duocastella, G. Vicidomini, and A. Diaspro. Simultaneous multiplane confocal microscopy using acoustic tunable lenses. *Optics Express*, 22(16):19293–301, 2014.

[4] S. Piazza, P. Bianchini, C. Sheppard, A. Diaspro, and M. Duocastella. Enhanced volumetric imaging in 2-photon microscopy via acoustic lens beam shaping. *Journal of Biophotonics*, 11(2), 2018.

[5] M. N. Rosenbluth, H. L. Berk, I. Doxas, and W. Horton. Effective diffusion in laminar convective flows. *Physics of Fluids*, 30(9):2636–2647, 1987.

[6] J. C. Baygents and F. Baldessari. Electrohydrodynamic instability in a thin fluid layer with an electrical conductivity gradient. *Physics of Fluids*, 10(1):301–311, 1998.

Appendix A

Electrohydrodynamics

A.1 A quick review of electromagnetism

A.1.1 Polarization

A dielectric material is an electric insulator that can be polarized by an applied electric field. In the presence of an electric field, the electrically charged molecules do not flow through the material, but only shift from the average equilibrium positions slightly. This shift is called dielectric polarization. The electric dipole moment per unit volume is called electric polarization or simply the polarization of the medium, $\mathbf{P}$, and it is proportional to the strength of the applied electric field. The electric field in dielectric media is the direct result of the electric displacement vector $\mathbf{D}$, which is the electric field corrected for polarization, $\mathbf{D} = \varepsilon_0\mathbf{E} + \mathbf{P} = \varepsilon\mathbf{E}$, where ε is absolute permittivity, or simply permittivity of the medium.

Inside the dielectric material there could be both bound and isolated charges. As a result, Gauss's law may be written as Poisson equation:

$$\nabla \cdot \varepsilon_0\mathbf{E} = \rho_P + \rho_f \quad \rightarrow \quad \nabla \cdot \mathbf{D} = \rho_f \tag{A.1}$$

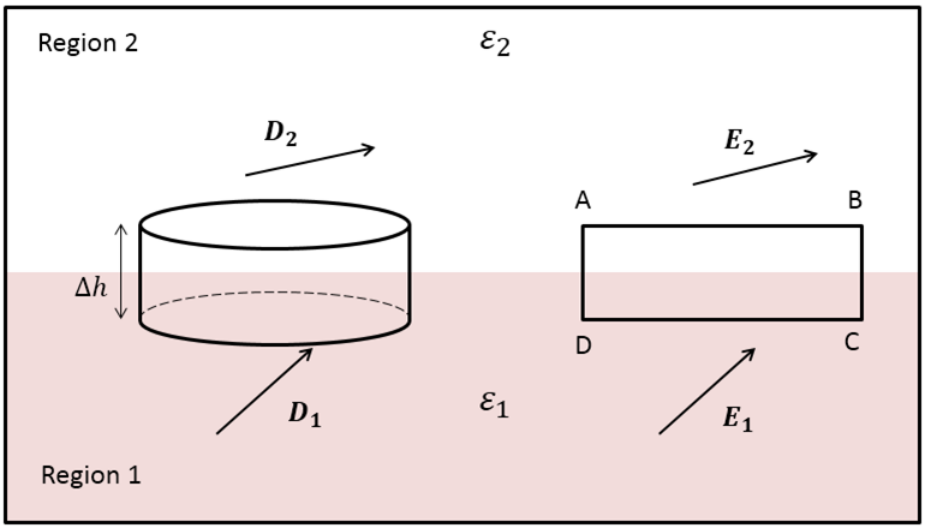

Figure A.1: Geometry for determining boundary conditions in dielectric-dielectric interface (adapted from [1]).

where ρ_f is the isolated, or free charge density in the volume. In dielectric materials, the bulk and surface polarization charge densities are defined as $\rho_P \equiv -\nabla \cdot \mathbf{P}$ and $\sigma_P \equiv \mathbf{P} \cdot \mathbf{n}$, respectively. For $\rho_f = 0$ the Poisson equation converts to Laplace equation as

$$\nabla \cdot \mathbf{D} = 0. \tag{A.2}$$

A.1.2 Boundary conditions

Consider Fig. A.1 where region (1) of permittivity ε_1 and region (2) of permittivity ε_2 are separated by an interface. The electric field, $\mathbf{E}$, is conservative and hence derivable from a scalar potential. Thus in the path ABCD shown in Fig. A.1 right, where AD and BC are arbitrarily small, the line integral reduces to

$$\oint \mathbf{E} \cdot d\mathbf{l} = 0 \Longrightarrow \mathbf{E_{1t}} = \mathbf{E_{2t}} \quad or \quad \hat{\mathbf{n}} \times (\mathbf{E_1} - \mathbf{E_2}) = 0, \tag{A.3}$$

where $\hat{\mathbf{n}}$ is the unit normal vector and $\mathbf{t}$ represents the tangential component. Based on this equation the tangential components of the electric field are continuous across the interface.

On the other hand, the contributions to the flux out, $\mathbf{D} \cdot \hat{\mathbf{n}} da$, where da is a differential area of the side of the "pill box" in Fig. A.1, is neglected when $\triangle h \to 0$, then Gauss's law gives $(D_{1n} - D_{2n}) \triangle a = \sigma_f \triangle a$ or more concisely

$$\hat{\mathbf{n}} \cdot (\mathbf{D_1} - \mathbf{D_2}) = \sigma_f. \tag{A.4}$$

Here σ_f is the total free surface charge density. From this equation one can realize that the normal component of the electric flux density is not continuous at the interface. These two sections have been adapted from chapters 4, 1 and 1 of Ref. [1–3]

A.1.3 Maxwell stress tensor

The total electromagnetic force exerted on a moving charge in an electromagnetic field is $\mathbf{F} = \int_v (\rho\mathbf{E} + \mathbf{J} \times \mathbf{B})\, dv$, hence the force per unit volume is evaluated by $\mathbf{f} = \rho\mathbf{E} + \mathbf{J} \times \mathbf{B}$, where ρ, $\mathbf{E}$, $\mathbf{J}$, and $\mathbf{B}$ are the total charge density, electric field, the current density, and the magnetic field, respectively. Using Maxwell's equations and vector field theory the force per unit volume can be written in the form

$$\mathbf{f} = \nabla . \overleftrightarrow{\mathbf{T}} - \varepsilon_0 \mu_0 \frac{\partial \mathbf{S}}{\partial t}, \tag{A.5}$$

where $\overleftrightarrow{\mathbf{T}}$, and $\mathbf{S}$ are the Maxwell stress tensor, and Poynting vector. Maxwell stress tensor represents the interaction between electric and magnetic forces and mechanical momentum. It is the stress tensor of an electromagnetic field. More specially, T_{ij} is the force (per unit area) in the ith direction acting on an element of surface oriented

in jth direction and it is shown by

$$T_{ij} \equiv \varepsilon_0 \left(E_i E_j - \frac{1}{2}\delta_{ij} E^2 \right) + \frac{1}{\mu_0} \left(B_i B_j - \frac{1}{2}\delta_{ij} B^2 \right). \tag{A.6}$$

where δ_{ij} is the Kronecker delta. The Poynting vector, $\mathbf{S}$, is the energy per unit time, per unit area, transported by the fields. In the static case, $\mathbf{S}$ is independent of time, and the second term in Equation (A.5) drops out and the electromagnetic force on the charge configuration can be expressed entirely in terms of the stress tensor. The diagonal elements of the stress tensor (T_{xx}, T_{yy}, T_{zz}) represent pressure and the off-diagonal elements (T_{xy}, T_{xz}, etc.) are shear stresses [4]. In the absence of any magnetic field, the stress tensor is in the form

$$T_{ij} \equiv \varepsilon_0 \left(E_i E_j - \frac{1}{2}\delta_{ij} E^2 \right). \tag{A.7}$$

In a dielectric material, the Maxwell stress tensor is written as

$$T_{ij} \equiv \varepsilon_0 k \left(E_i E_j - \frac{1}{2}\delta_{ij} E^2 \right), \tag{A.8}$$

where k is the dielectric constant of the material. The stress tensor in spherical coordinates can be written in the form

$$\overleftrightarrow{T} = \begin{bmatrix} T_{rr} & T_{r\theta} & T_{r\phi} \\ T_{\theta r} & T_{\theta\theta} & T_{\theta\phi} \\ T_{\phi r} & T_{\phi\theta} & T_{\phi\phi} \end{bmatrix} = \varepsilon \begin{bmatrix} E_r^2 - \frac{1}{2}E^2 & E_r E_\theta & E_r E_\phi \\ E_\theta E_r & E_\theta^2 - \frac{1}{2}E^2 & E_\theta E_\phi \\ E_\phi E_r & E_\phi E_\theta & E_\phi - \frac{1}{2}E^2 \end{bmatrix},$$

where $\varepsilon = \varepsilon_0 k$, and $E^2 = E_r^2 + E_\theta^2 + E_\phi^2$. At the interface of two dielectric media the Maxwell stress tensor is $\overleftrightarrow{T} = \overleftrightarrow{T_2} - \overleftrightarrow{T_1}$. The radial component is

$$T_{rr} = \frac{1}{2}(\varepsilon_2(E_{2r}^2 - E_{2\theta}^2) - \varepsilon_1(E_{1r} - E_{1\theta}^2)), \tag{A.9}$$

resembles a radial sheer, $T_{rr} > 0$, or pressure, $T_{rr} < 0$, except that it has a and θ dependence. The tangential component

$$T_{\theta r} = \varepsilon_2 E_{2\theta} E_{2r} - \varepsilon_1 E_{1\theta} E_{1r}, \tag{A.10}$$

is a shear stress [5].

A.2 A quick review of fluid mechanics

A.2.1 Introduction

Some of the macroscopic properties of a fluid affect how the fluid reacts to applied forces. Those properties that are most closely coupled to motion of the fluid are viscosity, μ (the shear stress required to achieve unit rate of strain), surface tension, γ (the energy required to increase the surface area of a liquid by a unit of area), and density, ρ (the ratio of the mass of a fluid to its volume). In a compressible fluid the density of the fluid varies significantly with change of pressure, while in an incompressible one the density is constant even with varying pressure [6]. All fluids discussed here are assumed to be incompressible.

A.2.2 Governing equations: Continuity and Navier-Stokes equations

A.2.2.1 Conservation of mass: the continuity equation

The conservation of mass in fluid flow comes from the fact that mass can not be created or destroyed within a volume v. As a consequence, the accumulation of mass inside the volume is accounted for by net flow of mass across the surface, S, of that volume. Mathematically

$$d\left(\int_v \rho dv\right) = -\left(\int_S \rho \mathbf{V} \cdot \mathbf{n} dS\right) dt, \tag{A.11}$$

where $\mathbf{V}$ and ρ are the velocity vector and mass density of the fluid, respectively.

The surface integral can be transformed to a volume integral and the new equation is valid for any volume, so the differential form of the continuity equation is shown by

$$\frac{\partial \rho}{\partial t} + \nabla \cdot (\rho \mathbf{V}) = 0. \tag{A.12}$$

The last equation can be written in the form of material derivative, $\frac{D}{Dt} = \frac{\partial}{\partial t} + \nabla \cdot \mathbf{V}$, of the mass density as

$$\frac{D\rho}{Dt} + \rho \nabla \cdot \mathbf{V} = 0. \tag{A.13}$$

For an incompressible fluid, density is constant in time and position, thus the continuity equation is in the form of [6, 7]

$$\nabla \,.\, \mathbf{V} = 0. \tag{A.14}$$

A.2.2.2 Conservation of momentum: Navier-Stokes equation

The momentum equation simply applies Newtonian's second law of motion, which states that the change in the linear momentum is equal to the sum of the forces acting on the mass. Namely

$$\begin{aligned}
&\frac{\partial}{\partial t}\int_{\upsilon}\rho\mathbf{V}d\upsilon && \text{(rate of accumulation of linear momentum in volume } \upsilon\text{)}\\
+&\int_{S}\rho\mathbf{V}\mathbf{V}\cdot\mathbf{n}dS && \text{(flux of linear momentum out through surface } S\text{)}\\
=&\int_{\upsilon}\rho\mathbf{g}d\upsilon && \text{(rate of gain of linear momentum due to body forces)}\\
+&\int_{S}\overleftrightarrow{\Upsilon}\cdot\mathbf{n}dS && \text{(rate of gain of linear momentum due to surface stresses, } \overleftrightarrow{\Upsilon}\text{).}
\end{aligned}$$

Using equation (A.14) and in the presence of the electric body forces the equation of motion or conservation of momentum can be written in the form of

$$\rho\frac{\partial\mathbf{V}}{\partial t}+\rho\mathbf{V}\cdot\nabla\mathbf{V}=\rho\mathbf{g}+\nabla\cdot\overleftrightarrow{\Upsilon} \tag{A.15}$$

where Υ is total stress tensor at interface. In the presence of electric stress $\overleftrightarrow{\Upsilon} = \overleftrightarrow{\tau}+\overleftrightarrow{T}$, where $\overleftrightarrow{\tau}$, $\overleftrightarrow{T}$ are surface stress and Maxwell stress tensors.

A.2.3 Stress tensor

In a fluid at rest, there are only normal components of stress on a surface and the stress tensor is isotropic and may be written in terms of the Kronecker delta, δ_{ij},

$$\tau_{ij}=-p\delta_{ij}, \tag{A.16}$$

where p is thermodynamic pressure. The negative sign is due to the fact that the normal components of τ are regarded as positive if they indicate tension rather than

compression.

A moving fluid develops additional components of stress due to viscosity. So the off-diagonal terms of τ become non-zero, and shear stresses develop. For a moving fluid, when the relaxation time of the molecules is small compared to the time scale of the flow, the stress splits into stress at rest, $-p\delta_{ij}$, and stress due to the fluid motion, σ_{ij}, as

$$\tau_{ij} = -p\delta_{ij} + \sigma_{ij}. \tag{A.17}$$

The anisotropic part, σ_{ij}, is related to the velocity gradients. For incompressible fluids, the stress tensor takes the simple form of

$$\tau_{ij} = -p\delta_{ij} + 2\mu e_{ij}, \tag{A.18}$$

where μ is viscosity of the fluid and $e_{ij} \equiv \frac{1}{2}\left(\frac{\partial V_i}{\partial x_j} + \frac{\partial V_j}{\partial x_i}\right)$. For an incompressible fluid with electric body forces the equation of motion, equation (A.15), reduces to

$$\rho\frac{\partial \mathbf{V}}{\partial t} + \rho\mathbf{V}\cdot\nabla\mathbf{V} = -\nabla p + \rho\mathbf{g} + \mu\nabla^{\mathbf{2}}\mathbf{V} + \nabla\cdot\overleftrightarrow{T}. \tag{A.19}$$

At very low Reynolds number the non-linear term, $\rho\mathbf{V}\cdot\nabla\mathbf{V}$ in equation A.19 vanishes.

A.2.4 Boundary conditions

The differential equations for the conservation laws are subject to boundary conditions in order to properly formulate any problem. Consider a fluid-fluid interface like a liquid drop in the surrounding continuous phase of the second liquid. The unit normal and tangential vectors at the interface are represented by $\hat{\mathbf{n}}$ and $\hat{\mathbf{t}}$, respectively. The continuity of the velocity at interface can be viewed in two parts, one on the continuity

of the tangential component of two velocities, the no-slip boundary condition

$$\mathbf{V_1} \cdot \hat{\mathbf{t}} = \mathbf{V_2} \cdot \hat{\mathbf{t}}, \tag{A.20}$$

and the other one on the continuity of the normal component of two velocities, a kinetic consequence when there is no mass transfer across the interface

$$\mathbf{V_1} \cdot \hat{\mathbf{n}} = \mathbf{V_2} \cdot \hat{\mathbf{n}}. \tag{A.21}$$

We also need a boundary condition connecting the state of total stress, which could be the viscous stress and the electric stress, and other stresses, in each fluid at the interface. This condition shows that the total force on the area element must be zero and it can be written as follows [8]

$$\hat{\mathbf{n}} \cdot \left(\overleftrightarrow{\Upsilon}_{\mathbf{1}} - \overleftrightarrow{\Upsilon}_{\mathbf{2}} \right) = 2C\gamma\hat{\mathbf{n}} - \nabla_{\mathbf{s}}\gamma. \tag{A.22}$$

To summarize, in the stress boundary condition, the symbols Υ_1 and Υ_2 represent the total stress tensor in each fluid, which can be viscous stress, electric stress, or any other stress at interface: in this study $\overleftrightarrow{\Upsilon} = \overleftrightarrow{\tau} + \overleftrightarrow{T}$. C is the mean curvature of the interface at the point where the condition is being applied, γ is the interfacial tension of the fluid-fluid interface, and $\nabla_{\mathbf{S}}$ is the surface gradient operator. The left side in the stress boundary condition is the difference between the stress vectors in fluids 1 and 2 at the interface, or the "jump" in stress. The resulting vector is decomposed into a part that is normal to the interface, namely the first term on the right side, and a part that is tangential to the interface, given in the second term on the right side.

Bibliography

[1] J. R. Reitz, F. J. Milford, and R. W. Christy. *Foundations of electromagnetic theory*. Addison-Wesley, San Francisco, 4th edition, 2008.

[2] J. D. Jackson. *Classical electrodynamics*. Wiley, New York, 3rd edition, 1998.

[3] H. P. Neff. *Introductory electromagnetics*. Wiley, New York, 1st edition, 1991.

[4] D. J. Griffiths. *Introduction to electrodynamics*. Pearson, Boston, 4th edition, 2012.

[5] S. Torza, R. G. Cox, and S. G. Mason. Electrohydrodynamic deformation and burst of liquid drops. *Philosophical Transactions of the Royal Society of London. Series A, Mathematical and Physical Sciences*, 269(1198):295–319, 1971.

[6] J. A. Fay. *Introduction to fluid mechanics*. The MIT Press, Cambridge, Mass., 1994.

[7] L. D. Landau and E. M. Lifshitz. *Fluid mechanics*. Butterworth-Heinemann, Amsterdam, 2nd edition, 1987.

[8] P. K. Kundu and I. M. Cohen. *Fluid mechanics*. Academic Press, Waltham, MA, 5th edition, 2011.

Appendix B

Drop deformation function

B.1 PDM approach

Drop deformation function is defined by $D = \frac{d_{\parallel} - d_{\perp}}{d_{\parallel} + d_{\perp}}$, where $d_{\parallel}$, $d_{\perp}$ are the axes of the ellipsoidal droplet parallel and perpendicular to the direction of the externally applied electric field. One can measure D from the mean curvature of the interface and it is usually calculated by examining small perturbations from the spherical shape using analytical or numerical methods [1, 2]. The mean curvature itself, C, is determined by Navier-Stokes equation for incompressible fluid, equation (A.19), continuity equation and the boundary conditions. One can relate the mean curvature function to the drop shape function, $\Gamma(\theta)$, defined by [3]

$$C = a - \frac{1}{a^2}\Big(\Gamma(\theta) + \frac{1}{2sin(\theta)}\frac{d}{d\theta}(sin(\theta)\frac{d\Gamma(\theta)}{d\theta})\Big), \tag{B.1}$$

where θ is the polar angle with respect to applied field direction. The drop deformation function, D, is related to $\Gamma(\theta)$ by

$$D = \frac{\Gamma(0) - \Gamma(\pi/2)}{2a}. \tag{B.2}$$

If the gravitational influences are neglected in equation (A.19), and there is no bulk free charge in the fluids, then the electric body force term vanishes too, and the hydrodynamic governing equations are summarized as

$$-\nabla p + \mu \nabla^{\mathbf{2}} \mathbf{V} = 0 \quad \text{and} \quad \nabla \cdot \mathbf{V} = 0. \tag{B.3}$$

It is worthwhile to mention that at steady state and for creeping flow, the unsteady and convective accelerations terms on the left hand side of equation (A.19) were dropped. The hydrodynamic boundary conditions are (A.20), (A.21), when the normal component of the velocity is equal to zero in both media, and (A.22). Equation (A.22) splits into normal and tangential components of the total force per unit area acting on the interface as

$$\begin{aligned}(p_{in} - p_{ex}) + (\mu_{ex} \nabla \mathbf{V}_{ex} \cdot \mathbf{n} - \mu_{in} \nabla \mathbf{V}_{in} \cdot \mathbf{n}) \cdot \mathbf{n} + \frac{1}{2} \left(\varepsilon_{in} |\mathbf{E}_{in}|^2 - \varepsilon_{ex} |\mathbf{E}_{ex}|^2 \right) + \\ (\varepsilon_{ex} \mathbf{E}_{ex} \mathbf{E}_{ex} \cdot \mathbf{n} - \varepsilon_{in} \mathbf{E}_{in} \mathbf{E}_{in} \cdot \mathbf{n}) \cdot \mathbf{n} - 2\gamma C = 0,\end{aligned} \tag{B.4}$$

and

$$(\mu_{ex} \nabla \mathbf{V}_{ex} \cdot \mathbf{n} - \mu_{in} \nabla \mathbf{V}_{in} \cdot \mathbf{n}) \cdot \mathbf{t} = 0, \tag{B.5}$$

respectively. Here p, μ, ε, γ are the pressure, viscosity, dielectric permittivity and the interfacial tension of the media, respectively. The subscripts in and ex are used to represent the droplet and the suspending fluid, respectively. The unit outward normal to the drop surface is n, and C is the a non-zero mean curvature of the interface. To make the equation (B.4) clear, lets consider $\mathbf{E} = 0$, the interfacial tension is uniform at the surface of the drop, so the normal component of the equation (A.22) will be the Laplace equation as $p_{in} - p_{ex} = 2\gamma C$. In this case the drop is spherical, $p_{ex} = 0$ and $C = \dfrac{1}{a}$. Next, one can consider the case $\mathbf{E} \neq 0$, so the drop feels the normal component of the viscous and electric stresses, shown by the second, third and fourth

terms in equation (B.4). Also the hydrostatic pressures inside and outside of the drop, the first term in equation (B.4), are affected by the applied electric field so $p_{ex} \neq 0$. The other boundary condition for Navier-Stokes equation is shown by

$$-p_{ex}I + \mu_{ex}\left(\nabla \mathbf{V}\right) = 0 \quad \text{at infinity,} \tag{B.6}$$

where I is the unit tensor. This equation is simply the equation (A.18) [1, 4].

B.2 LDM approach

The hydrodynamic equations for PDM, are also applicable to the LDM [5, 6]. The only difference appears in equation (B.5) due to the additional tangential stress arising from the interfacial charges, so

$$\left(\mu_{ex}\nabla \mathbf{V}_{ex} \cdot \mathbf{n} - \mu_{in}\nabla \mathbf{V}_{in} \cdot \mathbf{n}\right) \cdot \mathbf{t} + \left(\varepsilon_{ex}\mathbf{E}_{ex}\mathbf{E}_{ex} \cdot \mathbf{n} - \varepsilon_{in}\mathbf{E}_{in}\mathbf{E}_{in} \cdot \mathbf{n}\right) \cdot \mathbf{t} = 0. \tag{B.7}$$

.

Bibliography

[1] E. Zholkovskij, J. Masliyah, and J. Czarnecki. An electrokinetic model of drop deformation in an electric field. *Journal of Fluid Mechanics*, 472:1–27, 2002.

[2] M. N. Reddy. *Fundamental studies on the dynamics of drops in electric fields.* Proquest, Umi Dissertation Publishing, 2011.

[3] L. D. Landau and E. M. Lifshitz. *Fluid mechanics*. Butterworth-Heinemann, Amsterdam, 2nd edition, January 1987.

[4] G. Supeene, C. R. Koch, and S. Bhattacharjee. Deformation of a droplet in an electric field: Nonlinear transient response in perfect and leaky dielectric media. *Journal of Colloid And Interface Science*, 318(2):463–476, 2008.

[5] P. Vlahovska, R. Graciá, S. Aranda-Espinoza, and R. Dimova. Electrohydrodynamic model of vesicle deformation in alternating electric fields. *Biophysical Journal*, 96(12):4789–803, 2009.

[6] O. Vizika and D. A. Saville. The electrohydrodynamic deformation of drops suspended in liquids in steady and oscillatory electric fields. *Journal of Fluid Mechanics*, 239(1):1–21, 1992.